Biomaterials Translational

Contents

Quarterly Established in December 2020. Volume 4, Issue 3 September 28, 2023

Editorial

Viewpoint

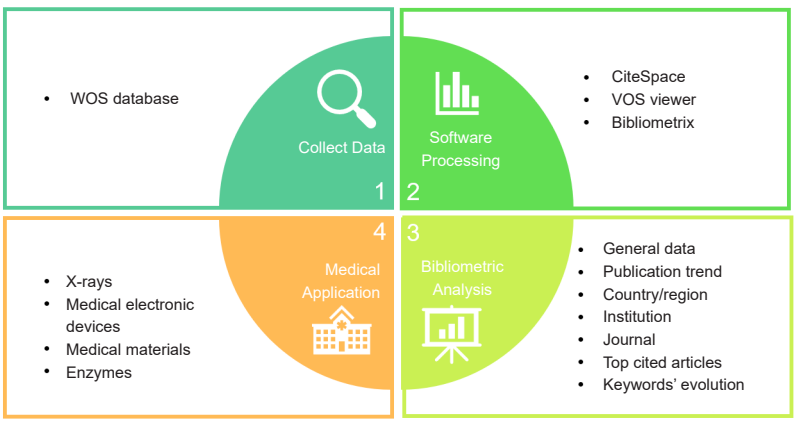

This review examines the application of perovskite in medical materials through bibliometric analysis, obtains the development history of perovskite in time and space, summarises the application of perovskite in the medical field from four aspects and prospects the future development.

Reviews

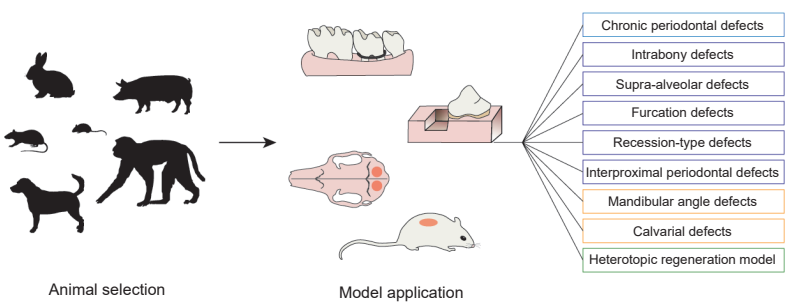

Various animal models used for testing biomaterials in periodontal regeneration are reviewed, including the chronic/acute periodontal defect model, mandibular angle defect model, calvarial defect model, and heterotopic regeneration model. Acute periodontal defects can be further categorised as intrabony defects, supra-alveolar defects, furcation defects, recession-type defects, and interproximal defects.

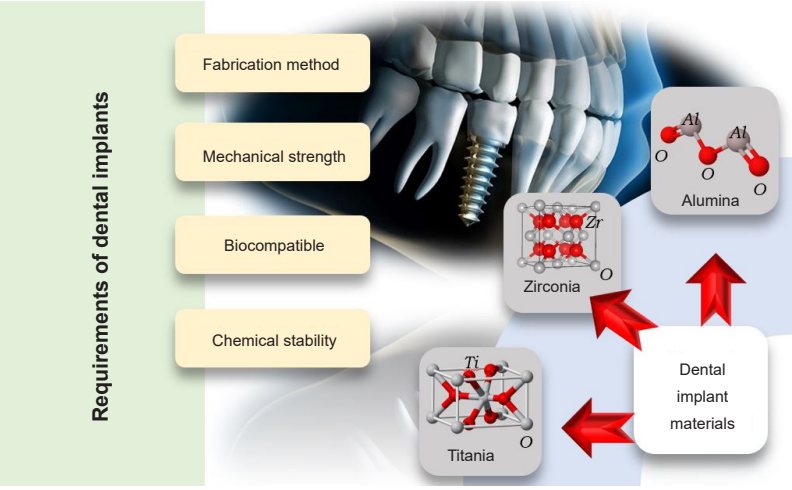

Dental implant material research aims to develop safe, durable, and biocompatible materials for dental implants. Researchers explore various materials, including metals (such as titanium), ceramics, polymers, and composites, considering factors such as strength, corrosion resistance, and bone integration.

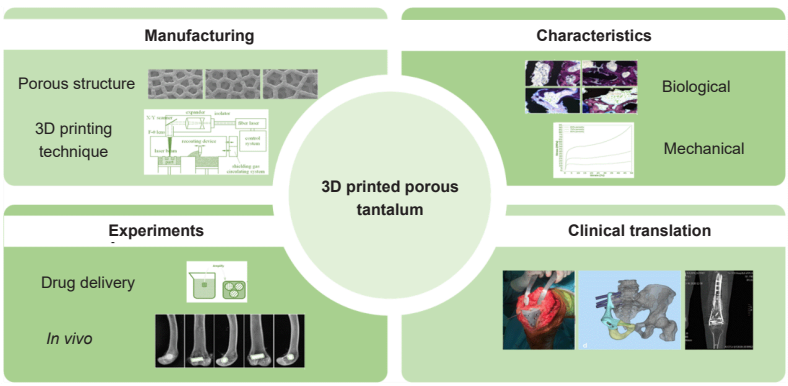

Recently, porous tantalum (Ta) metal has attracted more attention as a new orthopaedic implant material. With the deepening of research and the progress of technology, the advantages of porous Ta metal materials in terms of mechanics and biology have been gradually revealed. However, the mechanism of action involved in the biological effects of Ta metal requires more comprehensive and in-depth exploration, including the development of proteomics and genomics.

RESEARCH ARTICLE

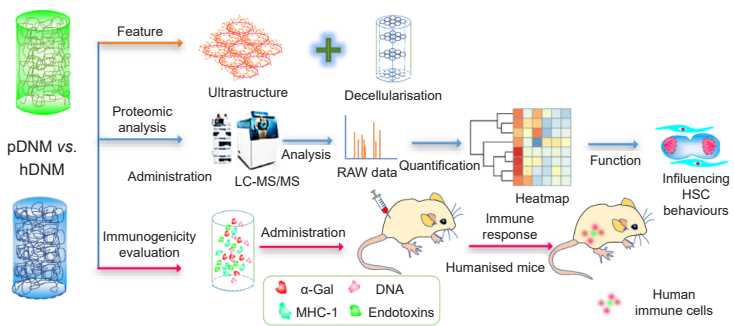

Comparative analysis of the features of ultrastructure, composition and matrix antigens, as well as the ability to provoke immune responses, of porcine decellularised nerve matrix (pDNM) and human decellularised nerve matrix (hDNM), provide the preliminary basic evidence for the utilisation of pDNM to replace human-derived decellularised nerve products for the repair of peripheral nerve damage.

The promise of serendipitous thinking

*Qian Wang**

I recently viewed a documentary series exploring Italian Renaissance Fresco art. While the photography quality was impeccable, and the selection of Frescos exemplary, I found myself disheartened by the narrow perspectives presented by a renowned contemporary painter. This artist's bias in favour of medieval Fresco art and lesser-known Italian masters led to a dismissive stance against the innovations of Renaissance art. He missed a crucial point – the greatness of Italian Renaissance art lies not in rigid adherence to religious themes but in its profound impact on humanity.

The Italian Renaissance was a movement dedicated to the pursuit of harmony between humanity and nature, nurturing dialogue among a spectrum of disciplines, including philosophy, literature, and the sciences. This intellectual blossoming was further enriched by advancements in fields such as anatomy, geometry, optics, and the chemistry of paints. This interplay between diverse fields and the freedom of intellectual exchanges ignited serendipitous thinking, serving as the cornerstone of Renaissance art achievement.

This phenomenon extends to the realm of science and technology.

I vividly recall an experience from 2008 when one of our research projects faced a serious roadblock. While culturing bone marrow-derived mesenchymal stem cells on the surface of mutant viruses, my student, Gagandeep Kaur, made an unexpected observation. Bone marrow-derived mesenchymal stem cells exhibited upregulated osteogenesis on the negative control – wild-type plant virus-coated surfaces.[1] Our repeating experiments consistently confirmed this curious result. Despite an exhaustive literature search, we could not find any existing theory to explain our findings.

It was during a visit to my dentist for an implantation surgery that serendipity struck. The dentist mentioned the use of mechanically sanded metal screws instead of traditional smooth screws in modern dental implants. Although the exact mechanism was unclear, these rougher screws seemed to integrate more favourably with the surrounding bone and marrow structures, leading to fewer implantation failures.

This "eureka" moment led to a realisation – the osteogenic effects observed on wild-type plant virus-based substrates likely stemmed from the specific topographical features provided by symmetrically organized capsid proteins, rather than specific functional units or binding epitopes as we had previously hypothesised.[2] This serendipitous event catalysed a new hypothesis: nanotopographical cues can significantly influence stem cell fate. Subsequently, our research group published numerous papers, including two in this journal,[3, 4] to validate this hypothesis.

Biomaterials Translational serves as a platform for cross-disciplinary subjects, welcoming comprehensive research and celebrating cutting-edge serendipitous discoveries. In this issue, three review papers,[5-7] a research article,[8] and a viewpoint essay[9] exemplify our commitment to these ideals.

My 3-year tenure as part of the editorial team of this journal has been a rewarding journey, especially as it coincided with the challenging period of the coronavirus disease 2019 (COVID-19) pandemic. I am grateful for the opportunity to collaborate with an exceptionally talented, dedicated, and professional team – Lijuan (Irene) Yang, Jie Yu, and Meng Zhao. As *Biomaterials Translational* transitions to a new editorial team, the journal remains constant in delivering interdisciplinary research in the expansive field of biomaterials science and translational research to you, our esteemed readers.

再见! Thank you for your readership!

Department of Chemistry and Biochemistry, University of South Carolina, Columbia, SC, USA

***Corresponding author:**
Qian Wang,
Wang263@mailbox.sc.edu.

http://doi.org/10.12336/biomatertransl.2023.03.001

How to cite this article:
Wang, Q. The promise of serendipitous thinking. *Biomater Transl.* **2023**, *4*(3), 129-130.

1. Kaur, G.; Valarmathi, M. T.; Potts, J. D.; Wang, Q. The promotion of osteoblastic differentiation of rat bone marrow stromal cells by a polyvalent plant mosaic virus. *Biomaterials.* **2008**, *29*, 4074-4081.
2. Metavarayuth, K.; Sitasuwan, P.; Luckanagul, J. A.; Feng, S.; Wang, Q. Virus nanoparticles mediated osteogenic differentiation of bone derived mesenchymal stem cells. *Adv Sci (Weinh).* **2015**, *2*, 1500026.
3. Metavarayuth, K.; Villarreal, E.; Wang, H.; Wang, Q. Surface topography and free energy regulate osteogenesis of stem cells: effects of shape-controlled gold nanoparticles. *Biomater Transl.* **2021**, *2*, 165-173.
4. Kingsak, M.; Maturavongsadit, P.; Jiang, H.; Wang, Q. Cellular responses to nanoscale substrate topography of TiO(2) nanotube arrays: cell morphology and adhesion. *Biomater Transl.* **2022**, *3*, 221-233.
5. Sun, Q.; Li, Y.; Luo, P.; He, H. Animal models for testing biomaterials in periodontal regeneration. *Biomater Transl.* **2023**, *4*, 142-150.
6. Thanigachalam, M.; Subramanian, A. V. M. Fabrication, microstructure and properties of advanced ceramic-reinforced composites for dental implants: a review. *Biomater Transl.* **2023**, *4*, 151-165.
7. Ying, J.; Yu, H.; Cheng, L.; Li, J.; Wu, B.; Song, L.; Yi, P.; Wang, H.; Liu, L.; Zhao D. Research progress and clinical translation of three-dimensional printed porous tantalum in orthopaedics. *Biomater Transl.* **2023**, *4*, 166-179.
8. Li, R.; Qiu, S.; Yang, W.; Rao, Z.; Chen, J.; Yang, Y.; Zhu, Q.; Liu, X.; Bai, Y.; Quan. D. A comparative study of human and porcine-derived decellularised nerve matrices. *Biomater Transl.* **2023**, *4*, 180-195.
9. Shi, T. L; Zhang, Y, F.; Yao, M. X.; Li, C.; Wang, H. C.; Ren, C.; Bai, J. S.; Cui, X.; Chen, W. Global trends and hot topics in clinical applications of perovskite materials: a bibliometric analysis. *Biomater Transl.* **2023**, *4*, 131-141.

Biomaterials Translational

Global trends and hot topics in clinical applications of perovskite materials: a bibliometric analysis

Tai-Long Shi[1,2,3,#], Yi-Fan Zhang[1,2,3,#], Meng-Xuan Yao[1,2,3], Chao Li[1,2,3], Hai-Cheng Wang[1,2,3], Chuan Ren[1,2,3], Jun-Sheng Bai[1,2,3], Xu Cui[4], Wei Chen[1,2,3,]*

Key Words:
bibliometrics; bibliometrix; CiteSpace; perovskite; R package

ABSTRACT

In recent years, perovskite has received increasing attention in the medical field. However, there has been a lack of related bibliometric analysis in this research field. This study aims to analyse the research status and hot topics of perovskite in the medical field from a bibliometric perspective and explore the research direction of perovskite. This study collected 1852 records of perovskite research in the medical field from 1983 to 2022 in the Web of Science (WOS) database. The country, institution, journal, cited references, and keywords were analysed using CiteSpace, VOS viewer, and Bibliometrix software. The number of articles related to perovskite research in the medical field has been increasing every year. China and USA have published the most papers and are the main forces in this research field. The University of London Imperial College of Science, Technology, and Medicine is the most active institution and has contributed the most publications. ACS Applied Materials & Interfaces is the most prolific journal in this field. "Medical electronic devices", "X-rays", and "piezoelectric materials" are the most researched directions of perovskite in the medical field. "Performance", "perovskite", and "solar cells" are the most frequently used keywords in this field. Advanced Materials is the most relevant and academically influential journal for perovskite research. Halide perovskites have been a hot topic in this field in recent years and will be a future research trend. X-ray, electronic medical equipment, and medical stents are the main research directions.

http://doi.org/10.12336/biomatertransl.2023.03.002

How to cite this article:
Shi, T. L; Zhang, Y, F.; Yao, M. X.; Li, C.; Wang, H. C.; Ren, C.; Bai, J. S.; Cui, X.; Chen, W. Global trends and hot topics in clinical applications of perovskite materials: a bibliometric analysis. *Biomater Transl.* **2023**, *4*(3), 131-141.

Introduction

Perovskite is a class of ceramic oxides named after their crystal structure, which is an octahedral cube with the general formula ABX_3. The A-site is usually composed of organic or inorganic cations (such as methylammonium, formamidinium, or inorganic cations Cs^+ or Rb^+); the B-site is composed of inorganic cations (Pb^{2+} or Sn^{2+}); and the X-site is composed of oxygen or halides (I, Br, or Cl). The surface adsorption of oxygen and lattice oxygen on perovskite affects its catalytic activity. At lower temperatures, surface adsorbed oxygen plays a major role in oxidation; at higher temperatures, lattice oxygen plays a role. Changing the metal elements at the A and B sites can regulate the number and activity of lattice oxygen. Substituting some of the +3-valent A and B atoms with +2 or +4-valent atoms can also generate lattice defects or lattice oxygen, thereby improving catalytic activity. This makes perovskites have excellent prospects in high-temperature catalysis and photocatalysis.[1]

In recent years, perovskites have been widely used in medical imaging. Medical X-ray imaging requires a reduction in diagnostic medical radiation to minimise its impact on patient health.[2, 3] Studies have shown that organic-metal perovskites prepared as thin films at low

temperatures and used in digital X-ray detectors have not only the advantages of low cost and large radiation area, but also low radiation dose.[4] Metal halide perovskites are a new type of optoelectronic material that can be used as a solution-deposited absorption layer in solar cells.[5] It also has the function of enhancing the water stability of halide perovskites and can be used for upconversion imaging in living cells.[6] Therefore, it has been widely used in the field of biological imaging. Due to the good biocompatibility and piezoelectric properties of perovskites, they are increasingly being manufactured as scaffolds for patients with fractures.[7] In addition, some materials can be simply encapsulated in a phospholipid protective layer through a thin film hydration method, which makes them have long-term waterproof characteristics and multi-functional biological imaging capabilities, and can be used for multi-cell imaging and *in vitro* tumour targeting.[8] Apart from high-temperature catalysis and photocatalysis, perovskite particles can also be used as catalysts for cellular metabolism.

Bibliometrics is the analysis of published information (such as books, journal articles, datasets, blogs) and their related metadata (such as abstracts, keywords, citations), using statistical data to describe or display relationships between published works. In recent years, bibliometric analysis has been used to analyse data, draw graphs, and show future research trends.[9] However, to date, no bibliometric analysis of the application of perovskites in the medical field has been found. Therefore, this study aims to analyse the research direction of perovskites in the medical field through bibliometric analysis, to understand related emerging frontier topics, and to provide direction for subsequent research.

Methods

Documents collection and retrieval strategy

We used the Web of Science (WOS) core collection database to search relevant publications on applications of perovskite in the medical field. The WOS database includes journals, books, patents, conference proceedings, and web resources. We chose the WOS database because it provides many articles with complete information.

The search formula used was: #1AND(#2OR#3)=[((ALL=(medical)) OR ALL=(medicine)) OR ALL=(biomedical)AND (((TS=(perovskite)) OR TI=(perovskite)) OR AB=(perovskite) OR((TS=($CaTiO_3$)) OR TI=($CaTiO_3$)) OR AB=($CaTiO_3$))]

Through the above search formula, a cross-sectional search was performed on December 17, 2022, and 1852 publications were retrieved from WOS in total. Finally, we reviewed and evaluated all available publication data to identify those that focused on "applications of perovskite in the medical field". **Figure 1** illustrates the search and exclusion protocols employed in this study for identifying suitable publications from the WOS database. The literature search was limited to English publications published between 1983 and 2022. In this study, our database only included research articles and reviews. The final screening results were exported to a dataset, including citation information (author, publication title, year of publication, source title, volume, issue, page numbers, citation count, source, and publication type) and bibliographic information (affiliation, editor, keywords, and funding details). The complete records of the retrieved articles were saved and downloaded from the WOS database and saved in BibTeX format for further analysis.

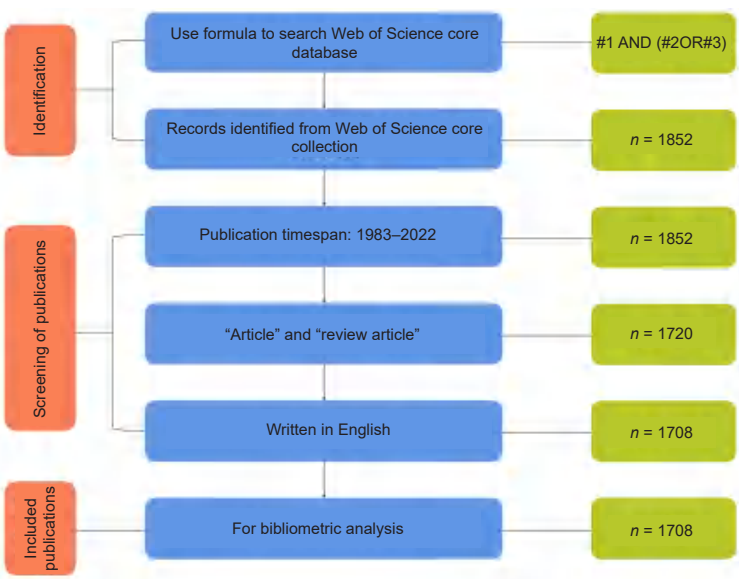

Figure 1. Flowchart for the selection of literature included in this study.

1 Department of Orthopaedic Surgery, Third Hospital of Hebei Medical University, Shijiazhuang, Hebei Province, China; 2 Key Laboratory of Biomechanics of Hebei Province, Shijiazhuang, Hebei Province, China; 3 NHC Key Laboratory of Intelligent Orthopaedic Equipment, Shijiazhuang, Hebei Province, China; 4 Center for Human Tissues and Organs Degeneration, Shenzhen Institute of Advanced Technology, Chinese Academy of Sciences, Shenzhen, Guangdong Province, China

***Corresponding author:** Wei Chen, surgeonchenwei@126.com.

#Author equally.

Analysis tools

To describe the characteristics of all literature related to "application of perovskite in the medical field", we used Bibliometrix (R Studio, V1.4, Posit Software, Boston, MA, USA)[10] and CiteSpace V5.8 R3 (Drexel University, Philadelphia, PA, USA)[11] to further analyse all eligible data.

Bibliometric analysis

The dataset was imported into Bibliometrix, which can analyse annual publishing trends and create line charts. In addition, it was also used to analyse the annual publishing trends of different countries and regions, as well as different journals. The bibliometrix package was employed to produce a word cloud and thematic map illustrating the top 100 high-frequency keywords. Thematic map starts with a co-occurring keyword network and draws a typified theme for a field in a two-dimensional map. The utilization of keyword+ (KWP) enables a more accessible interpretation of the research themes established within the framework. This analysis is conducted based on word or phrase occurrences that frequently appear in the reference titles cited within articles, but do not appear in the article titles themselves.

Results

General data

After searching the query, a total of 1852 articles were obtained. After undergoing additional screening, a total of 1708 articles met the inclusion criteria for the assessment system. **Table 1** presents the general information of all the included literature. The cumulative citation count for all the articles was 67,654, with an average citation frequency of 39.61 times per article. Among the included articles, there were 1584 research articles, comprising 92.7% of all publications, and 124 reviews, comprising 7.3% of all publications. Overall, 78 countries/regions, 1896 institutions, 7193 authors, and 447 journals have contributed to this field. The study also found that the number of articles published in journals increased between 2013 and 2022.

Table 1. General information of all publications on perovskite materials in the Web of Science database

Description	Results
Main information about data	
Timespan	1983–2022
Sources	447
Documents	1708
Annual growth rate (%)	4.11
Document average age (year)	5.66
Average citations per document	39.61
References	61233
Document contents	
Keywords plus (ID)	3480
Author's keywords (DE)	3714
Authors	
Total number of authors	7193
Authors of single-authored documents	15
Authors collaboration	
Single-authored documents	17
Co-authors per document	6.87
International co-authorships (%)	37.82
Document types	
Research article	1584
Review	124

Note: DE: the field identifier of the Author's Keywords; ID: the field identifier Of 'Keywords Plus' in the Web Of Science.

Publication trend

The number of newly published papers in the field of perovskite medical applications is depicted in **Figure 2**. The overall trajectory exhibits an upward trend, with a growth rate of 15.21%, dividing into two distinct periods. The first period spans from 1983 to 2012, during which the annual number of new publications in this field remained below 50. This period demonstrates a relatively stable trend, with an average annual growth rate of 8.38%. The second period covers the years 2013 to 2022, witnessing an annual increase of more than 50 publications, indicating a notable overall upward trend with an annual growth rate of 18.3%. It is worth noting that the number of new publications added in 2014 and 2016 is slightly lower than the previous year.

Country/region

Figure 3 presents a ranking of the top ten countries/regions that have made significant contributions in this field. China takes the lead with 2241 published papers, followed by USA with 529 papers, and UK with 458 papers. The region with the highest number of publications is Asia, accounting for 46.76% of all publications, followed by Europe, accounting for

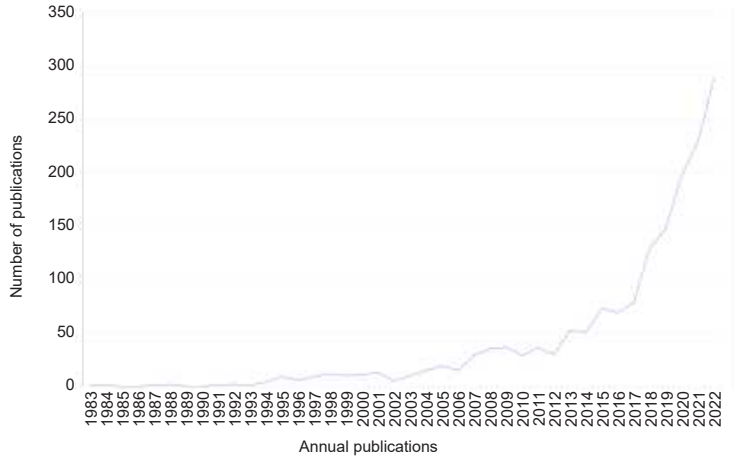

Figure 2. Number of publications related to novel clinical applications of perovskite materials in the Web of Science database (1983–2022).

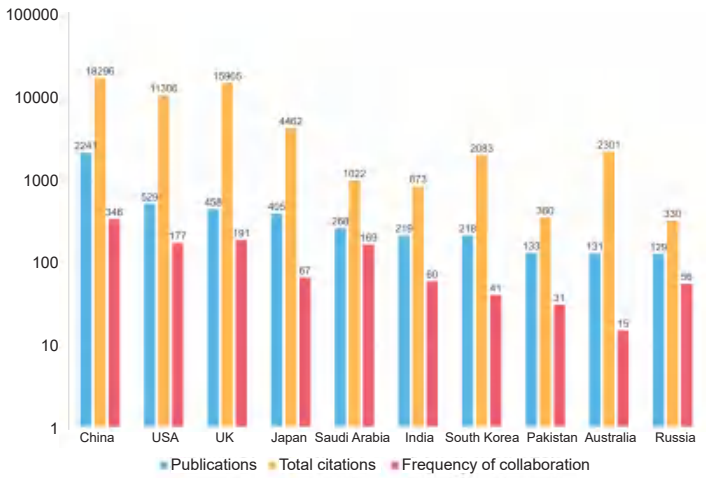

Figure 3. Top ten most productive countries/regions of all publications on perovskite materials in the Web of Science database.

30.23% of all publications. China is the most prolific country in Asia, and UKis the most prolific country in Europe. In terms of citations, China has the highest total number of citations (TC) (n = 18,296) and frequency of collaboration (n = 348); UK ranks second in TC (n = 15,905) and frequency of collaboration (n = 191); USA ranks third in TC (n = 11,306) and frequency of collaboration (n = 177).

Institution

Figure 4A shows the top ten institutions with the highest output in the field of perovskite medical applications based on the number of publications. The institution with the most publications is the University of London Imperial College of Science, Technology, and Medicine (210 publications), followed by the Chinese Academy of Sciences (91 publications) and King Saud University (59 publications). In terms of total citations, the University of London Imperial College of Science, Technology, and Medicine is again the top institution (with 18,834 citations), followed by the Chinese Academy of Sciences (3457 citations) and Southeast University (2334 citations). Among all institutions, London Imperial College of Science, Technology, and Medicine (with 90 citations per article) has the highest average citation frequency per article, followed by the National University of Singapore (72 citations per article) and the University of Cambridge (72 citations per article). Among the top ten most prolific institutions, five are in China, two are in the UK, and the other three are in Japan, Singapore, and Saudi Arabia.

In **Figure 4B**, a co-authorship network map of institutions is shown. The map reveals clusters of closely collaborating institutions. The largest cluster includes the Chinese Academy of Sciences, King Saud University, and the National University of Singapore, indicating that these institutions have close collaborative relationships, with the most participating institutions from China. Notable examples include the Imperial College of Science, Technology, and Medicine at the University of London and the Chinese Academy of Sciences.

Figure 4C shows a line chart that reflects the number of publications per year for the five most prolific institutions. The

University of London Imperial College of Science, Technology, and Medicine has been publishing articles in this field since 1997 and has the highest number of publications, citations, and average citations per article. The other four institutions started publishing more articles after 2015, with the Chinese Academy of Sciences showing a significant increase in publications since 2013. Southeast University has fewer publications than the Chinese Academy of Sciences, but it is also trending upward overall.

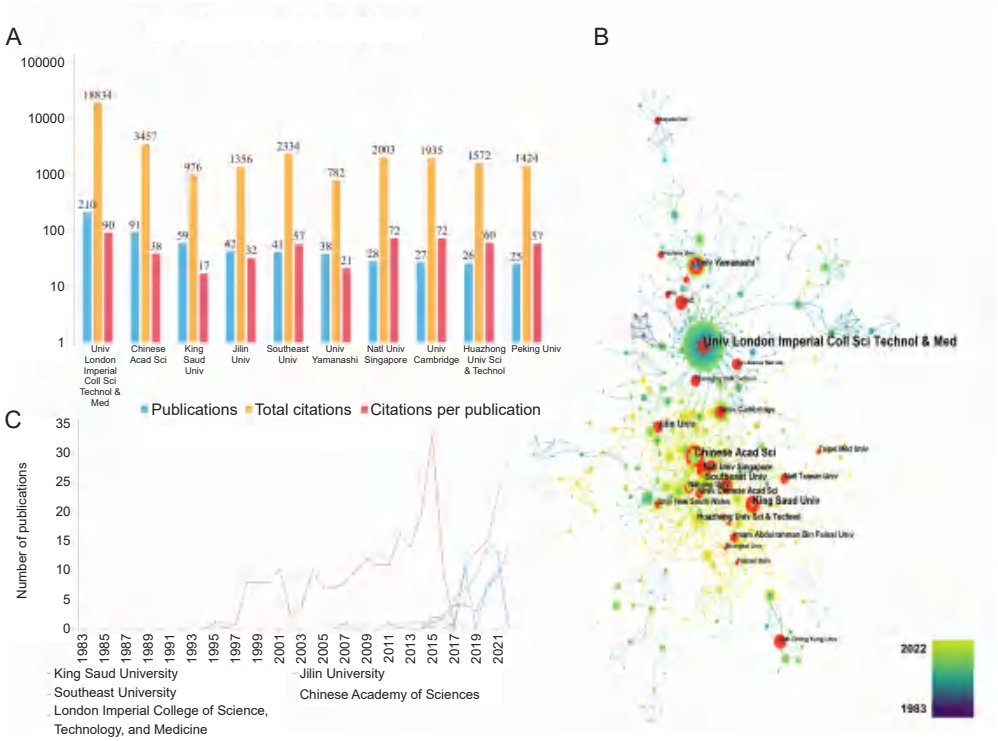

Figure 4. Keyword co-occurrence analysis of all publications on perovskite materials in the Web of Science database. (A) The number of articles published, the number of articles applied, and the average number of articles applied in VOS viewer. (B) Use VOS viewer to visualize the institutional co-occurrence network. Large nodes indicate that the occurrence rate of keywords is higher. The same colour indicates a close relationship. (C) Annual number of publications by the top five most productive institutions. In each group, the larger the node, the higher the frequency of the keyword; the denser the line, the closer their relationship. "Conversion" and "highly performance" not only have a high frequency of appearance, but also have a close relationship.

Journal

Table 2 shows the top nine most prolific journals and most cited journals in the field of perovskite materials. *ACS Applied Materials & Interfaces* (impact factor (2021) 10.38, Q1) is the most prolific journal with 46 publications (16.25% of the total), followed by *Solid State Ionics* (impact factor (2021) 3.70, Q2) with 40 publications, and *Chinese Chemical Letters* (impact factor (2021) 8.46, Q1) with 39 publications. In terms of citation and impact, *Solid State Ionics* ranks first (4396 TC, H-index 25), followed by *Advanced Materials* (2440 TC, H-index 21) and *ACS Applied Materials & Interfaces* (1051 TC, H-index 18). It's worth noting that the number of publications alone may not accurately reflect a country's or institution's influence in a given field. Therefore, we employed VOS viewer to identify the most frequently cited journals in the field of perovskite materials. The top three most cited journals are *Advanced Materials* (777 citations), *Journal of the American Chemical Society* (740 citations), and *Science* (736 citations).

Top cited articles

To ascertain the most influential research in this field, we utilized bibliometrics to extract the top ten most cited papers with the highest number of citations. The ten most cited papers are listed in **Table 3**. The most cited paper (73 local citations) was published by Yong Churl Kim in *Nature* in 2017, titled "*Printable organometallic perovskite enables large-area, low-dose X-ray imaging*". In this paper, the author discovered that perovskite films can control dark currents and instantaneous charge carrier transport, enabling low-dose X-ray imaging, as well as being used for radiation imaging, sensing, and energy harvesting photodetectors. In addition, four papers[12-15] reported on the relevant information of lead halide perovskites. Only one review introduces the past and present development of halide perovskite, as well as its prospects for the future.[12] The other three articles respectively introduce the relevant knowledge of halide perovskite with X-ray[13, 14] and gamma photons.[15]

Table 2. The top nine most prolific journals and co-cited journals with the most publications related to novel clinical applications of perovskite materials

Rank	Journal	Publications[a]	Total citations	H index	Impact factor (2021)	Co-cited journal	Co-citations	Impact factor (2021) of co-cited journal
1	*Solid State Ionics*	40	4396	25	3.7	*Advanced Materials*	777	32.09
2	*Advanced Materials*	29	2440	21	32.09	*Journal of the American Chemical Society*	740	16.38
3	*ACS Applied Materials & Interfaces*	46	1051	18	10.38	*Science*	736	63.71
4	*Journal of Materials Chemistry A*	24	1073	18	19.92	*Nature*	717	69.5
5	*Advanced Functional Materials*	30	1118	15	3.75	*Chemistry of Materials*	607	10.51
6	*Chemistry of Materials*	23	2263	15	10.51	*Nature Communications*	601	17.69
7	*Chinese Chemical Letters*	39	715	15	8.46	*ACS Applied Materials & Interfaces*	582	10.38
8	*Journal of Materials Chemistry C*	28	473	13	8.07	*Advanced Functional Materials*	574	19.92
9	*Journal of Alloys and Compounds*	24	595	12	6.37	*Nano Letters*	535	12.26

Note: [a]The publication refers to an article that has been published in a journal and expresses information and knowledge in a certain way, including text, images, and tables

Table 3. The top ten most cited publications with the most publications related to novel clinical applications of perovskite materials

Rank	First Author	Title	Local citations	Journal	Publication year
1	Yong Churl Kim	*Printable organometallic perovskite enables large-area, low-dose X-ray imaging*	73	*Nature*	2017
2	Qiushui Chen	*All-inorganic perovskite nanocrystal scintillators*	70	*Nature*	2018
3	Weicheng Pan	*$Cs_2AgBiBr_6$ single-crystal X-ray detectors with a low detection limit*	60	*Nature*	2017
4	Renzhong Zhuang	*Highly sensitive X-ray detector made of layered perovskite-like $(NH_4)_3Bi_2I_9$ single crystal with anisotropic response*	35	*Nature*	2019
5	Ajay Kumar Jena	*Halide perovskite photovoltaics: background, status, and future prospects*	31	*Chemical Reviews*	2019
6	Yuhai Zhang	*Metal halide perovskite nanosheet for Xray high-resolution scintillation imaging screens*	29	*ACS Nano*	2019
7	Yunxia Zhang	*Nucleation-controlled growth of superior lead-free perovskite $Cs_3Bi_2I_9$ single-crystals for high-performance X-ray detection*	29	*Nature Communications*	2020
8	Sergii Yakunin	*Detection of gamma photons using solution-grown single crystals of hybrid lead halide perovskites*	27	*Nature*	2016
9	M D Birowosuto	*X-ray scintillation in lead halide perovskite crystals*	24	*Scientific Reports*	2016
10	Weicheng Pan	*Hot-pressed $CsPbBr_3$ quasi-monocrystalline film for sensitive direct X-ray detection*	23	*Advanced Materials*	2019

Keywords' evolution

Keyword analysis is used to summarise and convey the thesis topic. **Figure 5A** shows co-occurring keyword analysis, grouping similar keywords together using "site space". The study merges 50 keywords into 14 groups, such as energy transfer, colloidal synthesis, and highly luminescent, which can be grouped under nanocrystal. The research hotspots are "oxidation," "hybrid perovskite", and "carbon nanotube".

Figure 5B lists the most commonly used keywords, with larger font sizes indicating higher citation frequencies. The top ten most frequently used keywords are "performance" (n = 168), "perovskite" (n = 141), "solar-cells" (n = 127), "efficient" (n = 122), "stability" (n = 111), "nanocrystals" (n = 107), "films" (n = 85), "temperature" (n = 84), "nanoparticles" (n = 82), and "transport" (n = 81).

Figure 5C illustrates the top 25 keywords exhibiting notable citation bursts in the field of perovskites. The active and non-active periods are represented by red and blue, respectively. Starting from 2010, keywords such as "nanocrystal", "Br", "Cl", "photoconductor" and "semiconductor" have been consistently utilized.

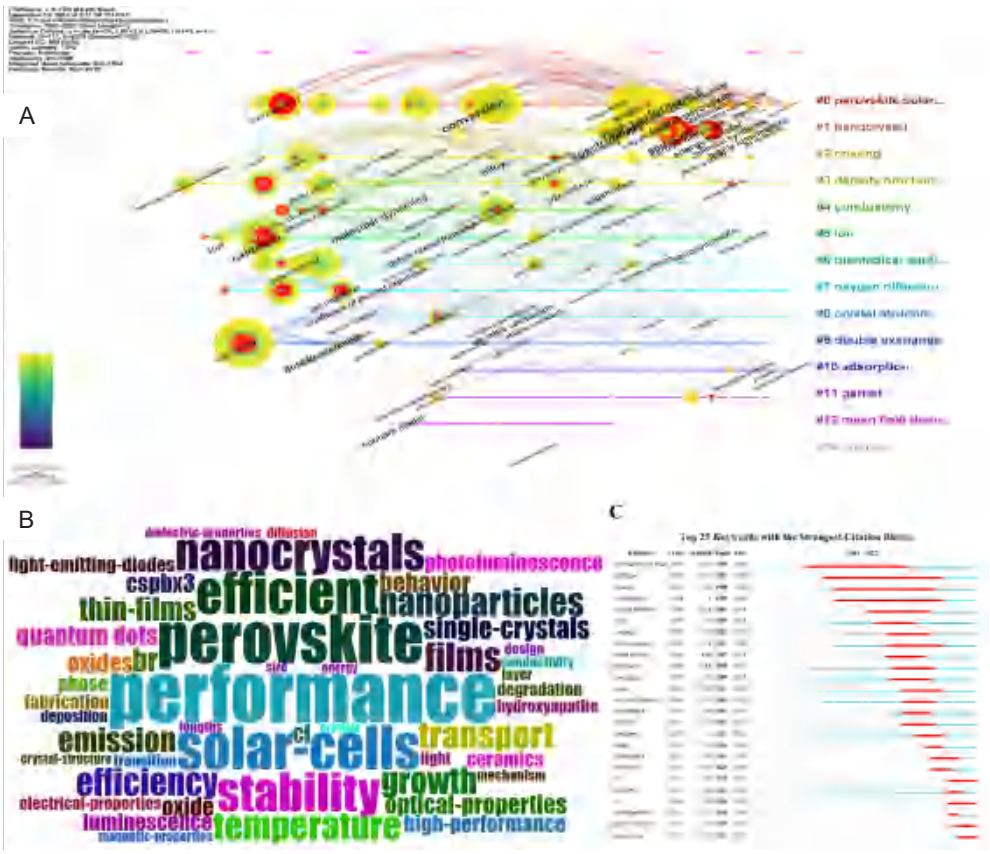

Figure 5. Keyword co-occurrence analysis of all publications on perovskite materials in the Web of Science database. (A) Use VOS viewer to visualize author keyword co-occurrence network. (B) Keywords that appear the most. The larger the font, the higher the frequency of keywords. (C) The initial keyword with the most significant citation burst signifies the prominent topics during different time periods. The red bars indicate the duration of the burst period, highlighting the intensification of interest. The strength of the burst indicates the importance of the topic to the field of study.

Discussion

Over the past few decades, researchers have conducted extensive studies on the application of perovskites in the medical field. A comprehensive analysis of research related to perovskites was conducted using bibliometric analysis, exploring publications, countries, institutions, journals, most cited articles, and keywords.

Global publication trends and countries/regions

The increasing number of publications in the field of perovskite medical applications indicates a growing interest and research focus in this area. The steady increase in the number of newly published papers since 2013 suggests that researchers are recognising the potential of perovskite materials in medical applications. The involvement of multiple countries, institutions, authors, and journals highlights the collaborative nature of research in this field. Collaboration between different entities can lead to the exchange of ideas, expertise, and resources, contributing to scientific advancements. China emerges as the leading contributor in terms of the number of published papers. This demonstrates China's active involvement and significant research output in perovskite

medical applications. It also reflects China's commitment to scientific research and development. Among them, the high efficiency and low cost of perovskite solar cells made in China have attracted worldwide attention.[16]

Asia and Europe are the leading regions in terms of publication output. This suggests that researchers from these regions are at the forefront of exploring the applications of perovskite materials in medicine. The high number of publications from these regions signifies their expertise and contributions to the field. The cumulative citation count and average citation frequency indicate the impact and visibility of the published articles. A higher number of citations suggests that the research conducted in this field has gained attention and recognition within the scientific community. Overall, the analysis underscores the growing research interest in perovskite medical applications, the collaborative nature of scientific exploration, and the significant contributions of China, Asia, and Europe in advancing this field. These findings provide a foundation for further research and development in leveraging perovskite materials for medical applications.

Institutions

The influence and contribution of research institutions represent the research level of a country or region. Among the top ten most prolific institutions, five are in China and two are located in UK. The University of London Imperial College of Science, Technology and Medicine in UK is the most productive institution, publishing the most papers on the application of perovskites in the medical field, and each paper is cited on average the most times. This research institution focuses on the problems and solutions encountered in the application of halide perovskites. Their recent research shows that tin halide perovskites are the preferred option for lead-free perovskite optoelectronic devices.[17] In China, the institution with the most papers and citations is the Chinese Academy of Sciences, which has focused on perovskite solar cells in recent years.

Journals and co-citation journals

In terms of publication output, *ACS Applied Materials & Interfaces* is the most prolific journal with 46 publications, representing 16.25% of the total. It is followed by *Solid State Ionics* with 40 publications and *Chinese Chemical Letters* with 39 publications. These journals have a significant contribution to the dissemination of research in the field. However, when considering citation impact, *Solid State Ionics* ranks first with 4396 total citations and a 25-H-index. This indicates that the articles published in *Solid State Ionics* have generated a substantial impact and have been widely cited.

Furthermore, it is important to note that the number of publications alone may not accurately reflect the influence of a country or institution in a specific field. Therefore, additional analysis was conducted using VOS viewer to identify frequently cited journals in the field of perovskite materials. The results reveal that *Advanced Materials* is the most frequently cited journal, with 777 citations. It is followed by *Journal of the American Chemical Society* with 740 citations and Science with 736 citations. These highly cited journals indicate their significance and impact in the field of perovskite materials research.

In conclusion, while *ACS Applied Materials & Interfaces*, *Solid State Ionics*, and *Chinese Chemical Letters* are the top prolific journals in terms of publication output, *Advanced Materials*, *Journal of the American Chemical Society*, and *Science* are the most frequently cited journals, highlighting their influence and importance in the field. Researchers should consider publishing their work in these high-impact journals to maximise visibility and potential citations.

Most cited references

Among all publications, the article most frequently cited is "*Printable organometallic perovskite enables large-area, low-dose X-ray imaging*" by Kim et al.[4] The authors found that solution-processed perovskite detectors can achieve low-dose X-ray imaging and can also be used for radiation imaging, sensing, and energy harvesting in optoelectronic devices. This article provides theoretical support for the widespread application of perovskites in X-ray medical imaging in the future. The most cited review is "*Halide perovskite photovoltaics: background, status, and future prospects*" by Jena et al.,[12] which is a comprehensive review of past research, current status, and future prospects of halide perovskites. The article focuses on summarizing the principles and latest advances in X-ray detectors and solar cells, laying the foundation for future related research.

Research hotspots and frontier trends

In the past, research on perovskite materials was mainly focused on inorganic oxides, such as ceramics, hydroxyapatite, and perovskite-type oxide. As research continues to deepen, halide and organic oxides are also receiving attention. The physical and chemical properties of perovskites, such as hysteresis, electrical properties, and conductivity, have always been a focus of research.

Perovskites and X-rays

X-rays play a crucial role in the medical field due to their penetrating effect, differential absorption, photosensitivity, and fluorescence. They can assist doctors in diagnosing diseases more accurately.[18] However, X-rays are also one of the most widely used sources of radiation in medical diagnosis and treatment, and ionisation and radiation can cause protein decomposition, leading to damage to the human body. Long-term radiation exposure can cause DNA molecule breakage and increase the risk of cancer.[19, 20] Therefore, reducing radiation and improving imaging quality is an urgent problem that needs to be addressed. In recent years, scientists have found that materials such as $(NH_4)_3Bi_2I_9$ single crystals, $Cs_3Bi_2I_9$ perovskite single crystals, and colloidal perovskite nanosheets ($CsPbBr_3$) have high sensitivity, low radiation, and high imaging quality.[13, 21] This shows that perovskites can reduce radiation and improve X-ray imaging quality, further improving their clinical applications.

Perovskites and medical electronic devices

With the development of society, energy demand is constantly increasing, and innovative solutions for efficient energy

harvesting are needed. In modern medical diagnostic and treatment methods, implantable biomedical electronic devices can improve patients' clinical outcomes and provide a large amount of data about the patients themselves, so they need to be small and lightweight. However, energy storage is still one of the obstacles affecting energy applications.[22, 23] The development of medical electronic devices aims to reduce energy consumption while also being able to extract energy from the environment, and solar cells are just the right solution. Sunlight is the easiest to obtain and cleanest source of energy. After the battery is implanted under the skin, it can obtain energy through solar radiation. However, the application of solar cells in the human body is limited by many factors. Firstly, they need to have good biocompatibility. Poon et al.'s experiment[24] has shown that cells grown on perovskite material surfaces have good metabolism and can be implanted in the human body for a long time while also having good piezoelectric properties. In terms of optical properties, Aminzare et al.[25] found that perovskites also exhibit efficient radiation recombination and coordinated spectral emission, with good photoelectric properties.

However, perovskite solar cells also have some problems, such as the incompatibility of halide ions with other ions, which can become charge traps and aggravate ion migration, severely affecting the efficiency and stability of the battery. Trap-mediated nonradiative charge recombination at the surface is one of the main limitations for achieving highly efficient metal halide perovskite photovoltaics.[26, 27] Zhang et al.[28] found that dual-functional cellulose can significantly reduce trap states, thus significantly suppressing nonradiative recombination and improving the power conversion efficiency of perovskite solar cells. Polyethylene glycol diacrylate can passivate surface defects in perovskite thin films to improve power conversion efficiency.[29] The defects in perovskite solar cells can be compensated for by other materials, and new materials are constantly being discovered and manufactured.

Perovskites and medical materials

Bones have strong regenerative abilities, but when the body's self-healing ability is exceeded, transplantation is required. Autogenous bone transplantation and allogeneic bone transplantation are not widely applicable due to quantity limitations. Therefore, suitable scaffolds are crucial for bone fracture healing.[30] There are many types of materials used to make scaffolds, including metal materials, polymer materials, and inorganic materials.[31] Regardless of the material used, good biocompatibility, biodegradability, and mechanical strength are required.[32] Metal materials such as Mg and Zn can promote bone generation but have moderate mechanical properties. Polymer materials such as polylactic acid have good flexibility but are brittle. Inorganic materials such as hydroxyapatite have good biocompatibility but poor mechanical strength. These materials all have advantages and disadvantages and can be improved or combined with other materials to make scaffolds to help patients with bone fractures recover.[33, 34] In recent years, biocompatible piezoelectric materials have received widespread attention due to their piezoelectric properties similar to those of human bones.[35] Biocompatible piezoelectric materials can come into contact and interact with human tissues in the body, produce local currents, restore damaged electrophysiological microenvironments, and promote bone regeneration.[36, 37] Some perovskites have piezoelectric properties, which have great potential in scaffold preparation. Bagchi et al.[7] found that perovskite ceramics such as calcium titanate and strontium titanate are compatible with cells, significantly enhance the expression of osteogenic genes, and promote bone regeneration. Dai et al.[38] found that barium titanate and polylactic acid piezoelectric composite materials can promote bone tissue regeneration and have strong osteogenic effects.

Perovskites and enzymes

There are many ways to treat cancer, and inducing cell pyroptosis is one of the new treatment methods. Pyroptosis is a new type of cell death that also belongs to programmed cell death, including membrane perforation, cell swelling, and cell rupture.[39] Unlike apoptosis, pyroptotic cells swell and release cell contents, such as the typical inflammasome.[40] Chang et al.[41] found that perovskite nanoenzymes can induce cell pyroptosis and have significant therapeutic effects on cancer through *in vitro* cell and *in vivo* animal experiments. In addition to direct application in clinical treatment, perovskites can also be used in biochemical research. Nanoenzymes synthesised by perovskite oxide $BiFeO_3$ have peroxidase-like activity and can measure creatinine levels in human serum.[42]

Limitations

There are several limitations to current research. First, only one database (WOS) was searched, and other databases and sources of information are not included in the bibliometric analysis of this article. Therefore, some potentially valuable information may have been missed. Second, because many authors are from China and their name abbreviations are repeated, no research was conducted in the "Results" section. Third, bibliometric analysis often uses citations to evaluate publishing quality. The application of perovskite in the medical field needs more study and more in-depth and comprehensive research.

Conclusion

In conclusion, research on perovskite materials in the medical field has been on the rise over the past 40 years, with a significant increase in the number of publications in the last 20 years. China has emerged as a major contributor to this field with the largest number of publications and collaborations with other countries. There is great potential for China to further develop its research in this area in the future.

Advanced Materials is the most relevant and influential journal in the field of perovskite research in medicine. Halide perovskites have become a hot research topic in recent years and are expected to be a future research trend. X-rays, medical electronic devices, and medical materials are the main research directions.

Author contributions

Design: WC; data collect: MXY; data analysis: TLS, MXY, YFZ, JSB; manuscript draft: TLS, CR; manuscript revision: TLS, HCW, XC, CL, WC. All authors have read and approved the final version of the manuscript.

Financial support

This work was supported by Key Supported Projects of the Joint Fund of the National Natural Science Foundation of China, No. U22A20357, the National Key R&D Program of China, No. 2020YFC1107601, and the Natural Science Foundation of Hebei Province – for Distinguished Young Scholars, No. H2021206329.

Acknowledgement

None.

Conflicts of interest statement

All authors declare that they have no conflict of interest.

1. Correa-Baena, J. P.; Saliba, M.; Buonassisi, T.; Grätzel, M.; Abate, A.; Tress, W.; Hagfeldt, A. Promises and challenges of perovskite solar cells. *Science*. **2017**, *358*, 739-744.
2. Sinnott, B.; Ron, E.; Schneider, A. B. Exposing the thyroid to radiation: a review of its current extent, risks, and implications. *Endocr Rev*. **2010**, *31*, 756-773.
3. Meedeniya, D.; Kumarasinghe, H.; Kolonne, S.; Fernando, C.; Díez, I. T.; Marques, G. Chest X-ray analysis empowered with deep learning: a systematic review. *Appl Soft Comput*. **2022**, *126*, 109319.
4. Kim, Y. C.; Kim, K. H.; Son, D. Y.; Jeong, D. N.; Seo, J. Y.; Choi, Y. S.; Han, I. T.; Lee, S. Y.; Park, N. G. Printable organometallic perovskite enables large-area, low-dose X-ray imaging. *Nature*. **2017**, *550*, 87-91.
5. Protesescu, L.; Yakunin, S.; Bodnarchuk, M. I.; Krieg, F.; Caputo, R.; Hendon, C. H.; Yang, R. X.; Walsh, A.; Kovalenko, M. V. Nanocrystals of cesium lead halide perovskites ($CsPbX_3$, X = Cl, Br, and I): novel optoelectronic materials showing bright emission with wide color gamut. *Nano Lett*. **2015**, *15*, 3692-3696.
6. Talianov, P. M.; Peltek, O. O.; Masharin, M.; Khubezhov, S.; Baranov, M. A.; Drabavičius, A.; Timin, A. S.; Zelenkov, L. E.; Pushkarev, A. P.; Makarov, S. V.; Zyuzin, M. V. Halide perovskite nanocrystals with enhanced water stability for upconversion imaging in a living cell. J *Phys Chem Lett*. **2021**, *12*, 8991-8998.
7. Bagchi, A.; Meka, S. R.; Rao, B. N.; Chatterjee, K. Perovskite ceramic nanoparticles in polymer composites for augmenting bone tissue regeneration. *Nanotechnology*. **2014**, *25*, 485101.
8. Yang, Z.; Xu, J.; Zong, S.; Xu, S.; Zhu, D.; Zhang, Y.; Chen, C.; Wang, C.; Wang, Z.; Cui, Y. Lead halide perovskite nanocrystals-phospholipid micelles and their biological applications: multiplex cellular imaging and in vitro tumor targeting. *ACS Appl Mater Interfaces*. **2019**, *11*, 47671-47679.
9. Wu, K.; Liu, Y.; Liu, L.; Peng, Y.; Pang, H.; Sun, X.; Xia, D. Emerging trends and research foci in tumor microenvironment of pancreatic cancer: a bibliometric and visualized study. *Front Oncol*. **2022**, *12*, 810774.
10. Aria, M.; Cuccurullo, C. bibliometrix: An R-tool for comprehensive science mapping analysis. *J Informetr*. **2017**, *11*, 959-975.
11. Mao, M.; Zhou, Y.; Jiao, Y.; Yin, S.; Cheung, C.; Yu, W.; Gao, P.; Yang, L. Bibliometric and visual analysis of research on the links between the gut microbiota and pain from 2002 to 2021. *Front Med (Lausanne)*. **2022**, *9*, 975376.
12. Jena, A. K.; Kulkarni, A.; Miyasaka, T. Halide perovskite photovoltaics: background, status, and future prospects. *Chem Rev*. **2019**, *119*, 3036-3103.
13. Zhang, Y.; Sun, R.; Ou, X.; Fu, K.; Chen, Q.; Ding, Y.; Xu, L. J.; Liu, L.; Han, Y.; Malko, A. V.; Liu, X.; Yang, H.; Bakr, O. M.; Liu, H.; Mohammed, O. F. Metal halide perovskite nanosheet for X-ray high-resolution scintillation imaging screens. *ACS Nano*. **2019**, *13*, 2520-2525.
14. Birowosuto, M. D.; Cortecchia, D.; Drozdowski, W.; Brylew, K.; Lachmanski, W.; Bruno, A.; Soci, C. X-ray scintillation in lead halide perovskite crystals. *Sci Rep*. **2016**, *6*, 37254.
15. Yakunin, S.; Dirin, D. N.; Shynkarenko, Y.; Morad, V.; Cherniukh, I.; Nazarenko, O.; Kreil, D.; Nauser, T.; Kovalenko, M. V. Detection of gamma photons using solution-grown single crystals of hybrid lead halide perovskites. *Nat Photon*. **2016**, *10*, 585-589.
16. Cui, D.; Wang, Y.; Han, L. China's progress of perovskite solar cells in 2019. *Sci Bull (Beijing)*. **2020**, *65*, 1306-1315.
17. Lanzetta, L.; Webb, T.; Marin-Beloqui, J. M.; Macdonald, T. J.; Haque, S. A. Halide chemistry in tin perovskite optoelectronics: bottlenecks and opportunities. *Angew Chem Int Ed Engl*. **2023**, *62*, e202213966.
18. Pu, H.; Gao, P.; Rong, J.; Zhang, W.; Liu, T.; Lu, H. Spectral-resolved cone-beam X-ray luminescence computed tomography with principle component analysis. *Biomed Opt Express*. **2018**, *9*, 2844-2858.
19. Sauer, K.; Zizak, I.; Forien, J. B.; Rack, A.; Scoppola, E.; Zaslansky, P. Primary radiation damage in bone evolves via collagen destruction by photoelectrons and secondary emission self-absorption. *Nat Commun*. **2022**, *13*, 7829.
20. Shi, H. M.; Sun, Z. C.; Ju, F. H. Recommendations for reducing exposure to medical X-ray irradiation (review). *Med Int (Lond)*. **2022**, *2*, 22.
21. Zhang, Y.; Liu, Y.; Xu, Z.; Ye, H.; Yang, Z.; You, J.; Liu, M.; He, Y.; Kanatzidis, M. G.; Liu, S. F. Nucleation-controlled growth of superior lead-free perovskite Cs(3)Bi(2)I(9) single-crystals for high-performance X-ray detection. *Nat Commun*. **2020**, *11*, 2304.
22. Norton, C.; Hassan, U. Bioelectronic sensor with magnetic modulation to quantify phagocytic activity of blood cells employing machine learning. *ACS Sens*. **2022**, *7*, 1936-1945.
23. Klimpel, M.; Kovalenko, M. V.; Kravchyk, K. V. Advances and challenges of aluminum-sulfur batteries. *Commun Chem*. **2022**, *5*, 77.
24. Poon, K. K.; Wurm, M. C.; Evans, D. M.; Einarsrud, M. A.; Lutz, R.; Glaum, J. Biocompatibility of (Ba,Ca)(Zr,Ti)O(3) piezoelectric ceramics for bone replacement materials. *J Biomed Mater Res B Appl Biomater*. **2020**, *108*, 1295-1303.
25. Aminzare, M.; Jiang, J.; Mandl, G. A.; Mahshid, S.; Capobianco, J. A.; Dorval Courchesne, N. M. Biomolecules incorporated in halide perovskite nanocrystals: synthesis, optical properties, and applications. *Nanoscale*. **2023**, *15*, 2997-3031.
26. Wang, R.; Xue, J.; Wang, K. L.; Wang, Z. K.; Luo, Y.; Fenning, D.; Xu, G.; Nuryyeva, S.; Huang, T.; Zhao, Y.; Yang, J. L.; Zhu, J.; Wang, M.; Tan, S.; Yavuz, I.; Houk, K. N.; Yang, Y. Constructive molecular configurations for surface-defect passivation of perovskite photovoltaics. *Science*. **2019**, *366*, 1509-1513.
27. Gu, X.; Xiang, W.; Tian, Q.; Liu, S. F. Rational surface-defect control via designed passivation for high-efficiency inorganic perovskite solar cells. *Angew Chem Int Ed Engl*. **2021**, *60*, 23164-23170.
28. Zhang, Z.; Wang, C.; Li, F.; Liang, L.; Huang, L.; Chen, L.; Ni, Y.; Gao, P.; Wu, H. Bifunctional cellulose interlayer enabled efficient perovskite solar cells with simultaneously enhanced efficiency and stability. *Adv Sci (Weinh)*. **2023**, *10*, e2207202.
29. Xu, W.; Zhu, T.; Wu, H.; Liu, L.; Gong, X. Poly(ethylene glycol) diacrylate as the passivation layer for high-performance perovskite solar cells. *ACS Appl Mater Interfaces*. **2020**, *12*, 45045-45055.

30. Sun, Y.; Jia, X.; Meng, Q. Characteristic evaluation of recombinant MiSp/poly(lactic-co-glycolic) acid (PLGA) nanofiber scaffolds as potential scaffolds for bone tissue engineering. *Int J Mol Sci.* **2023**, *24*, 1219.
31. Li, Y.; Chen, S. K.; Li, L.; Qin, L.; Wang, X. L.; Lai, Y. X. Bone defect animal models for testing efficacy of bone substitute biomaterials. *J Orthop Translat.* **2015**, *3*, 95-104.
32. Li, C.; Lv, H.; Du, Y.; Zhu, W.; Yang, W.; Wang, X.; Wang, J.; Chen, W. Biologically modified implantation as therapeutic bioabsorbable materials for bone defect repair. *Regen Ther.* **2022**, *19*, 9-23.
33. Jodati, H.; Evis, Z.; Tezcaner, A.; Alshemary, A. Z.; Motameni, A. 3D porous bioceramic based boron-doped hydroxyapatite/baghdadite composite scaffolds for bone tissue engineering. *J Mech Behav Biomed Mater.* **2023**, *140*, 105722.
34. Kulkarni, N. B.; Goyal, S. Comparison of bracket failure rate between two different materials used to fabricate transfer trays for indirect orthodontic bonding. *J Contemp Dent Pract.* **2022**, *23*, 307-312.
35. Khare, D.; Basu, B.; Dubey, A. K. Electrical stimulation and piezoelectric biomaterials for bone tissue engineering applications. *Biomaterials.* **2020**, *258*, 120280.
36. Xu, Q.; Gao, X.; Zhao, S.; Liu, Y. N.; Zhang, D.; Zhou, K.; Khanbareh, H.; Chen, W.; Zhang, Y.; Bowen, C. Construction of bio-piezoelectric platforms: from structures and synthesis to applications. *Adv Mater.* **2021**, *33*, e2008452.
37. Mokhtari, F.; Azimi, B.; Salehi, M.; Hashemikia, S.; Danti, S. Recent advances of polymer-based piezoelectric composites for biomedical applications. *J Mech Behav Biomed Mater.* **2021**, *122*, 104669.
38. Dai, X.; Yao, X.; Zhang, W.; Cui, H.; Ren, Y.; Deng, J.; Zhang, X. The osteogenic role of barium titanate/polylactic acid piezoelectric composite membranes as guiding membranes for bone tissue regeneration. *Int J Nanomedicine.* **2022**, *17*, 4339-4353.
39. Wang, S.; Liao, X.; Xiong, X.; Feng, D.; Zhu, W.; Zheng, B.; Li, Y.; Yang, L.; Wei, Q. Pyroptosis in urinary malignancies: a literature review. *Discov Oncol.* **2023**, *14*, 12.
40. Li, L.; Wang, S.; Zhou, W. Balance cell apoptosis and pyroptosis of caspase-3-activating chemotherapy for better antitumor therapy. *Cancers (Basel).* **2022**, *15*, 26.
41. Chang, M.; Wang, Z.; Dong, C.; Zhou, R.; Chen, L.; Huang, H.; Feng, W.; Wang, Z.; Wang, Y.; Chen, Y. Ultrasound-amplified enzyodynamic tumor therapy by perovskite nanoenzyme-enabled cell pyroptosis and cascade catalysis. *Adv Mater.* **2023**, *35*, e2208817.
42. Zhu, J.; Pan, J.; Li, Y.; Yang, J.; Ye, B. Enzyme-nanozyme cascade colorimetric sensor platform: a sensitive method for detecting human serum creatinine. *Anal Bioanal Chem.* **2022**, *414*, 6271-6280.

Received: August 16, 2023
Revised: September 9, 2023
Accepted: September 12, 2023
Available online: September 28, 2023

Animal models for testing biomaterials in periodontal regeneration

Qiao Sun[1], Yicun Li[3], Ping Luo[1], Hong He[1,2,]*

Key Words:
animal model; biomaterials; periodontitis; tissue regeneration

From the Contents

ABSTRACT

Periodontitis is a prevalent oral disease. It can cause tooth loss and has a significant impact on patients' quality of life. While existing treatments can only slow the progression of periodontitis, they are unable to achieve complete regeneration and functional reconstruction of periodontal tissues. As a result, regenerative therapies based on biomaterials have become a focal point of research in the field of periodontology. Despite numerous studies reporting the superiority of new materials in periodontal regeneration, limited progress has been made in translating these findings into clinical practice. This may be due to the lack of appropriate animal models to simulate the tissue defects caused by human periodontitis. This review aims to provide an overview of established animal models for periodontal regeneration, examine their advantages and limitations, and outline the steps for model construction. The objective is to determine the most relevant animal models for periodontal regeneration based on the hypothesis and expected outcomes.

***Corresponding author:**
Hong He,
drhehong@whu.edu.cn.

http://doi.org/10.12336/biomatertransl.2023.03.003

How to cite this article:
Sun, Q.; Li, Y.; Luo, P.; He, H. Animal models for testing biomaterials in periodontal regeneration. *Biomater Transl.* **2023**, *4*(3), 142-150.

Introduction

Periodontitis is a chronic inflammatory disease characterised by progressive destruction of the periodontium, including the gingiva, alveolar bone, periodontal ligament, and cementum. The disease affects about 20–50% of global population, with clinical manifestations such as gingival recession, tooth mobility, and tooth loss.[1] The primary cause of periodontitis is subgingival dental biofilm, which is why traditional treatments aim to control biofilm and reduce inflammation to halt the progression of the disease.[2] However, such treatments are limited in their ability to reverse tissue loss and reconstruct the biomechanical support of the teeth.[2] To address these limitations, regenerative therapies aimed at reconstructing all elements of the periodontium have become a central focus in the field of periodontology. These therapies strive to restore both the structure and function of the periodontium over previously diseased teeth.

Periodontal regeneration is an approach that leverages biomaterials to support tissue growth and repair. By utilizing biomaterials that create a supportive environment and incorporating growth factors and stem cells, periodontal regeneration aims to recreate a functional interface between the various components of the periodontium. Guided tissue regeneration concepts are applied through the use of barrier biomaterials to direct periodontal ligament stem cells and facilitate connective tissue attachment.[3,4] Bone grafting materials, such as autogenous and allograft bone and bone substitutes, are used to fill bone defects and promote bone and cementum regeneration.

Despite promising results from preclinical studies, the clinical outcomes of periodontal regeneration remain limited and unpredictable.[5] To fully restore the mechanical structure of the periodontium, it is necessary to recreate the functional interface between all components of the periodontium. To this end, the regenerative effects of biomaterials must be validated in similar tissue defects prior to their clinical application.

At present, a variety of animal models have been employed to model periodontitis or similar

periodontal defects, including rats, dogs, rabbits, miniature pigs, and non-human primates.[6-8] Large animals are preferred for their similarity in anatomy and physiology to humans, but ethical considerations limit their use. Smaller animals, such as rats and rabbits, are more cost-effective and convenient, and are often used in the early stages of material testing.

To model periodontal defects in animals, various surgical and ligature-induced models have been established, including supra-alveolar defects,[9] dehiscence defects,[10] furcation defects,[11] fenestration defects[12] and intrabony defects.[13] In these models, periodontal ligament and cementum are completely removed to reproduce the characteristics of human periodontal defects.

This review summarises the various animal models used for periodontal regeneration, detailing their advantages and procedures for establishing periodontal defects.

Literature Search

The articles about animal models for testing biomaterials in periodontal regeneration were retrieved by the search terms: ("periodontal regeneration" OR "periodontal tissue engineering") AND ("animal model" OR model OR preclinical) AND (biomaterial OR biomaterials). These searches were performed on Medicine in December, 2022. A total of 185 records were retrieved and carefully screened for eligibility. Finally, 114 articles were included in this review (**Figure 1**).

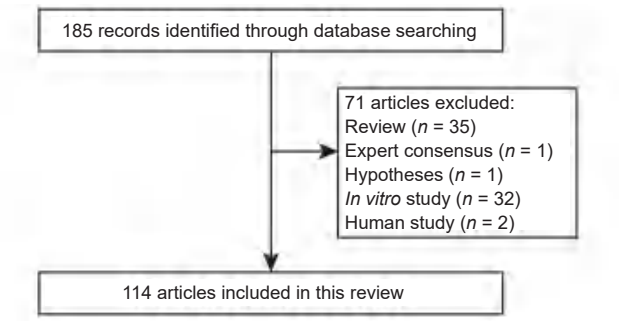

Figure 1. Flowchart of the literature search process.

Periodontal Defect Model

Mouse

Mice are widely utilised in biomedical research as models for periodontal disease due to their low-cost and convenience. However, the narrow oral cavity of mice poses challenges when performing intricate surgical procedures. This limitation makes it difficult to achieve uniform defect sizes across experimental groups. Hence, the murine periodontal defect was not surgically created, but rather induced through periodontitis. The unique advantage of mice is that stem cells originating from human can be transplanted and evaluated for their regenerative ability in immunodeficient mice. Additionally, mice can be gene-manipulated, enabling researchers to study the impact of specific genes on periodontal regeneration.

In 2018, Dr. Fareeha Batool[14] reported a chronic defect model in mice to test a membrane biomaterial for periodontal regeneration. The model involved inducing periodontitis in the palatal sites of the maxillary 1st molar through the placement of *Porphyromonas gingivlais*-infected silk ligatures. After 40 days, intrabony defects were formed, and the safety and efficacy of the biomaterial were evaluated through a palatal flap technique. The biomaterial was placed over the bony defect, and periodontal regeneration was assessed at 7th and 15th days post-treatment. The assessment included measurements of epithelial attachment, connect tissue attachment and alveolar bone level, analysed through histological imaging, to demonstrate tissue regeneration. This study provides valuable insights into the use of mice as models for evaluating regenerative therapies in periodontal disease.

Rat

The rat has become a commonly used animal model in the study of periodontal disease due to its histological similarities with the human periodontal region. Through inoculating periodontal pathogens, or fixing ligatures around the teeth, rats can develop periodontitis.[15] However, it is important to consider certain differences between rats and humans, including rapid wear of the occlusion surfaces and continuous eruption of molars leading to physiological remodelling of periodontal tissues.[7] Moreover, it is noteworthy that in rats, tooth drift occurs in a distal direction, whereas in humans, it occurs mesially. Cellular cementum progressively deposits to adapt to these physiological changes. This has a significant impact on the interpretation of data from periodontal defect models in rats. In addition, rats are less likely to form intrabony defects in periodontitis model due to the narrow interdental spaces, usually presented with horizontal bone loss.[16]

1 State Key Laboratory of Oral & Maxillofacial Reconstruction and Regeneration, Key Laboratory of Oral Biomedicine Ministry of Education, Hubei Key Laboratory of Stomatology, School & Hospital of Stomatology, Wuhan University, Wuhan, Hubei Province, China; 2 Department of Orthodontics, School and Hospital of Stomatology, Wuhan University, Wuhan, Hubei Province, China; 3 Department of Oral and Maxillofacial Surgery, Peking University Shenzhen Hospital, Shenzhen Peking University-The Hong Kong University of Science and Technology Medical Centre, Guangdong Province, China

Periodontal fenestration defect models have been widely used in research. Male Wistar or Sprague-Dawley rats are the most commonly used strains in these studies, where a critical-size defect is created on the radicular surfaces of the mandibular molars. The surgical procedure involves making an incision along the inferior border of the mandible, dissecting the underlying masseter muscle and periosteum, creating a 2 mm wide, 5 mm long, and 1.2 mm deep defect, and removing residual periodontal ligament and cementum.[17] To assess the regenerative ability of membrane biomaterials, these membranes were placed into the defects. Three weeks after the regenerative surgery, tissue samples are collected for the histological examination. This model can be modified by injecting rats with lipopolysaccharide to establish an inflammatory condition,[18] conducting the procedure in athymic rats to study the cell sheets obtained from human donors,[12, 19] or combining it with ovariectomy to study the effect of biomaterials in patients with both periodontal disease and osteoporosis.[20, 21]

Intrabony defect models can also be created in rats by surgically creating bilateral intrabony defects mesial to the first maxillary molar. After a crestal incision is made on the alveolar ridge, the alveolar bone mesial to the first maxillary molar is eliminated using a piezoelectric device under saline irrigation.[13, 22-29] The final dimensions of the defect are 2 mm by 2 mm by 1.7 mm in length, width, and depth, respectively. The defects are then treated with biomaterials according to the study design, and after 12 weeks, animals are euthanised and dissected for histomorphometry analysis.[24]

Rabbit

Periodontitis can be induced in rabbits.[30] Unlike rats and mice, the use of ligatures alone is not sufficient to induce periodontal disease in rabbits, making them a valuable model for evaluating the specific impact of human origin periodontal pathogens. Surgical creation of periodontal fenestration defects is also possible in rabbits due to their larger size, however, the continuous eruption of their teeth results in shifting of the defects towards the occlusal surface. By 12 weeks post-surgery, the defects have been replaced, rather than regenerated, with no signs of the surgical procedure present. As a result, the rabbit fenestration defect model is not appropriate for the study of periodontal regeneration.[31] Instead, traditional models such as rabbit femoral and calvarial defects have proven to provide valuable insights into bone healing and regeneration, although they may not accurately reflect the specific situation of periodontitis.[32, 33]

Dog

The size and anatomy of teeth and periodontal tissues in dogs are comparable to those observed in humans. Due to the accumulation of dental plaque and calculus, dogs frequently develop periodontitis in adulthood. In dogs, periodontitis is characterised by gingival recession, the formation of deep periodontal pockets, and bone defects.[34] Furcation regions are more commonly affected than interdental spaces, and in the late stages of periodontitis, the first and second premolars are most frequently lost. While naturally occurring periodontal defects in dogs are not uniform in terms of extent and location, this model may not be ideal for studying periodontal regeneration.[35] In contrast, surgical models are often used to test regeneration procedures. Defects can be rapidly and symmetrically created in dogs, allowing for the assessment of scaffolds, membranes, and growth factors for tissue regeneration. However, it is important to note that the care regulations for dogs are more complex and costly compared to rodents. Dogs require weekly periodontal prophylaxis, including ultrasonic cleaning and the use of 0.12% chlorhexidine mouthwash.

Intrabony defects

The production of 1-, 2-, and 3-wall intrabony defects in beagles has been experimentally validated. Among these, 3-wall intrabony defects exhibit greater potential for periodontal tissue regeneration. On the other hand, 1-wall defects are more susceptible to the formation of junctional epithelium, owing to the challenge of preserving the interstitial space between the tooth surface and the soft tissue flap.[36] The outcomes of tissue regeneration in the 2-wall intrabony defect model are influenced by the location of tissue sections, with sections closer to the lateral wall demonstrating greater regeneration than those further away.[35] Thus, the 2-wall intrabony defect may not be the optimal choice for evaluating candidate biomaterials.

The procedures for creating periodontal intrabony defects in dogs have been described in previous literatures.[37-42] Following the extraction of one or two premolars and a 2-month healing period, incisions are made and mucoperiosteal flaps are elevated from the underlying jaw bone. The alveolar bone, cementum, and periodontal ligament of the root surface are then surgically removed to create the intrabony defects, as illustrated in **Figure 2**. In each dog, up to four defects can be produced. An 8-week healing interval post-regenerative surgery is sufficient for the evaluation of periodontal regeneration in tissue samples.[43] Five histometric parameters, as illustrated in **Figure 3**, are useful for the assessment of tissue regeneration in histological images:[36, 44]

1. Defect height: distance from the alveolar crest to the base of the reference notch.
2. Junctional epithelium: distance from the cemento-enamel junction to the apical extension of the junctional epithelium on the root surface.
3. Connective tissue attachment: distance from the apical extension of the junctional epithelium to the coronal extension of newly formed cementum.
4. Cementum regeneration: distance from the base of the reference notch to the coronal extension of newly formed cementum on the root surface.
5. Bone regeneration: distance from the base of the reference notch to the coronal extension of newly formed bone along the root surface.

Supra-alveolar defects

The supra-alveolar defect model in dogs involves the horizontal removal of alveolar bone surrounding teeth. Specifically, critical-size 5-mm supra-alveolar periodontal defects are created around the mandibular premolars after

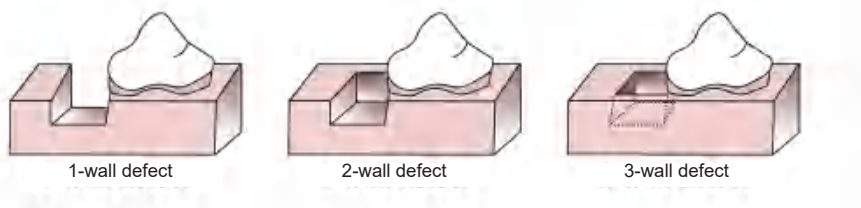

Figure 2. Schematic diagram depicting the surgically created 1-, 2-, and 3-wall intrabony defects.

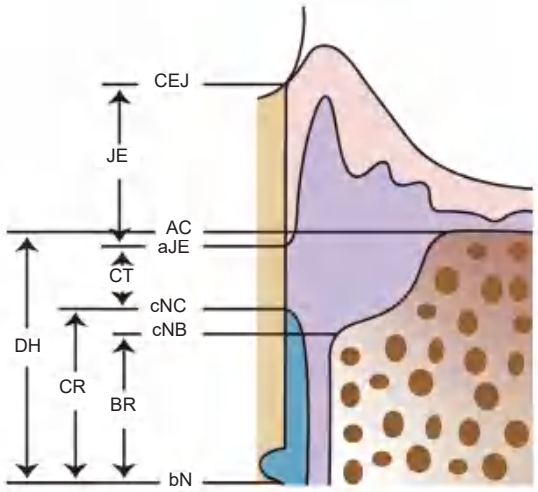

Figure 3. Schematic drawing representing measurement points for histometric parameters. AC: alveolar crest; aJE: apical extension of the junctional epithelium; bN: base of the reference notch; BR: bone regeneration; CEJ: cemento-enamel junction; cNB: coronal extension of newly formed bone; cNC: coronal extension of newly formed cementum; CR: cementum regeneration; CT: connective tissue attachment; DH: defect height; JE: junctional epithelial attachment.

elevating the mucoperiosteal flaps.[9, 45] The alveolar bone is removed using chisels and a hand-piece with fissure burs under water irrigation. The residual periodontal ligament and cementum are then removed from the roots through planing. As previously described, sterile ligatures are placed around the affected teeth for 8 weeks to induce an inflammatory condition in the periodontium.[46] This model is used to evaluate the efficacy of new biomaterials in promoting periodontal regeneration.

Furcation defects

The anatomy of the upper and lower premolars and the progression of periodontitis at these sites in beagles and mongrel dogs are highly similar to those in humans, making these dogs a valuable model for studying periodontal disease. The furcation defect model is often established around premolars, with class II furcation defects exhibiting the greatest potential for periodontal tissue regeneration. Conversely, class III furcation defects are associated with limited and unpredictable tissue regeneration due to the limited number of periodontal stem cells present on the defect surface.[47]

To create a class II furcation defect, the buccal mucoperiosteal flap is elevated to reveal the underlying alveolar bone, which is then removed to expose the buccal roots. The root surfaces are scaled to remove debris, periodontal ligament, and cementum. The defects are created with dimensions of 5 mm apicocoronally, 5 mm mesiodistally, and 3 mm buccolingually.[48, 49] The surgical procedure for creating class III furcation defects is similar to that of class II, with the difference being that more alveolar bone is removed to form a buccolingually penetrating defect on the root.[50] After surgery, the defects are filled with polyether impression material for 21 days to induce an inflammatory response and suppress natural bone repair.

Recession-type defects

The creation of artificial recession-type defects on the buccal surfaces of maxillary canine teeth in dogs is a common surgical procedure. This model is established by making a semicircular incision and two vertical incisions on the buccal gingiva, followed by elevation of a full-thickness flap. The resultant buccal dehiscence defects are 6 mm apicocoronally and 5 mm mesiodistally in dimensions.[51]

Interproximal periodontal defects

The Interproximal periodontal defect model was first established on dogs by Jung et al.[44] in 2011 as a means of studying a common clinical defect. The surgical procedure involves the creation of a vertical incision in the area surrounding the maxillary second premolar and the elevation of a full-thickness flap to expose the underlying alveolar bone between the second and third premolars. The removal of the alveolar bone and remaining periodontal tissues from the root surfaces results in the creation of a 5 mm vertically oriented and 3 mm horizontally oriented pocket defect that lacks any supporting bony walls.

Miniature pig

The miniature pig has proven to be a valuable animal model in periodontal research due to its similarity to humans in periodontal anatomy and the presence of naturally occurring periodontitis.[52] Additionally, its economical advantage over larger animals has further facilitated its use in various experiments. The induction of experimental periodontitis through ligature placement and pathogen inoculation in these animals takes approximately 4 weeks to develop, with the resultant destruction not fully restored even upon removal of the ligatures. Over the years, miniature pigs have been utilised to assess the regenerative capabilities of various biomaterials and technologies, with dehiscence-type defects created in the buccal aspect of mandibular premolars as one such example.[10]

Nonhuman primate

The anatomy of teeth and periodontium in nonhuman primates, particularly Macaca fascicularis, closely resembles that of humans and is characterised by the presence of dental plaque, calculus, and periodontal disease in adulthood.[53] Thus, nonhuman primates are considered an excellent animal model for evaluating regenerative procedures in periodontics. However, the use of nonhuman primates in experimental research raises ethical concerns and is expensive due to the requirement of specialised facilities and high costs associated with procurement and maintenance. As a result, the evaluation of new biomaterials in lower order phylogenetic species is recommended prior to testing in nonhuman primates.

There are three methods for inducing periodontal defects in nonhuman primates: the acute defect model, the chronic defect model, and the acute/chronic defect model. In the acute defect model, standard surgical procedures are followed, and spontaneous regeneration occurs in approximately 50–70% of cases, making it difficult to determine the extent to which regenerative outcomes are due to the biomaterials.[54] In the chronic defect model, orthodontic elastics are placed around the teeth, leading to accelerated plaque accumulation, inflammation, and destruction of periodontal tissues over a 3–6-month period. This defect model is usually conducted in single root teeth. If the interproximal space between teeth is large, then an angular intrabony defect will be obtained. If the interproximal space is narrow or there is an elastic on the adjacent tooth, suppra-alveolar defects will be achieved.[55] This model accurately mimics human periodontitis, but is time consuming and costly. The acute/chronic defect model combines surgical removal of periodontal tissues with the placement of ligatures or alginate to induce chronic inflammation and inhibit spontaneous regeneration.[11, 56-58]

Other Defect Models

The mandibular angle defect model is a widely accepted method for evaluating the efficacy of biomaterials in promoting bone regeneration. This model involves creating round, through-and-through osseous defects measuring 5 mm in diameter on both sides of the mandible in Sprague-Dawley rats. It has been successfully used to assess the performance of membrane materials and the results are obtained by fixing the membranes to the bone defects for 6 weeks and monitoring the progress of bone regeneration.[59]

The calvarial defect model, on the other hand, is a powerful tool for evaluating the potential of biomaterials for craniofacial skeleton regeneration. This model is also useful for periodontal research, as the physiological remodelling of calvaria is similar to that of the human mandibular bone.[60] This model is conducted in rats and rabbits and involves exposing the calvarial bone through a sagittal incision, elevating a full-thickness flap, and creating a round transosseous defect of 8 mm in diameter in the centre of the calvarium of rats[61-67] or four bony defects of the same diameter in rabbits.[33, 68, 69] The created bony defect is regarded as a critical-sized defect, which will not heal spontaneously during the lifetime of the animal.[70] To evaluate the effectiveness of the biomaterials, histological evaluation and micro-computed tomography analysis are performed at 2- and 8-week intervals post-surgery. Micro-computed tomography analysis calculates parameters such as total augmented volume, new bone volume, bone volume fraction, and bone mineral density, which are analysed for statistical significance.[63] Meanwhile, histomorphometric analysis measures the areas and percentages of new bone, residual material, and defect closure, providing additional information on the efficacy of the biomaterials.[64, 71]

Heterotopic Regeneration Model

The heterotopic subcutaneous transplantation model has been extensively utilised in stem cell-based regeneration research. This well-established model eliminates the influence of microenvironmental factors on tissue regeneration, making it a valuable tool for evaluating stem cell-based therapies. The model involves the assembly of stem cell sheets, specifically human periodontal ligament stem cells, onto scaffold materials[72-75] or bone grafts,[76-80] which are then subcutaneously implanted into the dorsal area of athymic mice or rats. Some studies have incorporated dentin slices and bone substitutes to simulate the periodontal space.[72-74] Following a 6–8-week healing interval, tissue samples are collected and analysed for the formation of cementum, bone, and the periodontal ligament. These evaluations provide insight into the efficacy of stem cell-based therapies for periodontal tissue regeneration.

Conclusions & Perspectives

The testing of periodontal regenerative procedures in animal models is crucial prior to the initiation of clinical trials. By creating periodontal defects similar to those found in human patients, the safety and effectiveness of new biomaterials and treatments can be assessed. The availability of sufficient tissue samples allows for a comprehensive evaluation of the quality and extent of regenerated periodontal support tissues.

Rats, due to their ease of feeding and maintenance, have become the standard animal model for testing new biomaterials. However, it is important to note that the physiology of the periodontium in rats differs from that of humans. Dogs and non-human primates, on the other hand, provide the closest approximation of human periodontium, making them ideal models for the verification of regenerative procedures. However, the use of these animals must be justified by ethical considerations and the limitations imposed by the number of animals used must be carefully considered during the

experimental design. In conclusion, a stepwise approach is recommended for evaluating new biomaterials, starting with testing in small animals, followed by validation in dogs and non-human primates.

While acute defects, namely surgically created defects, are predominantly employed in these included articles due to their ability to ensure uniform defect sizes across experimental groups and reduce the duration of animal experiments, it's worth highlighting that acute defects do not faithfully replicate the pathological characteristics of defects caused by periodontitis. Discrepancies exist in the pathophysiological conditions and the processes involved in tissue healing and regeneration between acute defects and those caused by periodontitis. Consequently, experimental findings derived from acute defect models may not offer precise predictability for clinical applications. As such, we advocate the adoption of chronic periodontal defect models, with the aim of furnishing more clinically pertinent insights for translational purposes. Furthermore, periodontitis-induced tooth mobility and tooth loss represent the most immediate factors impacting patients' quality of life. In the context of these animal experiments, there is limited documentation regarding the effectiveness of biomaterials in ameliorating tooth mobility. We contend that these functional outcome assessments should be incorporated into the evaluation of animal models, in addition to histomorphological measurements, to provide a more comprehensive understanding.

This review provides a comprehensive overview of frequently employed animal models as reported in the literature (**Table 1**). The rationale for the selection of these animal models in the

Table 1. Animal models for periodontal regeneration

Animal species	Characteristic	Type of model	Site of defect	Size of defect	Longest period for evaluation
Mouse	Low-cost; Immunodeficient mice and gene-manipulated mice are available; Regenerative procedures are difficult to conduct due to the narrow oral cavity.	Chronic periodontal defect model			15 days
		Heterotopic transplantation model			8 weeks
Rat	Well established as a model for periodontitis; Physiological remodelling of periodontal tissues due to continuous eruption of molars; More likely to form horizontal bone loss due to the narrow interdental spaces.	Acute periodontal defect model	Fenestration defect	$2 \times 5 \times 1.2$ mm^3	3 weeks
		Other defect models	Intrabony defect	$2 \times 2 \times 1.7$ mm^3	12 weeks
			Mandibular angle defect	5 mm in diameter	6 weeks
			Calvarial defect	8 mm in diameter	12 months
Rabbit	Periodontitis can be induced; Fenestration defects may be replaced rather than regenerated due to the continuous eruption of their teeth.	Other defect models	Calvarial defect	8 mm in diameter	8 weeks
Dog	Size and anatomy of periodontal tissues are comparable to humans; Naturally developed periodontitis; The daily care and postoperative maintenance are more complex than rodents.	Acute periodontal defect model	Intrabony defect	$5 \times 5 \times 5$ mm^3 or $5 \times 5 \times 4$ mm^3 or $4 \times 4 \times 4$ mm^3	24 weeks
			Supra-alveolar defect	5 mm	8 weeks
			Furcation defect	$5 \times 5 \times 3$ mm^3	120 days
			Recession-type defect	6×5 mm^2	8 weeks
			Interproximal periodontal defect	5×3 mm^2	8 weeks
Miniature pig	Similarities to humans in periodontal anatomy and the presence of naturally occurring periodontitis.	Acute periodontal defect model	Recession-type defect	5×4 mm^2	3 months
Nonhuman primate	The anatomy of teeth and periodontium in nonhuman primates closely resembles that of humans; An excellent animal model for evaluating regenerative procedures; Ethical concerns, requirements of specialised facilities and high costs.	Acute/chronic periodontal defect model		7–9 × 2–3 mm^2 or $3 \times 4 \times 5$ mm^3	5 months

cited articles was typically based on references to previously published research. Consequently, our review lacks an in-depth exploration of the physiological characteristics of periodontal tissue in various animal species but centres on the methodologies for establishing these models. Additionally, it should be noted that only a limited number of the included articles provided data on the incidence of adverse events following regenerative procedures, thus this critical aspect is not addressed in our review.

Author contributions

QS and HH conceptualised and designed the review; QS drafted the manuscript; YL, PL and HH checked and revised the manuscript. All authors reviewed and approved the final version of the manuscript.

Financial support

None.

Acknowledgement

None.

Conflicts of interest statement

The authors declare no conflict of interest.

1. Nazir, M. A. Prevalence of periodontal disease, its association with systemic diseases and prevention. *Int J Health Sci (Qassim).* **2017**, *11*, 72-80.
2. Kwon, T.; Lamster, I. B.; Levin, L. Current concepts in the management of periodontitis. *Int Dent J.* **2021**, *71*, 462-476.
3. Melcher, A. H. On the repair potential of periodontal tissues. *J Periodontol.* **1976**, *47*, 256-260.
4. Nyman, S.; Gottlow, J.; Karring, T.; Lindhe, J. The regenerative potential of the periodontal ligament. An experimental study in the monkey. *J Clin Periodontol.* **1982**, *9*, 257-265.
5. Villar, C. C.; Cochran, D. L. Regeneration of periodontal tissues: guided tissue regeneration. *Dent Clin North Am.* **2010**, *54*, 73-92.
6. Xu, X. Y.; Li, X.; Wang, J.; He, X. T.; Sun, H. H.; Chen, F. M. Concise review: periodontal tissue regeneration using stem cells: strategies and translational considerations. *Stem Cells Transl Med.* **2019**, *8*, 392-403.
7. Struillou, X.; Boutigny, H.; Soueidan, A.; Layrolle, P. Experimental animal models in periodontology: a review. *Open Dent J.* **2010**, *4*, 37-47.
8. Kantarci, A.; Hasturk, H.; Van Dyke, T. E. Animal models for periodontal regeneration and peri-implant responses. *Periodontol 2000.* **2015**, *68*, 66-82.
9. Nuñez, J.; Sanchez, N.; Vignoletti, F.; Sanz-Martin, I.; Caffesse, R.; Santamaria, S.; Garcia-Sanz, J. A.; Sanz, M. Cell therapy with allogenic canine periodontal ligament-derived cells in periodontal regeneration of critical size defects. *J Clin Periodontol.* **2018**, *45*, 453-461.
10. França-Grohmann, I. L.; Sangiorgio, J. P. M.; Bueno, M. R.; Casarin, R. C. V.; Silvério Ruiz, K. G.; Nociti, F. H., Jr.; Casati, M. Z.; Sallum, E. A. Treatment of dehiscence-type defects with collagen matrix and/or enamel matrix derivative: histomorphometric study in minipigs. *J Periodontol.* **2020**, *91*, 967-974.
11. Jimbo, R.; Singer, J.; Tovar, N.; Marin, C.; Neiva, R.; Bonfante, E. A.; Janal, M. N.; Contamin, H.; Coelho, P. G. Regeneration of the cementum and periodontal ligament using local BDNF delivery in class II furcation defects. *J Biomed Mater Res B Appl Biomater.* **2018**, *106*, 1611-1617.
12. Farag, A.; Hashimi, S. M.; Vaquette, C.; Bartold, P. M.; Hutmacher, D. W.; Ivanovski, S. The effect of decellularized tissue engineered constructs on periodontal regeneration. *J Clin Periodontol.* **2018**, *45*, 586-596.
13. Hasani-Sadrabadi, M. M.; Sarrion, P.; Nakatsuka, N.; Young, T. D.; Taghdiri, N.; Ansari, S.; Aghaloo, T.; Li, S.; Khademhosseini, A.; Weiss, P. S.; Moshaverinia, A. Hierarchically patterned polydopamine-containing membranes for periodontal tissue engineering. *ACS Nano.* **2019**, *13*, 3830-3838.
14. Batool, F.; Morand, D. N.; Thomas, L.; Bugueno, I. M.; Aragon, J.; Irusta, S.; Keller, L.; Benkirane-Jessel, N.; Tenenbaum, H.; Huck, O. Synthesis of a novel electrospun polycaprolactone scaffold functionalized with ibuprofen for periodontal regeneration: an in vitro and in vivo study. *Materials (Basel).* **2018**, *11*, 580.
15. Khuda, F.; Baharin, B.; Anuar, N. N. M.; Satimin, B. S. F.; Nasruddin, N. S. Effective Modalities of Periodontitis Induction in Rat Model. *J Vet Dent.* **2023**, 8987564231178459.
16. Heijl, L.; Wennström, J.; Lindhe, J.; Socransky, S. S. Periodontal disease in gnotobiotic rats. *J Periodontal Res.* **1980**, *15*, 405-419.
17. Ni, C.; Zhou, J.; Kong, N.; Bian, T.; Zhang, Y.; Huang, X.; Xiao, Y.; Yang, W.; Yan, F. Gold nanoparticles modulate the crosstalk between macrophages and periodontal ligament cells for periodontitis treatment. *Biomaterials.* **2019**, *206*, 115-132.
18. Shang, F.; Liu, S.; Ming, L.; Tian, R.; Jin, F.; Ding, Y.; Zhang, Y.; Zhang, H.; Deng, Z.; Jin, Y. Human umbilical cord MSCs as new cell sources for promoting periodontal regeneration in inflammatory periodontal defect. *Theranostics.* **2017**, *7*, 4370-4382.
19. Dan, H.; Vaquette, C.; Fisher, A. G.; Hamlet, S. M.; Xiao, Y.; Hutmacher, D. W.; Ivanovski, S. The influence of cellular source on periodontal regeneration using calcium phosphate coated polycaprolactone scaffold supported cell sheets. *Biomaterials.* **2014**, *35*, 113-122.
20. Zhang, Y.; Wei, L.; Wu, C.; Miron, R. J. Periodontal regeneration using strontium-loaded mesoporous bioactive glass scaffolds in osteoporotic rats. *PLoS One.* **2014**, *9*, e104527.
21. Zheng, B.; Jiang, J.; Chen, Y.; Lin, M.; Du, Z.; Xiao, Y.; Luo, K.; Yan, F. Leptin overexpression in bone marrow stromal cells promotes periodontal regeneration in a rat model of osteoporosis. *J Periodontol.* **2017**, *88*, 808-818.
22. Oortgiesen, D. A.; Walboomers, X. F.; Bronckers, A. L.; Meijer, G. J.; Jansen, J. A. Periodontal regeneration using an injectable bone cement combined with BMP-2 or FGF-2. *J Tissue Eng Regen Med.* **2014**, *8*, 202-209.
23. Cai, X.; Yang, F.; Yan, X.; Yang, W.; Yu, N.; Oortgiesen, D. A.; Wang, Y.; Jansen, J. A.; Walboomers, X. F. Influence of bone marrow-derived mesenchymal stem cells pre-implantation differentiation approach on periodontal regeneration in vivo. *J Clin Periodontol.* **2015**, *42*, 380-389.
24. El-Sayed, B.; Davies, R. P. W.; El-Zehery, R. R.; Ibrahim, F. M.; Grawish, M. E.; Kirkham, J.; El-Gendy, R. An in-vivo intraoral defect model for assessing the use of p(11)-4 self-assembling peptide in periodontal regeneration. *Front Bioeng Biotechnol.* **2020**, *8*, 559494.
25. Liu, X.; He, X.; Jin, D.; Wu, S.; Wang, H.; Yin, M.; Aldalbahi, A.; El-Newehy, M.; Mo, X.; Wu, J. A biodegradable multifunctional nanofibrous membrane for periodontal tissue regeneration. *Acta Biomater.* **2020**, *108*, 207-222.
26. Xu, X.; Zhou, Y.; Zheng, K.; Li, X.; Li, L.; Xu, Y. 3D polycaprolactone/gelatin-oriented electrospun scaffolds promote periodontal regeneration. *ACS Appl Mater Interfaces.* **2022**, *14*, 46145-46160.

27. Nemcovsky, C. E.; Zahavi, S.; Moses, O.; Kebudi, E.; Artzi, Z.; Beny, L.; Weinreb, M. Effect of enamel matrix protein derivative on healing of surgical supra-infrabony periodontal defects in the rat molar: a histomorphometric study. *J Periodontol.* **2006**, *77*, 996-1002.
28. Oortgiesen, D. A.; Meijer, G. J.; Bronckers, A. L.; Walboomers, X. F.; Jansen, J. A. Regeneration of the periodontium using enamel matrix derivative in combination with an injectable bone cement. *Clin Oral Investig.* **2013**, *17*, 411-421.
29. Babo, P. S.; Cai, X.; Plachokova, A. S.; Reis, R. L.; Jansen, J.; Gomes, M. E.; Walboomers, X. F. Evaluation of a platelet lysate bilayered system for periodontal regeneration in a rat intrabony three-wall periodontal defect. *J Tissue Eng Regen Med.* **2018**, *12*, e1277-e1288.
30. Hasturk, H.; Jones, V. L.; Andry, C.; Kantarci, A. 1-Tetradecanol complex reduces progression of Porphyromonas gingivalis-induced experimental periodontitis in rabbits. *J Periodontol.* **2007**, *78*, 924-932.
31. Oortgiesen, D. A.; Meijer, G. J.; Bronckers, A. L.; Walboomers, X. F.; Jansen, J. A. Fenestration defects in the rabbit jaw: an inadequate model for studying periodontal regeneration. *Tissue Eng Part C Methods.* **2010**, *16*, 133-140.
32. Schmitt, J. M.; Buck, D. C.; Joh, S. P.; Lynch, S. E.; Hollinger, J. O. Comparison of porous bone mineral and biologically active glass in critical-sized defects. *J Periodontol.* **1997**, *68*, 1043-1053.
33. Lee, J. Y.; Park, J. Y.; Hong, I. P.; Jeon, S. H.; Cha, J. K.; Paik, J. W.; Choi, S. H. 3D-printed barrier membrane using mixture of polycaprolactone and beta-tricalcium phosphate for regeneration of rabbit calvarial defects. *Materials (Basel).* **2021**, *14*, 3280.
34. Hamp, S. E.; Hamp, M.; Olsson, S. E.; Lindberg, R.; Schauman, P. Radiography of spontaneous periodontitis in dogs. *J Periodontal Res.* **1997**, *32*, 589-597.
35. Haney, J. M.; Zimmerman, G. J.; Wikesjö, U. M. Periodontal repair in dogs: evaluation of the natural disease model. *J Clin Periodontol.* **1995**, *22*, 208-213.
36. Kim, C. S.; Choi, S. H.; Chai, J. K.; Cho, K. S.; Moon, I. S.; Wikesjö, U. M.; Kim, C. K. Periodontal repair in surgically created intrabony defects in dogs: influence of the number of bone walls on healing response. *J Periodontol.* **2004**, *75*, 229-235.
37. Matsuse, K.; Hashimoto, Y.; Kakinoki, S.; Yamaoka, T.; Morita, S. Periodontal regeneration induced by porous alpha-tricalcium phosphate with immobilized basic fibroblast growth factor in a canine model of 2-wall periodontal defects. *Med Mol Morphol.* **2018**, *51*, 48-56.
38. Imber, J. C.; Bosshardt, D. D.; Stähli, A.; Saulacic, N.; Deschner, J.; Sculean, A. Pre-clinical evaluation of the effect of a volume-stable collagen matrix on periodontal regeneration in two-wall intrabony defects. *J Clin Periodontol.* **2021**, *48*, 560-569.
39. Shirakata, Y.; Taniyama, K.; Yoshimoto, T.; Miyamoto, M.; Takeuchi, N.; Matsuyama, T.; Noguchi, K. Regenerative effect of basic fibroblast growth factor on periodontal healing in two-wall intrabony defects in dogs. *J Clin Periodontol.* **2010**, *37*, 374-381.
40. Iwata, T.; Yamato, M.; Tsuchioka, H.; Takagi, R.; Mukobata, S.; Washio, K.; Okano, T.; Ishikawa, I. Periodontal regeneration with multi-layered periodontal ligament-derived cell sheets in a canine model. *Biomaterials.* **2009**, *30*, 2716-2723.
41. Kim, C. K.; Kim, H. Y.; Chai, J. K.; Cho, K. S.; Moon, I. S.; Choi, S. H.; Sottosanti, J. S.; Wikesjö, U. M. Effect of a calcium sulfate implant with calcium sulfate barrier on periodontal healing in 3-wall intrabony defects in dogs. *J Periodontol.* **1998**, *69*, 982-988.
42. Shirakata, Y.; Setoguchi, F.; Sena, K.; Nakamura, T.; Imafuji, T.; Shinohara, Y.; Iwata, M.; Noguchi, K. Comparison of periodontal wound healing/regeneration by recombinant human fibroblast growth factor-2 combined with β-tricalcium phosphate, carbonate apatite, or deproteinized bovine bone mineral in a canine one-wall intra-bony defect model. *J Clin Periodontol.* **2022**, *49*, 599-608.
43. Choi, S. H.; Kim, C. K.; Cho, K. S.; Huh, J. S.; Sorensen, R. G.; Wozney, J. M.; Wikesjö, U. M. Effect of recombinant human bone morphogenetic protein-2/absorbable collagen sponge (rhBMP-2/ACS) on healing in 3-wall intrabony defects in dogs. *J Periodontol.* **2002**, *73*, 63-72.
44. Jung, U. W.; Chang, Y. Y.; Um, Y. J.; Kim, C. S.; Cho, K. S.; Choi, S. H. Interproximal periodontal defect model in dogs: a pilot study. *Oral Dis.* **2011**, *17*, 26-32.
45. Wikesjö, U. M.; Selvig, K. A.; Zimmerman, G.; Nilvéus, R. Periodontal repair in dogs: healing in experimentally created chronic periodontal defects. *J Periodontol.* **1991**, *62*, 258-263.
46. Wei, L.; Teng, F.; Deng, L.; Liu, G.; Luan, M.; Jiang, J.; Liu, Z.; Liu, Y. Periodontal regeneration using bone morphogenetic protein 2 incorporated biomimetic calcium phosphate in conjunction with barrier membrane: a pre-clinical study in dogs. *J Clin Periodontol.* **2019**, *46*, 1254-1263.
47. Garrett, S.; Gantes, B.; Zimmerman, G.; Egelberg, J. Treatment of mandibular class III periodontal furcation defects. Coronally positioned flaps with and without expanded polytetrafluoroethylene membranes. *J Periodontol.* **1994**, *65*, 592-597.
48. Carlo Reis, E. C.; Borges, A. P.; Araújo, M. V.; Mendes, V. C.; Guan, L.; Davies, J. E. Periodontal regeneration using a bilayered PLGA/calcium phosphate construct. *Biomaterials.* **2011**, *32*, 9244-9253.
49. Chantarawaratit, P.; Sangvanich, P.; Banlunara, W.; Soontornvipart, K.; Thunyakitpisal, P. Acemannan sponges stimulate alveolar bone, cementum and periodontal ligament regeneration in a canine class II furcation defect model. *J Periodontal Res.* **2014**, *49*, 164-178.
50. Suaid, F. A.; Macedo, G. O.; Novaes, A. B.; Borges, G. J.; Souza, S. L.; Taba, M.; Palioto, D. B.; Grisi, M. F. The bone formation capabilities of the anorganic bone matrix-synthetic cell-binding peptide 15 grafts in an animal periodontal model: a histologic and histomorphometric study in dogs. *J Periodontol.* **2010**, *81*, 594-603.
51. Shujaa Addin, A.; Akizuki, T.; Hoshi, S.; Matsuura, T.; Ikawa, T.; Fukuba, S.; Matsui, M.; Tabata, Y.; Izumi, Y. Biodegradable gelatin/beta-tricalcium phosphate sponges incorporating recombinant human fibroblast growth factor-2 for treatment of recession-type defects: A split-mouth study in dogs. *J Periodontal Res.* **2017**, *52*, 863-871.
52. Wang, S.; Liu, Y.; Fang, D.; Shi, S. The miniature pig: a useful large animal model for dental and orofacial research. *Oral Dis.* **2007**, *13*, 530-537.
53. Schou, S.; Holmstrup, P.; Kornman, K. S. Non-human primates used in studies of periodontal disease pathogenesis: a review of the literature. *J Periodontol.* **1993**, *64*, 497-508.
54. Caton, J.; Mota, L.; Gandini, L.; Laskaris, B. Non-human primate models for testing the efficacy and safety of periodontal regeneration procedures. *J Periodontol.* **1994**, *65*, 1143-1150.
55. Caton, J. G.; Kowalski, C. J. Primate model for testing periodontal treatment procedures: II. Production of contralaterally similar lesions. *J Periodontol.* **1976**, *47*, 506-510.
56. Yamashita, M.; Lazarov, M.; Jones, A. A.; Mealey, B. L.; Mellonig, J. T.; Cochran, D. L. Periodontal regeneration using an anabolic peptide with two carriers in baboons. *J Periodontol.* **2010**, *81*, 727-736.
57. Emerton, K. B.; Drapeau, S. J.; Prasad, H.; Rohrer, M.; Roffe, P.; Hopper, K.; Schoolfield, J.; Jones, A.; Cochran, D. L. Regeneration of

periodontal tissues in non-human primates with rhGDF-5 and beta-tricalcium phosphate. *J Dent Res.* **2011**, *90*, 1416-1421.

58. Wang, B.; Mastrogiacomo, S.; Yang, F.; Shao, J.; Ong, M. M. A.; Chanchareonsook, N.; Jansen, J. A.; Walboomers, X. F.; Yu, N. Application of BMP-bone cement and FGF-gel on periodontal tissue regeneration in nonhuman primates. *Tissue Eng Part C Methods.* **2019**, *25*, 748-756.
59. Zellin, G.; Gritli-Linde, A.; Linde, A. Healing of mandibular defects with different biodegradable and non-biodegradable membranes: an experimental study in rats. *Biomaterials.* **1995**, *16*, 601-609.
60. Spicer, P. P.; Kretlow, J. D.; Young, S.; Jansen, J. A.; Kasper, F. K.; Mikos, A. G. Evaluation of bone regeneration using the rat critical size calvarial defect. *Nat Protoc.* **2012**, *7*, 1918-1929.
61. Polimeni, G.; Koo, K. T.; Pringle, G. A.; Agelan, A.; Safadi, F. F.; Wikesjö, U. M. Histopathological observations of a polylactic acid-based device intended for guided bone/tissue regeneration. *Clin Implant Dent Relat Res.* **2008**, *10*, 99-105.
62. An, Y. Z.; Heo, Y. K.; Lee, J. S.; Jung, U. W.; Choi, S. H. Dehydrothermally cross-linked collagen membrane with a bone graft improves bone regeneration in a rat calvarial defect model. *Materials (Basel).* **2017**, *10*, 927.
63. Jang, J. W.; Lee, J. S.; Jung, U. W.; Kim, C. S.; Cho, K. S. In vivo evaluation of commercially available gel-type polyethylene glycol membrane for carrier of recombinant human bone morphogenetic protein-2. *J Oral Maxillofac Surg.* **2017**, *75*, 297.e1-297.e13.
64. Jung, U. W.; Choi, S. Y.; Pang, E. K.; Kim, C. S.; Choi, S. H.; Cho, K. S. The effect of varying the particle size of beta tricalcium phosphate carrier of recombinant human bone morphogenetic protein-4 on bone formation in rat calvarial defects. *J Periodontol.* **2006**, *77*, 765-772.
65. Jung, U. W.; Song, K. Y.; Kim, C. S.; Lee, Y. K.; Cho, K. S.; Kim, C. K.; Choi, S. H. Effects of a chitosan membrane coated with polylactic and polyglycolic acid on bone regeneration in a rat calvarial defect. *Biomed Mater.* **2007**, *2*, S101-105.
66. Pang, E. K.; Im, S. U.; Kim, C. S.; Choi, S. H.; Chai, J. K.; Kim, C. K.; Han, S. B.; Cho, K. S. Effect of recombinant human bone morphogenetic protein-4 dose on bone formation in a rat calvarial defect model. *J Periodontol.* **2004**, *75*, 1364-1370.
67. Park, J. C.; So, S. S.; Jung, I. H.; Yun, J. H.; Choi, S. H.; Cho, K. S.; Kim, C. S. Induction of bone formation by Escherichia coli-expressed recombinant human bone morphogenetic protein-2 using block-type macroporous biphasic calcium phosphate in orthotopic and ectopic rat models. *J Periodontal Res.* **2011**, *46*, 682-690.
68. You, H.; Lee, E. U.; Kim, Y. K.; Kim, B. C.; Park, J. Y.; Lim, H. C.; Lee, J. S.; Noh, I.; Jung, U. W.; Choi, S. H. Biocompatibility and resorption pattern of newly developed hyaluronic acid hydrogel reinforced three-layer poly (lactide-co-glycolide) membrane: histologic observation in rabbit calvarial defect model. *Biomater Res.* **2014**, *18*, 12.
69. Pae, H. C.; Kang, J. H.; Cha, J. K.; Lee, J. S.; Paik, J. W.; Jung, U. W.; Choi, S. H. Bone regeneration using three-dimensional hexahedron channel structured BCP block in rabbit calvarial defects. *J Biomed Mater Res B Appl Biomater.* **2019**, *107*, 2254-2262.
70. Teng, S. H.; Lee, E. J.; Wang, P.; Shin, D. S.; Kim, H. E. Three-layered membranes of collagen/hydroxyapatite and chitosan for guided bone regeneration. *J Biomed Mater Res B Appl Biomater.* **2008**, *87*, 132-138.
71. Choi, J. Y.; Jung, U. W.; Kim, C. S.; Eom, T. K.; Kang, E. J.; Cho, K. S.; Kim, C. K.; Choi, S. H. The effects of newly formed synthetic peptide on bone regeneration in rat calvarial defects. *J Periodontal Implant Sci.* **2010**, *40*, 11-18.
72. Zhao, B.; Chen, J.; Zhao, L.; Deng, J.; Li, Q. A simvastatin-releasing scaffold with periodontal ligament stem cell sheets for periodontal regeneration. *J Appl Biomater Funct Mater.* **2020**, *18*, 2280800019900094.
73. Wang, Z. S.; Feng, Z. H.; Wu, G. F.; Bai, S. Z.; Dong, Y.; Chen, F. M.; Zhao, Y. M. The use of platelet-rich fibrin combined with periodontal ligament and jaw bone mesenchymal stem cell sheets for periodontal tissue engineering. *Sci Rep.* **2016**, *6*, 28126.
74. Liao, Y.; Li, H.; Shu, R.; Chen, H.; Zhao, L.; Song, Z.; Zhou, W. Mesoporous hydroxyapatite/chitosan loaded with recombinant-human amelogenin could enhance antibacterial effect and promote periodontal regeneration. *Front Cell Infect Microbiol.* **2020**, *10*, 180.
75. Varoni, E. M.; Vijayakumar, S.; Canciani, E.; Cochis, A.; De Nardo, L.; Lodi, G.; Rimondini, L.; Cerruti, M. Chitosan-based trilayer scaffold for multitissue periodontal regeneration. *J Dent Res.* **2018**, *97*, 303-311.
76. Yang, H.; Gao, L. N.; An, Y.; Hu, C. H.; Jin, F.; Zhou, J.; Jin, Y.; Chen, F. M. Comparison of mesenchymal stem cells derived from gingival tissue and periodontal ligament in different incubation conditions. *Biomaterials.* **2013**, *34*, 7033-7047.
77. Gao, L. N.; An, Y.; Lei, M.; Li, B.; Yang, H.; Lu, H.; Chen, F. M.; Jin, Y. The effect of the coumarin-like derivative osthole on the osteogenic properties of human periodontal ligament and jaw bone marrow mesenchymal stem cell sheets. *Biomaterials.* **2013**, *34*, 9937-9951.
78. Park, J. C.; Oh, S. Y.; Lee, J. S.; Park, S. Y.; Choi, E. Y.; Cho, K. S.; Kim, C. S. In vivo bone formation by human alveolar-bone-derived mesenchymal stem cells obtained during implant osteotomy using biphasic calcium phosphate ceramics or Bio-Oss as carriers. *J Biomed Mater Res B Appl Biomater.* **2016**, *104*, 515-524.
79. Gao, H.; Li, B.; Zhao, L.; Jin, Y. Influence of nanotopography on periodontal ligament stem cell functions and cell sheet based periodontal regeneration. *Int J Nanomedicine.* **2015**, *10*, 4009-4027.
80. Kim, Y. T.; Park, J. C.; Choi, S. H.; Cho, K. S.; Im, G. I.; Kim, B. S.; Kim, C. S. The dynamic healing profile of human periodontal ligament stem cells: histological and immunohistochemical analysis using an ectopic transplantation model. *J Periodontal Res.* **2012**, *47*, 514-524.

Received: February 25, 2023
Revised: June 2, 2023
Accepted: September 4, 2023
Available online: September 28, 2023

Biomaterials Translational

Fabrication, microstructure and properties of advanced ceramic-reinforced composites for dental implants: a review

Mugilan Thanigachalam[*,#], *Aezhisai Vallavi Muthusamy Subramanian*[#]

Key Words:
ceramic composites; flexural strength; fracture toughness; implant materials; sintering; Vickers hardness

From the Contents

ABSTRACT

The growing field of dental implant research and development has emerged to rectify the problems associated with human dental health issues. Bio-ceramics are widely used in the medical field, particularly in dental implants, ortho implants, and medical and surgical tools. Various materials have been used in those applications to overcome the limitations and problems associated with their performance and its impact on dental implants. In this article we review and describe the fabrication methods employed for ceramic composites, the microstructure analyses used to identify significant effects on fracture behaviour, and various methods of enhancing mechanical properties. Further, the collective data show that the sintering technique improves the density, hardness, fracture toughness, and flexural strength of alumina- and zirconia-based composites compared with other methods. Future research aspects and suggestions are discussed systematically.

Department of Mechanical Engineering, Government College of Technology, Coimbatore, Tamil Nadu, India

***Corresponding author:**
Mugilan Thanigachalam, mugilangct@gmail.com.

#Author equally.

http://doi.org/10.12336/biomatertransl.2023.03.004

How to cite this article:
Thanigachalam, M.; Subramanian, A. V. M. Fabrication, microstructure and properties of advanced ceramic-reinforced composites for dental implants: a review. *Biomater Transl.* **2023**, *4*(3), 151-165.

Introduction

Global biomedical research in industry has been driven rapidly due to several limitations of dental implants such as short service life, failure rate, and poor functional performance. Ceramics are non-metallic materials which are made from combinations of metal and non-metallic components. The essential properties of ceramics are high strength, high hardness, excellent oxidation resistance, low thermal conductivity, and good corrosion resistance. However most ceramics are monolithic, and some special engineering functions cannot be achieved effectively due to their brittle nature.[1] Consequently the principal intention for working on ceramic matrix composites (CMCs) is to enhance the current options and increase the many applications in the fields of engineering and medicine.[2, 3] These can be achieved by making modifications to existing composites and then implementing new combinations of matrix and reinforcements.[4]

CMCs have excellent thermal shock resistance, are resistant to wear, possess excellent creep behaviour, and exhibit improved fracture toughness.[5] The causes of crack initiation and development such as material fatigue, over loading, and residual stress in ceramic material have been investigated and many strengthening mechanisms have been employed to avoid the formation of cracks in the tip area using filler materials. High temperatures and thermal shocks are a necessary aspect of various engineering applications. Typically, tubes are present in the flow heat exchangers, cutting tool inserts, and gasoline turbines in automobile industries, particularly aerospace appliances[6] "*The common reinforcements especially applied in dental ceramic composites are titanium carbide (TiC), carbon nanotubes (CNTs), titanium nitride (TiN), boron nitride (BN), carbon nanofibres (CNF), carbon powder, graphene, etc.*" Spark plasma sintering (SPS) and hot pressing are the most common and effective techniques for preparing composites with higher temperature ranges. In addition to the temperature limitation, other limitations of this method include degradation. Another limitation of CMCs is that they cannot be used to make complex shapes. During sintering of CMCs

also leads to thermal stress introduction. So conventional or non-conventional machining (NCM) processes are used when additional manufacturing steps are necessary. The known methods used for machining ceramics and their composite are drilling and grinding. Both these methods are tricky for complex shape and require more time to machine and machining the complex shape.[7] "*Ultrasonic machining (USM), abrasive jet machining (AJM), abrasive water jet machining (AWJM), laser machining, and electric discharged machining (EDM) are the important cost reduction techniques in modern CNC*".[8] NCM processes can reduce the cost and gear up by eliminating or reducing the need for secondary machining. Also, most NCM techniques reduce the requirement for costly cutting tools, because material is removed by erosion and abrasion with a simple primary source. Mechanical abrasion, melting or evaporation, chemical dissolution, and electrochemical dissolution are developed machining techniques involved in ceramic machining involving material removal.[9] For the last three decades, remarkable development has been achieved in all kinds of ceramic frames for use in dental restoration applications. Combined aesthetic veneering porcelains for all restorations are made up of ceramics that consist of fluorapatite, leucite, or aluminium oxide as the crystalline phase and glass with high strength ceramic cores, particularly zirconium-oxide or aluminium-oxide, and lithium-disilicate. All ceramics consist of a more significant proportion of different crystalline phases, which differs from metal-ceramics.[10] This is the main reason underlying the improvements in mechanical properties of all ceramics, but more substantial opacity can develop, which is not advisable for ceramics used in dental applications. Various factors can increase or decrease the transparency of a material: the grain size, microstructure particle orientation, phase refractive index, and refractive index.[11] Consequently there is a greater potential to develop a clear, transparent appearance using alumina and zirconia ceramics, and the recent alumina series provides greater translucency by using special materials suitable for clinical use.

Dental ceramic materials are classified based on the ceramic system, transparency, microstructure, fabrication temperature, material composition, and usage. Based on these parameters, the glass-to-crystalline ratio, the geometry of crystalline structure and size, and the mismatch between the crystal thermal expansion, Young's modulus, and phase changes, significantly influence the properties and performance of dental ceramic materials.[12, 13]

To improve the properties of a material, it is generally essential to increase its density through stage adjustment (using another stage of grain development); dynamic sintering (adding another substance to build mass vehicle); responsive sintering (the utilization of added importance to forestall loss of stoichiometry), and through liquid-stage sintering. Consequently, the sintering cycle can be improved by sintering added substances, which are utilized to balance out the desired glasslike structures, or added to the liquid stage to aid increased densification. In this sense, a glassy phase can be a sintering added substance. Indeed, the sintering cycle in the presence of a glass (liquid stage sintering) can happen at a lower temperature in the examination of dry sintering (sintering measure without a polished stage). Liquid stage sintering includes the arrangement of fluids because of the various softening temperatures of the segments. The liquid phase accounts for 1% to 20% of the volume. Control of the microstructure of ceramic materials is critical because it permits acquisition of data to measure the exhibition of these materials in help. In dental ceramic production, surface cracks can be distinguished through the fluorescent penetrant liquid technique or identified through acoustic emission, optically or interferometrically. Also, the various essential factors involved in the design consideration of dental implants are biocompatibility, bio- and osseointegration, biomechanics, corrosion resistance, material compositions, and mechanical properties. Recent dental implant materials, shapes, and factors considered in the design of dental implants are shown in **Figure 1**. In this article we attempt to review the research dealing with the various fabrication methods, microstructural analysis, and some essential mechanical properties of ceramic composites used in dental implants.

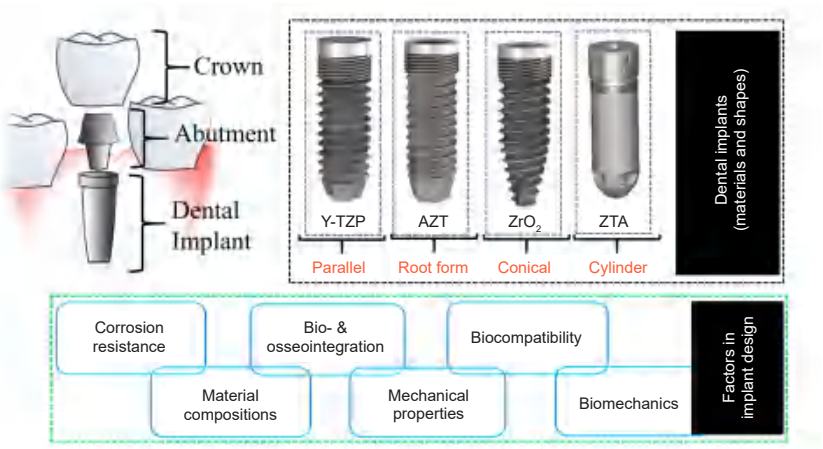

Figure 1. Materials and factors considered in the design of dental implants. AZT: alumina-toughened zirconia; Y-TZP: yttria-stabilised tetragonal zirconia polycrystalline; ZrO_2: zirconium dioxide; ZTA: zirconia-toughened alumina.

Materials and Fabrication Methods Involved in Ceramic Composites

The most significant ceramic materials used in dental implant application are listed. Zirconia (ZrO_2) is known for its excellent biocompatibility and strength, and thus is widely used for dental implant abutments and frameworks. Alumina (Al_2O_3) ceramics offer high strength and wear resistance, making them suitable for dental implant applications. Hydroxyapatite (HA) is a bioactive ceramic often used as a coating on dental implant surfaces to enhance osseointegration. Bioactive glass can bond with bone tissue and can be used in dental implant coatings. Tricalcium phosphate (TCP) ceramics have properties of biocompatibility and resorbability, making them useful in dental implant applications. Yttria-stabilised zirconia (YSZ) ceramics combine the properties of zirconia with enhanced stability due to yttria stabilization. Lithium disilicate is used for making dental crowns and bridges due to its aesthetic properties and strength.[14] Glass-ceramics such as leucite-reinforced ceramics are used in dental restorations due to their natural appearance and strength. Silicon nitride (Si_3N_4) ceramics, although less common, have been investigated for dental implant applications due to their mechanical properties. Calcium phosphate ceramics offer bioactivity and can support bone regeneration around dental implants. The choice of a ceramic material depends on various factors including its mechanical properties, biocompatibility, aesthetics, and intended application within the dental implant system.[15]

Titanium and its alloys are widely used for dental implants due to their biocompatibility. Researchers are focusing on developing innovative surface modifications to enhance osseointegration and promote better bone integration. Zirconia continues to be popular for dental implants, and researchers are exploring ways to improve its properties further by blending it with other materials or modifying its microstructure. Biodegradable materials, such as magnesium alloys or polymers, are being studied for use as temporary implants and as scaffolds for tissue regeneration. These materials gradually degrade over time as new tissue forms.

Researchers are working on developing advanced ceramic composites with improved mechanical properties and aesthetics for dental implant applications. One such material is polyether ether ketone (PEEK)-based biopolymers reinforced by different ceramic particulates like titanium dioxide (TiO_2) and silicon dioxide (SiO_2) with surface modifications. These modifications provide improved mechanical strength and excellent osteointegration.[16-19]

Various coatings and bioactive agents are being investigated to improve implant-bone bonding, prevent infections, and stimulate tissue regeneration. Smart implants are implants embedded with sensors or electronics that are being explored for real-time monitoring of implant conditions, healing progress, and potential issues.

Based on functional requirements, properties, and application, CMCs can be fabricated by various techniques as described by multiple investigators: dry pressing (uniaxial compacting), hot isostatic compacting, and cold isostatic compacting of powder ceramics.[20] The major important factors adopted for the fabrication of CMCs are operating temperature, type of reinforcement used, and the size and shape of the composites required, which depend on an application basis.[21] The liquid phase process contains the sol-gel and polymer infiltration pyrolysis processing methods. Slip casting and powder metallurgy are the most applicable techniques for preparing composites in the solid phase.[22] Because these techniques can be applied to ceramic materials with high melting points, like titanium, zirconium, tungsten, molybdenum, and tantalum, they can also achieve homogenous particle distribution. These can reduce the need for subsequent machining and increase the powder-to-product percentage. The gas-phase process includes reaction bonding, chemical vapour deposition, and chemical vapour infiltration. Reinforcement and matrix phase produce the chemical reaction that has controlled conditions in the gas phase reaction, and these techniques include reaction bonding and chemical vapour infiltration processes. Much recent research undertaken to reduce the processing temperature and time are using powder metallurgical techniques to achieve a high rate of densification, to produce a near net shape, and the energy requirement is less for growth and nucleation properties.[23]

Compressive strength and bulk density are the critical properties of CMCs in many applications. Still, there is some disadvantage to achieving these properties in reaction bonding of materials in the sintering technique with a temperature range from 1450°C to 1700°C. The single microwave cavity method has also been used to obtain a pore-free and homogeneous composite instead of sintering.[24] The weight percentage and fracture toughness of the preceramic polymer polycarbosilane can be increased. The material's porosity can be decreased in preceramic polymer reaction bonding by fabricating porous ceramics. The phase-wise fabrication techniques are classified into liquid, solid, and gas phases, illustrated in **Figure 2**. The commercially-available dental zirconia systems are tabulated in **Table 1**.[25] Most implant manufacturing companies moved towards one-piece type implants with various shapes such as conical, cylindrical, and root forms because the process and material properties are critically important in two-piece type implants.

Melting infiltration in the reaction bonding technique has been adopted for manufacture of silicon carbide (SiC)/CNT composite. The proper distribution of reinforcement is assured by using this technique, leading to better electrical conductivity properties. By increasing the graphite content, the open porosity of the multi-bonded porous ceramic increases, and it can be decreased by improving the temperature and forming pressure of the sintering process. Due to gaseous oxidation within products, open pores are formed.[26] There is an improvement in flexure strength with increased multiplication which is achieved by increasing sintering temperature. The reaction bonding process protects the oxidation of SiC with formation of a gel intermediary.[27] At the various temperatures of the ferro molybdenum (FeMO) alloy fabrication process, the effect of alloying confers excellent physical properties on CMCs.[28] A similar study has been carried out in the reaction-bonded technique of silicon nitride by adding lithium oxide

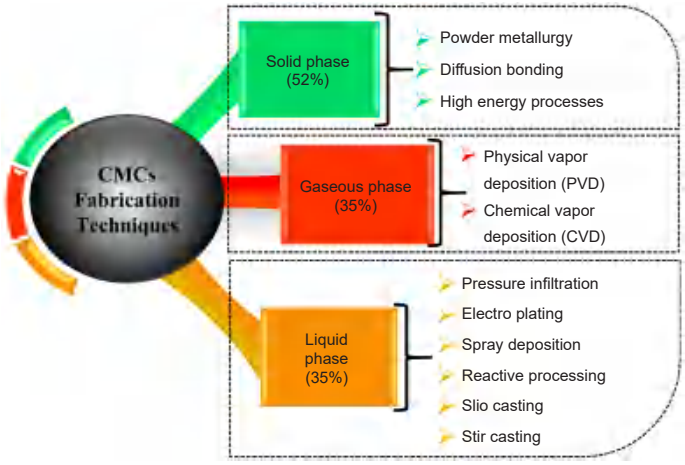

Figure 2. Ceramic matrix composite fabrication processes. CMCs: ceramic matrix composites; CVD: chemical vapour deposition; PVD: physical vapour deposition.

Table 1. Implant manufacturers and zirconia implant materials

Implant material	Product name	Manufacturer
Alumina-toughened zirconia	ZERAMEX (P)lus	Dental point AG, Spreitenbach, Switzerland
	FairWhite™	Fair implant, Schleswig-Holstein, Germany
	SDS – Swiss Dental Solutions 1.0 DT	SDS Swiss Dental Solutions AG, Kreuzlingen, Switzerland
Yttria-stabilised tetragonal zirconia polycrystalline	CeraRoot	CeraRoot S.L, Barcelona, Spain
	Ceralog	Camlog System, Basel, Switzerland
	SDS 2.2	SDS AG, Kreuzlingen, Switzerland
	ICX-White	MKI GmbH &Co.KG, Stuttgart, Germany
	REPLICATE™ System	Natural Dental Implant AG, Berlin, Germany
Zirconia oxide	Konus K3Pro ZirKon Implant system	Argon Medical Productions, Plano, TX, USA
	Easy Kon	General Implants, Wurmlingen, Germany
	Whitesky	Bredent medical, Senden, Germany
	CeraRoot	
	(S)andard ZV3	ZV3-ZirconVison GmbH, Munchen, Germany
	Ceramic implant	VITA Zahnfabrik, Wurttemberg, Germany

(LiO_2) and Si powder. The findings revealed that regardless of Al impurity, when there is a decrease in thermal conductivity, the purity of Si powder increases, and the presence of LiO_2 also increases. The effective way of determining the bending strength of a composite is the four-point bending method. In this case, Si powder with course level addition gives the best result of about 700 MPa and 11 MPa·$m^{1/2}$ of fracture toughness.[29] The addition of various sizes of particles to reaction-bonded boron carbide gives excellent fracture toughness. The presence of pores in reaction-bonded boron carbide ceramic due to residual silicon affects the fracture toughness property. Where there is a decrease in volume fraction, the hardness of reaction-bonded boron carbide composite increases because it contains larger-sized particles.[30] Decreasing the residual silicon quality of the composite will give a reduction in porosity. By using nano-sized zirconia powder, the SiC growth will increase, a method of composite fabrication which provides an increased level of flexural strength and fracture toughness.

The densification rate has been increased and the temperature reduced for vanadium pentoxide (V_2O_5). The effect of reinforcement by addition of SiC particles in the nitration gives higher density and achieves the required mechanical properties and explicit microstructure.[31] The addition of 10% SiC particles in the sintered specimen gives better mechanical properties of reaction bonding between the silicon nitrate composites.[32] The two-step freeze casting technique has been implemented for composite fabrication to reduce thermal reaction in SiC ceramics, creating an overall shape with improved strength. Material deposition is associated with various ceramics, metal alloys, and semiconductors with coatings of thin and thick layers. An advanced method such as thermal plasma chemical vapour deposition produces enhanced results compared to the other conventional deposition methods. The SiC/Si_3N_4 alpha-beta phase is formed in a controlled manner. The gas turbine materials, semiconducting material, various coatings of ceramic composites, and fibre-reinforced composites are

broad application areas in the CVD and sintering processes. During the sintering process, the particles of ceramic and reinforcement are compressed after the compacting process using a gravity die setup at high temperatures. A grain boundary will develop due to the hot pressing between the particles. This forms a connective structure with the help of neck formation. A higher compressive force and the effect of higher temperature maintain the neck growth formation which tends to develop and become densified. During this process, the porosity of the ceramic composite is reduced due to the temperature effect on the densification process. Pore-free ceramic structures are being fabricated using sintering techniques.[33] Densification through neck formation in the sintering process is shown in **Figure 3**.

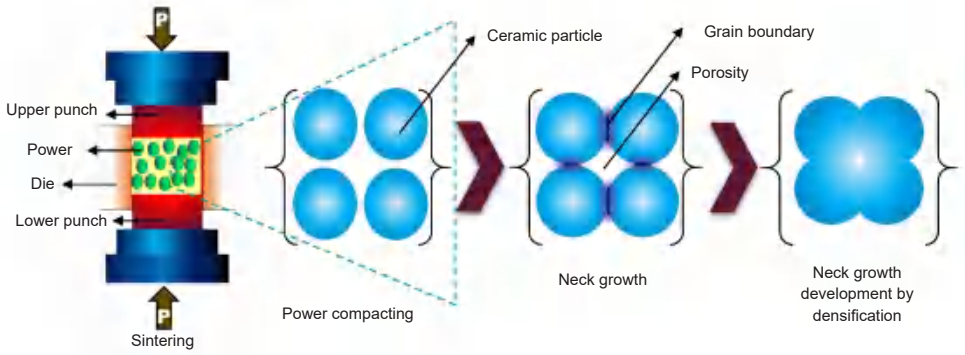

Figure 3. Grain growth development by densification.

The fabrication techniques suitable for ceramic composites based on their crystalline structure are listed in **Figure 4**. **Figure 5** shows the sintering techniques divided into general categories. Based on pressure-assisted and pressureless sintering, the state, the type of phases that the material possesses, and stress level, whether it is considered high-stress or low-stress level, have been classified. In phase-oriented classification, processes are further divided into liquid and solid phases under which sub-entities are included for consideration while selecting the type of sintering. The actual sintering process stages are classified into three stages, starting from the heating stage, holding for a particular temperature and finally cooling the specimen. During the first stage of this process, the temperature of the tip increases because of the gradual increment of tip displacement. Sintering is a critical step in the fabrication process of dental implants, particularly when using ceramics or metal alloys. Sintering involves heating the implant components at elevated temperatures but below their melting points. This process leads to the fusion of particles, resulting in densification, increased mechanical strength, and improved material properties. Sintering is essential to achieve the required structural integrity and biocompatibility of dental implant materials, ensuring that the implant materials are strong enough to withstand the mechanical forces exerted during chewing and other oral functions. Additionally, sintering helps achieve a biocompatible surface that allows for proper osseointegration, which is the fusion of the implant with the surrounding bone. The specifics of sintering, such as temperature, atmosphere, and time, depend on the material being used. Dental implant manufacturers carefully optimise these parameters to achieve the desired structural and biocompatible properties required for successful dental implantation. In **Table 2**, the grain size and sintering parameters and their relationship to relative density are shown.[34]

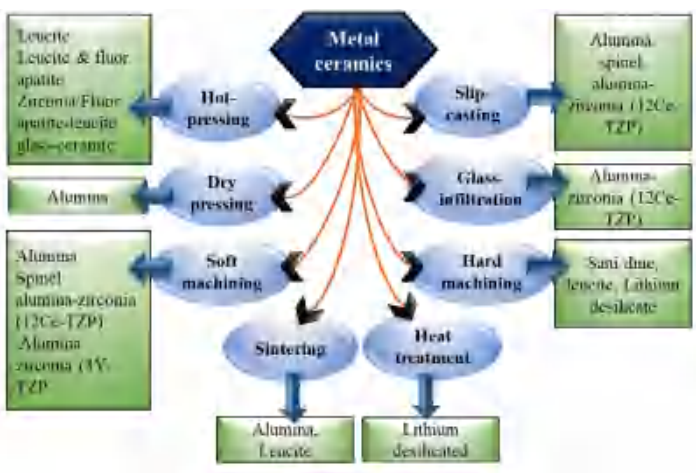

Figure 4. Appropriate fabrication techniques for various crystalline phases. 12Ce-TZP: 12 ceria stabilized tetragonal zirconia polycrystals; 3Y-TZP: 3 yttriastabilised tetragonal zirconia polycrystalline.

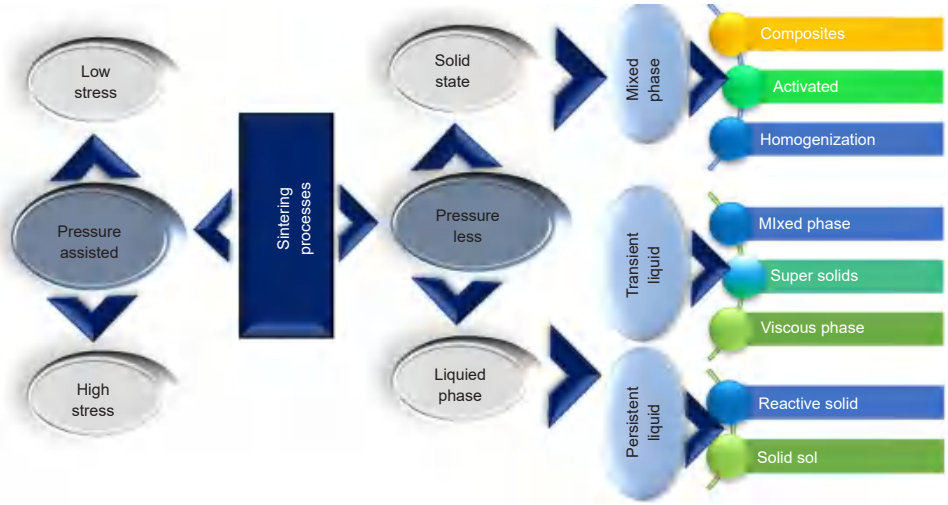

Figure 5. Classification of sintering processes.

Table 2. Summary of the sintering process of alumina-toughened zirconia

Sintering method	Sintering temperature (°C)	Holding time (minutes)	Relative density (%)	Grain size (nm)		Codes[a]
				Zirconia	Alumina	
Microwave sintering (MW)	1200	10	98.5	210±64	270±84	MW120010
	1200	30	99	240±67	300±100	MW120030
	1300	10	99.8	280±75	400±157	MW130010
	1300	30	99.8	280±70	380±146	MW130030
Conventional sintering (CS)	1400	120	98.3	240±41	350±98	CS1400120
	1500	120	99.2	330±56	450±100	CS1500120

Note: [a]First two letters indicate the method of sintering, next four digits indicates sintering temperature in degrees Celsius and last two digits indicate holding time in minutes.

Microstructure Studies

Microstructure analyses of dental ceramic composites were performed to improve understanding of the distribution of particles and elements, the presence of grains, phases, and molecular structure. This type of analysis is also used to study the surface characteristics of prepared composites. The surface characterisation includes surface morphology, fracture, fatigue, and grain growth analyses on the surface. The various microstructure examination techniques carried out were scanning electron microscopy (SEM), field emission SEM, and transmission electron microscopy using standard fracture and fatigue tested specimens for comparison. All dental ceramic composite such as ZrO_2, Al_2O_3, aluminium titanate (Al_2TiO_5), TiO_2, chromic oxide (Cr_2O_3), alumina-toughened zirconia (ATZ), and ZTA have various kinds of microstructural behaviour associated with their composition. Consequently, the addition of reinforcement gives an enhanced microstructure suitable for a particular application. The addition of reinforced particles such as oxides provides a densified microstructure. If the presence of Ni content increases within the structure, ceramic composites will give better densities than specimens with smaller pore sizes.[35] Usually, these gradual additions give the specimen a better relative density, due to the uniform spreading of nickel particles, which has been clearly shown in microstructure images. The authors suggested that the process of sintering is well suited to generating a material with a highly dense grain structure.[36]

The ceramic material tools used in the dental implant fabrication process consist of a very dense and refined microstructure of graphene particles with different contents. Improved strength has been achieved due to the mature dispersal of graphene particles in the CMCs, especially given the excellent distribution of various size grains. Less fractured surfaces were detected in SEM images of these graphite tool materials with tungsten carbide (WC).[37] An extensive fracture was determined at about 68% in the notch region of 2Ce-TZP compared to the monoclinic phase 3Y-TZP. Also, there was no micro-cracked zone in 3Y-TZP.[38] This analysis also revealed exciting facts about the various regions of the fracture surface specimens: from the initial notch crack to the final fracture. It was concluded that R curves help predict the stress intensity factor concerning crack length. The fracture surface of TSP with various crack regions is shown in **Figure 6**.

In the 3Y-TZP/Ta ceramic composite, the pressure applied perpendicular or parallel to the orientation of an SPS specimen was observed in SEM images. The Ta particles in the TZP composites give the material fracture toughness up to 15 $MPa{\cdot}m^{1/2}$. These microstructure images show the partial debonding of the Ta particles during plastic deformation due to

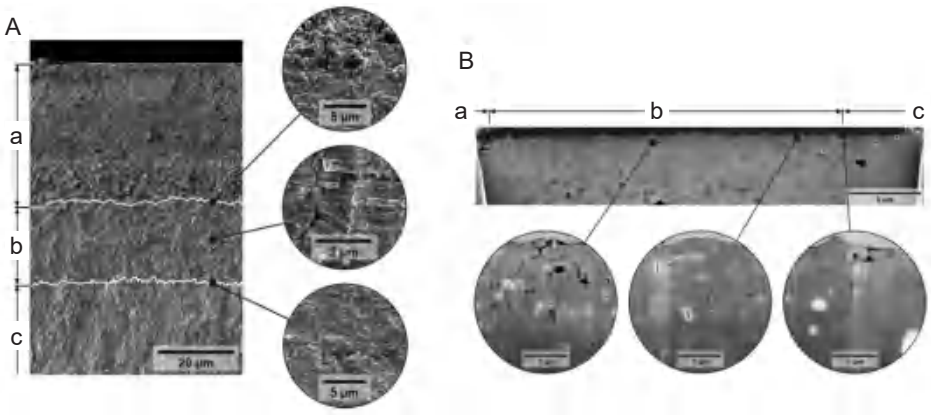

Figure 6. (A) Fracture surface, where three different regions are distinguished: notch (a), micro-cracked area (b), and regular fracture surface (c). (B) The cross-sectional view obtained by focused ion beam analysis of the fracture surface. Reprinted from Turon-Vinas and Anglada.[38] Copyright 2018 The Academy of Dental Materials.

the toughening process. The presence of Ta particles increases the crack growth resistance.[39] The focusing wavelength range of the SEM images also gives a better understanding of the various phenomena in the particle addition or any mechanism involved in improving the properties in this investigation. The 3LM type SEM with an EDX chemical microanalyzer was used for microstructural characterisation to identify the presence of phases. Crack propagation will occur because of the flake-shaped particles used in the SPS process with the applied pressure with uniform dispersion and proper orientation. Pressure-less rapid sintering of Al_2O_3 and ZrO_2 with various range compositions reveals the dense structure of the particles in SEM images with a constant sintering temperature of 1550°C per 2-minute duration and heating rates of 5°C to 100°C per minute.[40] The restriction of the densification process in the dental ceramic comprises a ZrO_2-Al_2O_3 base, purely based on the effect of zirconia.

SEM graphs of ZrO_2 (partially stabilized zirconia, PSZ) composites give the proper distribution of the particles and greater electron density brightens the zirconium (Zr) presence region. The particles did not possess the particular effect of base-pinned grain boundaries of alumina. Calcium magnesium-based ceramics have granular crystal morphology that includes microfracture because of grain size and distribution. If grain size is below 10 µm, the grain will give better distribution of images. Hot presses ceramic composites have higher density compared to other fabrication technique composites, and the standard atomic ratios of Ca, Mg, and Al are comparatively lower and are tightly bonded during sintering.[41] Nitrogen absorption is an effective analytical method for calculating the primary size of particles.[42] This technique can achieve the best particle dispersion. Alumina carbon composite created by sintering at 1400°C produces highly porous ceramics. This porosity was measured by the water absorption method. The technique of field emission gun-scanning electron microstructure is used for this analysis. Fracture morphologies of porous Si_3N_4-Si_3N_4 with 30 µm scale and different deposition times in hours reveal that the fracture of the porous structure is high.[43] Fracture morphologies of porous Si_3N_4-Si_3N_4 with various deposition times at 30 µm magnification are shown in **Figure** 7. SEM images of the fracture surfaces of Zr-based composites are shown in **Figure 8**.

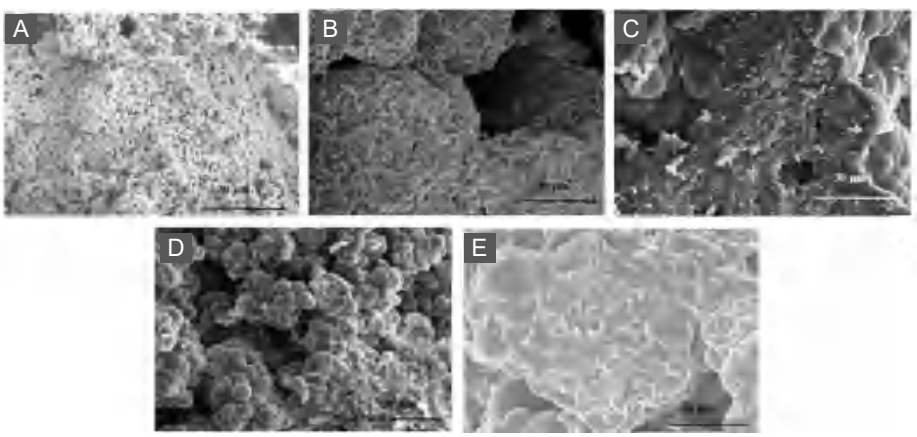

Figure 7. Fracture morphologies of porous Si_3N_4–Si_3N_4 composite ceramics as a function of deposition time: (A) 0, (B) 3, (C) 6, (D) 9, and (E) 12 hours. Scale bars: 30 µm. Si_3N_4: silicon nitride. Reprinted from Cheng et al.[43]

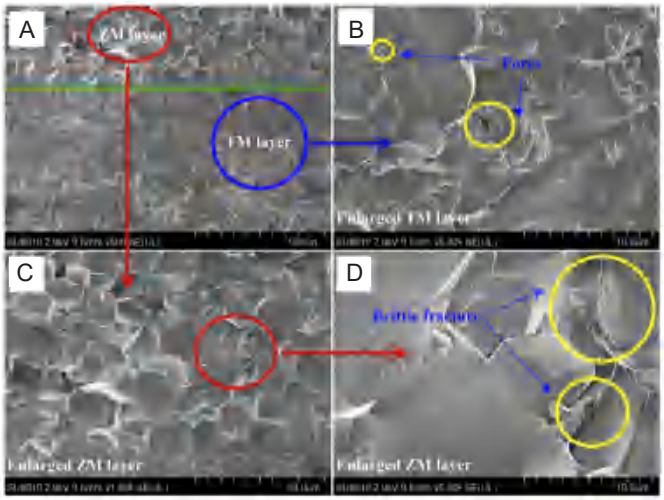

Figure 8. Scanning electron microscopic images of fracture surfaces. Scale bars: 100 μm (A), 10 μm (B, D), 50 μm (C). Reprinted from Liu et al.[4] Copyright 2019 Elsevier Ltd and Techna Group S.r.l.

Mechanical Properties

General properties of ceramic materials include high melting point, high hardness strength, physical properties those hinder the performance, high modulus of elasticity, good chemical resistance, and low malleability. Normally ceramic composite materials have been proven to be ionic materials so valence is warranted. These materials may be crystalline in structure or amorphous in nature. The substandard or enhanced mechanical properties lead to fracture and various deformations.[44] To overcome the brittle nature, ceramic material has been incorporated into the different reinforcement categories. Crack formation also developed as a result of the poor mechanical properties of ceramics. These limitations can be resolved by improving the mechanism of mechanical property improvement.

Vickers hardness

One factor influencing the hardness of the material is grain size; another is relative density. These two factors have been suggested to significantly affect the hardness of ATZ composites in most material research concerning a particular fabrication technique called sintering.[45] In the Vickers hardness test, monolithic ceramic composites like Al_2O_3-TiN increased 65% and achieved 24.6 GPa. A Vickers diamond pyramid-type indenter is a micro-indentation primarily suitable for prediction of dental bilayer structure hardness. Nanoindentation type hardness computation of standard specimens prepared on ceramics decreases slightly with Ni content addition. The effect of graphene on the hardness of ceramic tools has been improved up to 24.64 GPa.

Meanwhile, the hardness decreased due to the destruction of the microstructure. Hardness values of 1700 Vickers hardness number (VHN) have been achieved in many ATZ ceramic composites. The Zr toughened alumina ceramics reached 1120 VHN. The Y-TZP, tetragonal grain-based ceramics, have a 1200-VHN value. The hardness value of ceria-stabilised zirconia-based composites is 1160 VHN. The case of PSZ with alumina has a VHN of 16.31 MPa, a 30% improvement due to the addition of yttrium doping. The titanium (Ti) and graphene flakes significantly affect the ceramic hardness resulting in a 25% improvement. Due to the high sintering temperature of approximately 1650°C, under 35 MPa pressure, 20.1 GPa VHN has been achieved. The Vickers hardness value of Ti alumina-based ceramic has reached 37 GPa due to the increase of Ti particles in the alumina. Most sintering processes have been performed only after particle grain size reduction. The effect that increasing the sintering temperature on Vickers hardness has on variation in alumina ceramics with yttria-partially stabilised zirconia (Y-PSZ) is shown in **Figure 9**. Sintering temperature plays a vital role in obtaining the hardness and elastic modulus of alumina and zirconia-based ceramic composites.[46] The effect of sintering temperature on Vickers hardness and elastic modulus at the addition of zirconia is shown in **Figure 10**.

Decreasing the grain size results in a densified composite so that the hardness value increases because of the improvement in indentation resistance properties of the composites.[47] The ZrB_2–SiC–Ni with ball-milled sintering produces a composite hardness value of up to 20.2 GPa VHN. The two essential models of Vickers hardness prediction are the proportional specimen resistance[48] model using Meyer law and the Tabor model based on the theory of rigid material indentation related to yield stress. Using these kinds of empirical models, the indentation load-size effect of a material can be calculated. In Meyer law, it gives the relational existence between applied load (P) and indentation size (a), as shown in equation (1),

$$P = Ha^n \quad (1)$$

Where n is the Meyer index, and H is the constant. The specimen resistance can be calculated by using the following equation (2) according to Hays and Kendall,[46]

$$R = p_1 a \quad (2)$$

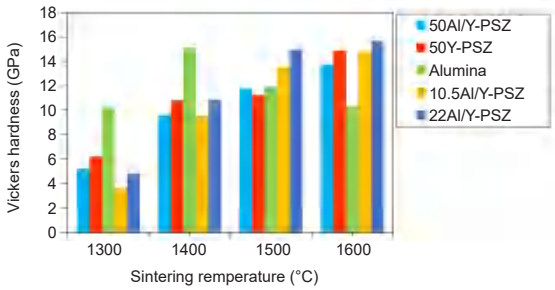

Figure 9. Effect of sintering temperature on Vickers hardness of alumina ceramics.

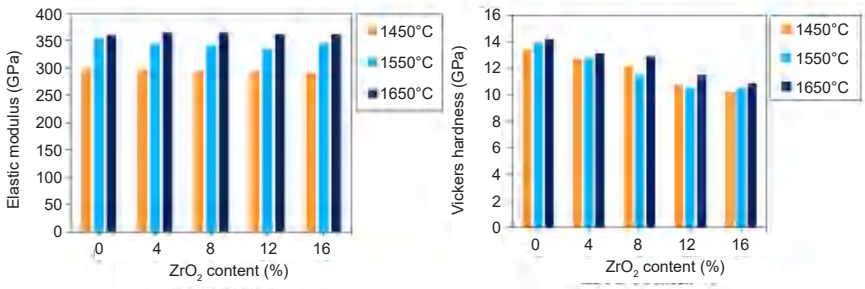

Figure 10. Effect of zirconia addition on elastic modulus and Vickers hardness at various sintering temperatures. ZrO_2: zirconium dioxide.

After that, effective indentation load and dimensions for indentation are relatively calculated by using the following equation (3),

$$P_{effective} = P - R = P - p_1 a = p_2 a^2 \quad (3)$$

Some modified versions of proportional specimen resistance models can be helpful for the determination of indentation hardness at the surface caused by induced residual stresses that occur while machining the specimen. Equation (4) depicts the relationship between the indentation parameters and indentation size,

$$P = \alpha + p_1 a + p_2 a^2 \quad (4)$$

Where α is the constant, and p_1 and p_2 are the proportional specimen resistance model parameters. These kinds of semi-empirical models are also beneficial to determining the nano level of the VHN of the ceramic materials, which have crystalline and monolithic forms, by using the following equation (5),

$$VHN = 1.8544 \frac{P_{effective}}{a^2} \quad (5)$$

The micro-Vickers hardness number of non-strain hardening specimens can be calculated by using the Tabor relation, which is related to yield stress yield σ_{yield} and load in equation (6),

$$VHN = 2.9\sigma_{yield} \quad (6)$$

Using this equation, the effects of indentation of the coated surface of ceramic composites can be calculated.

Fracture toughness

Fracture toughness is an important mechanical property for dental implant materials because this implies the reliability of products. The toughness value of most AZT ceramics is about 4.0 MPa·$m^{1/2}$ to 5.0 MPa·$m^{1/2}$ due to the high zirconia content. Zirconia-based ceramics have moderate fracture toughness values up to 4.5 MPa·$m^{1/2}$. Due to the tetragonal grains in the Y-TZP, fracture toughness increases from about 8.0 MPa·$m^{1/2}$ to 10.0 MPa·$m^{1/2}$, which is the highest value compared to the other types of dental ceramics.[49] The fracture toughness (FT) of microwave-sintered specimens were comparatively much better than those of other densified specimens prepared by conventional sintering. The peak value of fracture toughness achieved was 6.3 MPa·$m^{1/2}$ with microwave sintering (MS)130010 and the lowest was 4.9 MPa·$m^{1/2}$ with conventional sintering (CS) 1400120. Usually, the fracture toughness value increases with the increase of sintering temperature due to ceramic particle bonding. Also, higher sintering temperatures produce enhanced densities,[50, 51] so fracture toughness can reach exceptionally high values with SPS. In non-conventional techniques, the fracture toughness value improvement is highly possible with ZrB_2-SiC-Ni-ultra high temperature ceramics which achieve comparatively excellent toughness only because of their Ni content. The toughness value reaches a mean of 8.3 MPa·$m^{1/2}$ in ZrB_2-SiC ceramics. The reason for this improvement is that increasing the Ni content confers appropriate modifications in the macro defect reduction, due to the thermal expansion coefficient of the ceramic particles.[52] The toughness value is changed for the following reasons: one is the mis-match of the values, and another is the external load. So usually, low fracture toughness ceramics have limited practical applications.[53]

Figure 11 shows the fracture-toughening mechanism of zirconia composites. Initially, the zirconia particles in the monoclinic phase reach the crack initiation stage. Then, the phase-changing phenomenon transforms the monoclinic phase zirconia particles into tetragonal phase zirconia. Crack propagation is controlled by tetragonal phase zirconia due to its formation of covalent solid bonds after the phase-changing process. The technical analysis of surface cracks influenced by fracture toughness was carried out in alumina-based ceramics using crack length measurement. Based on that analysis, the crack initiation mechanism was formulated and then identically analysed and controlled in high-purity alumina ceramics. The standard empirical models used in direct crack length measurements are the Anstis and Palmqvist crack analysis models.[54] The effect of zirconia on fracture toughness at various grain sizes is shown in **Figure 12**. Initiating nucleation on a specific grain located on the surface triggers a process leading to the formation of micro-cracks and exerting stress on neighbouring regions within the transformed zone. This, in turn, results in extensive micro-cracking and a roughened surface. The orange pathway illustrates the penetration that occurs due to micro-cracking encircling the transformed grains. To overcome the limited resilience of alumina as well as the susceptibility of zirconia to ageing, the current trend involves the creation of alumina-zirconia composites. This approach offers the potential to harness the advantages of zirconia's toughness-enhancing mechanism while circumventing the significant drawback associated with its transformation when exposed to steam or bodily fluids. A recent review of literature about alumina-zirconia composites developed for biomedical applications reveals a range of compositions, spanning from zirconia-rich to alumina-rich, that have been subjected to testing.[55]

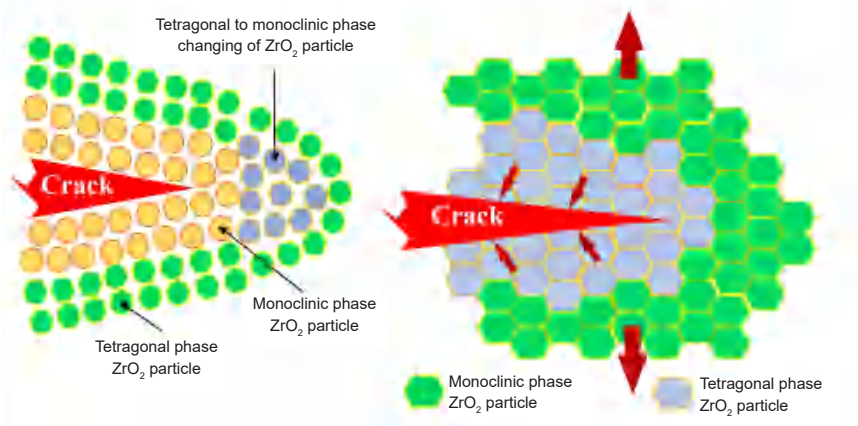

Figure 11. Toughening mechanism in zirconia against crack propagation. ZrO_2: zirconium dioxide.

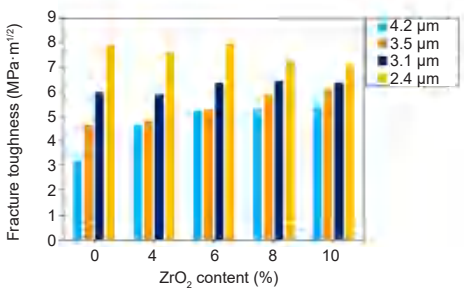

Figure 12. Effect of ZrO_2 content on fracture toughness at various grain sizes. ZrO_2: zirconium dioxide.

Ceramic materials used in dental implants and other structural applications primarily involve a transformation toughening process. Zirconia undergoes a crystallographic phase transformation when subjected to certain stress conditions, which imparts enhanced toughness and resistance to crack propagation. This transformation toughening mechanism is key to improving the overall mechanical reliability of zirconia ceramics.

Tetragonal to monoclinic transformation works as follows, zirconia exists in several crystallographic phases, with the most relevant ones for dental applications being tetragonal and monoclinic phases. Under normal conditions, zirconia is stabilised in its tetragonal phase due to the addition of stabilizing elements like yttria (Y_2O_3) during the manufacturing process. By harnessing this transformation toughening mechanism, zirconia ceramics can exhibit improved fracture toughness and resistance to crack propagation. This property is highly beneficial in dental implant materials, where the prevention of cracks and the ability to withstand chewing forces are critical for long-term performance and durability.[56]

Flexural strength

Flexural strength is increased by the addition of increasing amounts of Ti and Mg ceramic particles. This strength has improved up to 625 MPa in a single direction. The addition of graphene reinforcement to the zirconia will give a 30% improvement in flexural strength value of 590 MPa, mainly in monolithic zirconia. If the material is very dense, meaning it achieves better flexural strength, then due to the density, the strength increases up to 47 MPa. In the case of ATZ, the composite has produced a range of flexural strength between 450–700 MPa due to the greater content of zirconia.[57] At the same time, 604 MPa is also predicted in the ZTA.[58] Here also, grain size plays a significant role in improving implant strength. Thus, minimizing the grain size will help achieve a higher range of strength. The tetragonal grains give tremendous strength values to dental implant materials; the range is 1000 MPa to 1300 MPa. Ceria-stabilised zirconia gives the highest flexural strength value at 1500 MPa. From this, monolithic zirconia is only suitable for particular strength basis applications, so combinations of zirconia and other oxides give higher flexural strength. The effect of TiO_2 content on flexural strength for various sintering temperatures gives better flexural strength at a 5% addition of TiO_2 with all sintering temperatures.[59] **Figure 13** shows the effect of ZrO_2 content on flexural strength at various sintering temperatures. The mechanical properties of the zirconia implant materials are shown in **Figure 14**. The systematically-collected literature of materials, methods, and results of analysis of mechanical properties for ceramic composites from various research papers in recent years are listed in **Table 3**. *In-vitro* testing involves subjecting dental implant materials to controlled laboratory conditions. Flexural strength testing measures the material's ability to withstand bending or flexing forces. This is typically done using a three-point or four-point bending test setup. Higher flexural strength indicates better resistance to bending and potential for withstanding occlusal forces in the oral environment. The most common method for determining fracture toughness is using the single-edge notched beam test or compact tension test. Higher fracture toughness values indicate a greater ability to resist crack initiation and propagation, which is essential for preventing implant failure due to stress concentration and fatigue.[17]

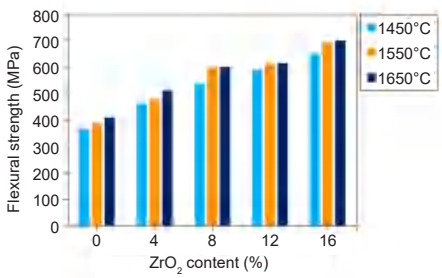

Figure 13. Effect of ZrO_2 content on flexural strength at various sintering temperatures. ZrO_2: zirconium dioxide.

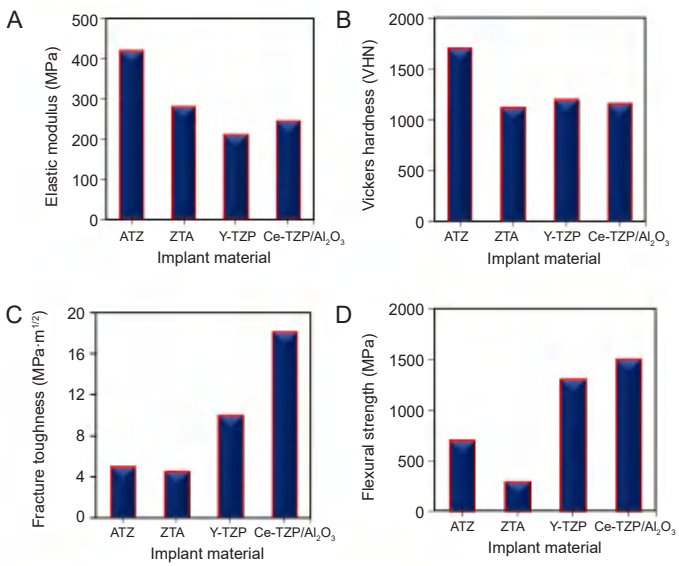

Figure 14. Mechanical properties of different implant materials. (A) Elastic modulus. (B) Vickers hardness. (C) Fracture toughness. (D) Flexural strength. Al_2O_3: aluminium dioxide; AZT: alumina toughened zirconia; TPZ: tetragonal phase zirconia; Y-TZP: Yttria-stabilised tetragonal zirconia polycrystalline; ZTA: zirconia toughened alumina.

Table 3. Systematic literature collection of results from recent research

Studies	Ceramic composites	Method of mixing	Conditions for sintering	Results
Liu et al.[4]	Al_2O_3–ZrB_2–MgO/ Al_2O_3–TiN–MgO	Planetary ball milling machine, alumina ball to powder ratio 1:3	Hot pressed, vacuum at 1650°C, 60 minutes under 35 MPa.	Flexural strength = 654 ± 43 MPa, fracture toughness = 8.7 ± 0.2 MPa·$m^{1/2}$, Vickers hardness = 20.1 ± 0.5 GPa, elastic modulus = 351 GPa
Tovar-Vargas et al.[59]	Yttrium doped ZrO_2–Al_2O_3 composite powders with partially stabilised ZrO_2 (PSZ)	Wet ball milling	Pressing (370 MPa); Sintering (1600°C/5 hours)	Highest Kc ~8.40 ± 0.4 MPa and hardness ~16.31 ± 0.58 GPa were obtained for the 30 wt% PSZ-Al_2O_3
Smirnov et al.[21]	Hierarchical tantalum-graphene flakes reinforced zirconia	Ball milling	Spark plasma sintering (maximum temperatures of 1400 and 1500°C under vacuum at a heating rate of 100°C/min, and applied pressure of 80 MPa)	Flexural strength 30% increment and toughness 175% increase compared to monolithic Zr
Liu et al.[60]	ρ-Al_2O_3	Wet-milled with a rotating speed of 300 r/min for 3 hours	Compacted at 10 MPa, sintered at a heating rate of 5°C/min to 1600°C, 3 hours	Hot modulus of rupture = 6.26 MPa, thermal shock resistance = 2.53
Yan et al.[36]	ZrB_2–SiC–Ni	Ball-milled for 12 hours	Spark plasma sintering	Fracture toughness = 8.3 MPa,
Smirnov et al.[39]	3Y-TZP/Ta	High-energy ball milling	spark plasma sintering, vacuum (≈ 1 × 10^2 Mbar) at 1400°C, 200°C/min	Flexural strength = 967 MPa, surface roughness Ra = 0.3 ± 0.1
Prajzler et al.[40]	Alumina based zirconia ceramics	Ball milling	Pressureless rapid rate sintering (100°C/min to 1500°C/min)	Nearly total density (> 95% TD) without forming cracks or other structural defects.
Ke et al.[41]	WcoB-TiC	Planetary ball milling machine	Sintering at 1500°C, 60 minutes	Hardness = 91.6 HRA, transverse rapture strength = 1783 MPa.
Cheng et al.[43]	Porous Si_3N_4–Si_3N_4	Ball milling	Sintering and 3D printing combined with low-pressure chemical vapour infiltration	Density increased from 0.99 to 2.02 g/cm^3 flexural strength of 47 ± 2 MPa
Manshor et al.[61]	TiO_2 (ZTA–TiO_2) Cr_2O_3	Ball milling	Sintering 1600°C for 1 hour with 5°C/min	Fracture toughness increased to 7.15 MPa·$m^{1/2}$ by adding up to 0.6 wt% Cr_2O_3
Zhu et al.[62]	$MgTiO_3$/CaO-B_2O_3-SiO_2	Ball milling with ethyl alcohol for 300 minutes	Sintered at 810°C, 120 minutes	Bulk density = 3.1270 g/cm^3, flexural strength = 214.85 MPa
Wang et al.[63]	Al_2O_3/TiC	Hybrid slurries form ball-milling for 60 hours	Hot-pressing sintering 1700–1750°C in a nitrogen atmosphere, 35 MPa	Fracture toughness = 97 MPa·$m^{1/2}$, Vickers hardness = 37 GPa
Zhang et al.[64]	SiAlON–Si_3N_4	Ball milling	Reaction-bonded sintering, 4°C/min to 1500°C	Compressive strength = 185 MPa
Zhao et al.[65]	ZrB_2–SiC–Ni	Ball-milled for 12 hours using ZrO_2 ball media	Spark plasma sintering, 1400°C for 1 minute, 200°C/min	Hardness = 20.2 GPa, elastic modulus of ZS =53.7 GPa
Li et al.[66]	CM_2A_8 ($CaMg_2Al_{16}O_{27}$) and $C_2M_2A_{14}$ ($Ca_2Mg_2Al_{28}O_{46}$)	Calcinated at 900°C for 1 hour	Hot press sintering 1750°C, 15 MPa.	Vickers hardness = 12.95 GPa, fracture toughness = 2.17 MPa, flexural strength = 248 MPa

Note: 3D: three-dimensional; Al_2O_3: aluminium dioxide; B_2O_3: boron trioxide; $C_2M_2A_{14}$: stable calcium aluminate phase; CaO: calcium oxide; CM_2A_8: ternary stable calcium aluminate phase; Cr_2O_3: chromic oxide; Kc: fracture toughness; MgO: magnesium oxide; $MgTiO_3$: magnesium titanium oxide; Si_3N_4: silicon nitride; SiAlON: formation of silicon nitride, aluminium oxide and aluminium nitride; SiC: silicon carbide; SiO_2: silicon dioxide; TD: total density; TiC: titanium carbide; TiN: titanium nitride; TiO_2: titanium dioxide; WCoB: tungsten cobalt boron; Y-TZP: yttria-stabilised tetragonal zirconia polycrystalline; ZrB_2: zirconium diboride; ZrO_2: zirconium dioxide; ZS: zirconium diboride with silicon carbide; ZTA: zirconia-toughened alumina.

Ex-vitro analysis involves assessing dental implant materials in real-world clinical settings, such as in patients' mouths. This includes monitoring patients over an extended period to evaluate the long-term performance of the implants. Clinical studies provide valuable information on how implants perform under actual oral conditions, considering factors like occlusal forces, oral hygiene, and patient habits.[18]

Conclusion and Future Scope

The current scenario of zirconia ceramics in dental applications has been providing expected mechanical properties and biological integration enhancement in the material world.

• The application of zirconia-based CMCs can be an excellent alternative to titanium-based implants because of the rapid developments in the medical field. In the last decade, the

application of dental zirconia and alumina-based ceramics has improved.

• Implant fabrication in conventional methods has manifested some limitations, so there is a need to improve densified composites that advanced sintering techniques can achieve. Computer-aided design-oriented 3D manufacturing techniques also provide a suitable route to achieve near net shape without material waste.

• Mechanical perspective comes with clinical research aspects that keep on searching for materials to replace titanium implants. Most researchers focus on AZT and ZTA alone, without any combination, mainly bio oxides.

• The future focus of dental implant material with biocompatible oxides helps to further enhance the performance of the implant, such as resistance to minor fracture, strength, and functionality. The different combinations of zirconia implants can be a promising alternative that is looking to refine mechanical competencies. Collaboration of clinical dentistry research with *in-vitro* and *in-vivo* studies of enhanced bioceramic composites and material processing technologies is required for rapid development in bioceramic research.

Dental implant technology is continually evolving, and review papers may become outdated relatively quickly. New materials, techniques, and research findings may emerge after this review has been published. Review papers often focus on a specific aspect of dental ceramic implants or a subset of relevant studies. This limited scope may not cover all available research or provide a comprehensive overview of the field.

Author contributions

MT: Conceptualization, data curation, writing - original draft, writing - review & editing; AVMS: supervision, review & editing. Both authors reviewed and approved the final version of the manuscript.

Financial support

None.

Acknowledgement

The first author would like to give his sincere thanks to Dr. M.S. Aezhisai Vallavi for their immense support and valuable suggestions.

Conflicts of interest statement

The authors declare that they have no conflict of interest.

1. Wójcik, N. A.; Tagiara, N. S.; Möncke, D.; Kamitsos, E. I.; Ali, S.; Ryl, J.; Barczyński, R. J. Mechanism of hopping conduction in Be–Fe–Al–Te–O semiconducting glasses and glass–ceramics. *J Mater Sci.* **2022**, *57*, 1633-1647.
2. Magnani, G.; Fabbri, P.; Leoni, E.; Salernitano, E.; Mazzanti, F. New perspectives on zirconia composites as biomaterials. *J Compos Sci.* **2021**, *5*, 244.
3. Taeh, A. S.; Othman, F. M.; Abdul-Hamead, A. A. Reviewing alumina-zirconia composite as a ceramic biomaterial. *Hunan Daxue Xuebao.* **2022**, *49*, 263-273.
4. Liu, C.; Sun, J.; Li, G.; Li, B.; Gong, F. Fabrication, mechanical properties and fracture behaviors of the laminated Al_2O_3–ZrB_2–MgO / Al_2O_3–TiN–MgO ceramic composite. *Ceram Int.* **2020**, *46*, 857-865.
5. Williams, T.; Yeomans, J.; Smith, P.; Heaton, A.; Hampson, C. Effect of interfacial area on densification and microstructural evolution in silicon carbide–boron carbide particulate composites. *J Mater Sci.* **2016**, *51*, 353-361.
6. Alcudia-Ramos, M. A.; Fuentez-Torres, M. O.; Ortiz-Chi, F.; Espinosa-González, C. G.; Hernández-Como, N.; García-Zaleta, D. S.; Kesarla, M. K.; Torres-Torres, J. G.; Collins-Martínez, V.; Godavarthi, S. Fabrication of g-C_3N_4/TiO_2 heterojunction composite for enhanced photocatalytic hydrogen production. *Ceram Int.* **2020**, *46*, 38-45.
7. Pradhan, S.; Singh, S.; Prakash, C.; Królczyk, G.; Pramanik, A.; Pruncu, C. I. Investigation of machining characteristics of hard-to-machine Ti-6Al-4V-ELI alloy for biomedical applications. *J Mater Res Technol.* **2019**, *8*, 4849-4862.
8. Saeed, F.; Muhammad, N.; Khan, A. S.; Sharif, F.; Rahim, A.; Ahmad, P.; Irfan, M. Prosthodontics dental materials: From conventional to unconventional. *Mater Sci Eng C Mater Biol Appl.* **2020**, *106*, 110167.
9. Lin, C.; Zhao, Q.; Zhao, X.; Yang, Y. Cavitation erosion of metallic materials. *Int J Georesources Environment.* **2018**, *4*, 1-8.
10. Ramachandran, K.; Boopalan, V.; Bear, J. C.; Subramani, R. Multi-walled carbon nanotubes (MWCNTs)-reinforced ceramic nanocomposites for aerospace applications: a review. *J Mater Sci.* **2022**, *57*, 3923-3953.
11. Meena, K. L.; Vidyasagar, C. S.; Benny Karunakar, D. Mechanical and tribological properties of MgO/multiwalled carbon nanotube-reinforced zirconia-toughened alumina composites developed through spark plasma sintering and microwave sintering. *J Mater Eng Perform.* **2022**, *31*, 682-696.
12. Condi Mainardi, J.; Bonini Demarchi, C.; Mirdrikvand, M.; Karim, M. N.; Dreher, W.; Rezwan, K.; Maas, M. 3D bioprinting of hydrogel/ceramic composites with hierarchical porosity. *J Mater Sci.* **2022**, *57*, 3662-3677.
13. Bartoli, M.; Duraccio, D.; Faga, M. G.; Piatti, E.; Torsello, D.; Ghigo, G.; Malucelli, G. Mechanical, electrical, thermal and tribological behavior of epoxy resin composites reinforced with waste hemp-derived carbon fibers. *J Mater Sci.* **2022**, *57*, 14861-14876.
14. Osman, R. B.; Swain, M. V. A critical review of dental implant materials with an emphasis on titanium versus zirconia. *Materials (Basel).* **2015**, *8*, 932-958.
15. Tartsch, J.; Blatz, M. B. Ceramic dental implants: an overview of materials, characteristics, and application concepts. *Compend Contin Educ Dent.* **2022**, *43*, 482-488; quiz 489.
16. Thanigachalam, M.; Muthusamy Subramanian, A. V. Evaluation of PEEK-TiO(2)- SiO(2) nanocomposite as biomedical implants with regard to in-vitro biocompatibility and material characterization. *J Biomater Sci Polym Ed.* **2022**, *33*, 727-746.
17. Muthusamy Subramanian, A. V.; Thanigachalam, M. Mechanical performances, in-vitro antibacterial study and bone stress prediction of ceramic particulates filled polyether ether ketone nanocomposites for medical applications. *J Polym Res.* **2022**, *29*, 318.
18. Thanigachalam, M.; Muthusamy Subramanian, A. V. In-vitro cytotoxicity assessment and cell adhesion study of functionalized nTiO2 reinforced PEEK biocompatible polymer composite. *Polym Plasts Technol Mater.* **2022**, *61*, 566-576.
19. Mugilan, T.; Aezhisai Vallavi, M. S.; Sugumar, D. Materialistic characterization, thermal properties, and cytocompatibility investigations on acrylic acid-functionalized nSiO2-reinforced PEEK polymeric nanocomposite. *Colloid Polym Sci.* **2022**, *300*, 1155-1168.
20. Zhai, X.; Zhang, X.; Ma, Y.; Liu, J. Influence of Bi_2O_3, TiO_2 additives

and sintering process on the performance of ITO target based on normal pressure sintering method. *Trans Indian Ceramic Soc.* **2019**, *78*, 83-88.

21. Smirnov, A.; Peretyagin, P.; Bartolomé, J. F. Processing and mechanical properties of new hierarchical metal-graphene flakes reinforced ceramic matrix composites. *J Eur Ceram Soc.* **2019**, *39*, 3491-3497.
22. Qian, K.; Yao, Z.; Lin, H.; Zhou, J.; Haidry, A. A.; Qi, T.; Chen, W.; Guo, X. The influence of Nd substitution in Ni–Zn ferrites for the improved microwave absorption properties. *Ceram Int.* **2020**, *46*, 227-235.
23. Ghosh, R.; Sarkar, R. Comparative analysis of novel calcium phosphate based machinable bioceramic composites. *Trans Indian Ceramic Soc.* **2020**, *79*, 131-138.
24. Raghavendra, C. R.; Basavarajappa, S.; Sogalad, I.; Naik, K. Study on wear mechanism and contact temperature against dry sliding wear of Ni-Al2O3 nanocomposite coating. *Trans Indian Ceramic Soc.* **2020**, *79*, 139-143.
25. Yadav, P.; Rattan, S.; Tripathi, A.; Kumar, S. Tailoring of complex permittivity, permeability, and microwave-absorbing properties of CoFe2O4/NG/PMMA nanocomposites through swift heavy ions irradiation. *Ceram Int.* **2020**, *46*, 317-324.
26. Liu, C.; Li, X.; Wu, Y.; Zhang, L.; Chang, X.; Yuan, X.; Wang, X. Fabrication of multilayer porous structured TiO_2–$ZrTiO_4$–SiO_2 heterostructure towards enhanced photo-degradation activities. *Ceram Int.* **2020**, *46*, 476-486.
27. Avcıoğlu, S.; Buldu, M.; Kaya, F.; Üstündağ, C. B.; Kam, E.; Menceloğlu, Y. Z.; Kaptan, H. Y.; Kaya, C. Processing and properties of boron carbide (B_4C) reinforced LDPE composites for radiation shielding. *Ceram Int.* **2020**, *46*, 343-352.
28. Zhang, H.; Li, M.; Zhu, C.; Tang, Q.; Kang, P.; Cao, J. Preparation of magnetic α-Fe_2O_3/$ZnFe_2O_4$@Ti_3C_2 MXene with excellent photocatalytic performance. *Ceram Int.* **2020**, *46*, 81-88.
29. Zhang, Z.; Lin, T.; Shao, H.; Peng, J.; Wang, A.; Zhang, Y.; Yu, X.; Liu, S.; Wang, L.; Zhao, M. Effect of different dopants on porous calcium silicate composite bone scaffolds by 3D gel-printing. *Ceram Int.* **2020**, *46*, 325-330.
30. Song, S.; Gao, Z.; Lu, B.; Bao, C.; Zheng, B.; Wang, L. Performance optimization of complicated structural SiC/Si composite ceramics prepared by selective laser sintering. *Ceram Int.* **2020**, *46*, 568-575.
31. Su, N. K.; Rejab, N. A.; Ahmad, Z. A.; Abdullah, N. S. Densification of zirconia toughened alumina added CeO_2 ceramics via hot isostatic press sintering technique. *Key Eng Mater.* **2022**, *908*, 228-233.
32. Thankachan, T.; Soorya Prakash, K.; Malini, R.; Ramu, S.; Sundararaj, P.; Rajandran, S.; Rammasamy, D.; Jothi, S. Prediction of surface roughness and material removal rate in wire electrical discharge machining on aluminum based alloys/composites using Taguchi coupled Grey Relational Analysis and Artificial Neural Networks. *Appl Surf Sci.* **2019**, *472*, 22-35.
33. Adibpur, F.; Tayebifard, S. A.; Zakeri, M.; Shahedi Asl, M. Spark plasma sintering of quadruplet ZrB_2–SiC–ZrC–Cf composites. *Ceram Int.* **2020**, *46*, 156-164.
34. Gil-Flores, L.; Salvador, M. D.; Penaranda-Foix, F. L.; Dalmau, A.; Fernández, A.; Borrell, A. Tribological and wear behaviour of alumina toughened zirconia nanocomposites obtained by pressureless rapid microwave sintering. *J Mech Behav Biomed Mater.* **2020**, *101*, 103415.
35. Xia, Y.; Mou, J.; Deng, G.; Wan, S.; Tieu, K.; Zhu, H.; Xue, Q. Sintered ZrO_2–TiO_2 ceramic composite and its mechanical appraisal. *Ceram Int.* **2020**, *46*, 775-785.
36. Yan, X.; Jin, X.; Li, P.; Hou, C.; Hao, X.; Li, Z.; Fan, X. Microstructures and mechanical properties of ZrB_2–SiC–Ni ceramic composites prepared by spark plasma sintering. *Ceram Int.* **2019**, *45*, 16707-16712.
37. Cui, E.; Zhao, J.; Wang, X. Determination of microstructure and mechanical properties of graphene reinforced Al_2O_3-Ti(C, N) ceramic composites. *Ceram Int.* **2019**, *45*, 20593-20599.
38. Turon-Vinas, M.; Anglada, M. Strength and fracture toughness of zirconia dental ceramics. *Dent Mater.* **2018**, *34*, 365-375.
39. Smirnov, A.; Peretyagin, P.; Bartolomé, J. F. Wire electrical discharge machining of 3Y-TZP/Ta ceramic-metal composites. *J Alloys Compd.* **2018**, *739*, 62-68.
40. Prajzler, V.; Salamon, D.; Maca, K. Pressure-less rapid rate sintering of pre-sintered alumina and zirconia ceramics. *Ceram Int.* **2018**, *44*, 10840-10846.
41. Ke, D.; Pan, Y.; Wu, R.; Xu, Y.; Wang, P.; Wu, T. Effect of initial Co content on the microstructure, mechanical properties and high-temperature oxidation resistance of WCoB-TiC ceramic composites. *Ceram Int.* **2018**, *44*, 1213-1219.
42. Rakshit, R.; Das, A. K. A review on cutting of industrial ceramic materials. *Precis Eng.* **2019**, *59*, 90-109.
43. Cheng, Z.; Ye, F.; Liu, Y.; Qiao, T.; Li, J.; Qin, H.; Cheng, L.; Zhang, L. Mechanical and dielectric properties of porous and wave-transparent Si_3N_4-Si_3N_4 composite ceramics fabricated by 3D printing combined with chemical vapor infiltration. *J Adv Ceram.* **2019**, *8*, 399-407.
44. Srinivasan, V. P.; Palani, P. K.; Selvarajan, L. Experimental investigation on electrical discharge machining of ceramic composites (Si_3N_4-TiN) using RSM. *Int J Comput Mater Sci Surf Eng.* **2018**, *7*, 104-115.
45. Kuntz, M.; Krüger, R. The effect of microstructure and chromia content on the properties of zirconia toughened alumina. *Ceram Int.* **2018**, *44*, 2011-2020.
46. Monzavi, M.; Zhang, F.; Meille, S.; Douillard, T.; Adrien, J.; Noumbissi, S.; Nowzari, H.; Chevalier, J. Influence of artificial aging on mechanical properties of commercially and non-commercially available zirconia dental implants. *J Mech Behav Biomed Mater.* **2020**, *101*, 103423.
47. Gao, P. Z.; Cheng, L.; Yuan, Z.; Liu, X.-p.; Xiao, H.-n. High temperature mechanical retention characteristics and oxidation behaviors of the $MoSi_2(Cr_5Si_3)$—RSiC composites prepared via a PIP—AAMI combined process. *J Adv Ceram.* **2019**, *8*, 196-208.
48. Machaka, R.; Derry, T. E.; Sigalas, I.; Herrmann, M. Analysis of the Indentation Size Effect in the Microhardness Measurements in B_6O. *Adv Mater Sci Eng.* **2011**, *2011*, 539252.
49. Singaravel Chidambara Nathan, A.; Tah, R.; Balasubramanium, M. K. Evaluation of fracture toughness of zirconia silica nano-fibres reinforced feldespathic ceramic. *J Oral Biol Craniofac Res.* **2018**, *8*, 221-224.
50. Liao, Y.; Wang, Y.; Chen, Z.; Wang, X.; Li, J.; Guo, R.; Liu, C.; Gan, G.; Wang, G.; Li, Y.; Zhang, H. Microstructure and enhanced magnetic properties of low-temperature sintered LiZnTiMn ferrite ceramics with Bi_2O_3-Al_2O_3 additive. *Ceram Int.* **2020**, *46*, 487-492.
51. Talimian, A.; Galusek, D. Aqueous slip casting of translucent magnesium aluminate spinel: Effects of dispersant concentration and solid loading. *Ceram Int.* **2019**, *45*, 10646-10653.
52. Hou, P. J.; Guo, Y. F.; Sun, L. X.; Deng, G. Q. Simulation of temperature and thermal stress filed during reciprocating traveling WEDM of insulating ceramics. *Procedia CIRP.* **2013**, *6*, 410-415.
53. Caravaca, C. F.; Flamant, Q.; Anglada, M.; Gremillard, L.; Chevalier, J. Impact of sandblasting on the mechanical properties and aging

resistance of alumina and zirconia based ceramics. *J Eur Ceram Soc.* **2018**, *38*, 915-925.
54. Jindal, P. C. A new method for evaluating the indentation toughness of hardmetals. *Crystals.* **2018**, *8*, 197.
55. Ahmad, I.; Islam, M.; Al Habis, N.; Parvez, S. Hot-pressed graphene nanoplatelets or/and zirconia reinforced hybrid alumina nanocomposites with improved toughness and mechanical characteristics. *J Mater Sci Technol.* **2020**, *40*, 135-145.
56. Chen, X.; Liu, C.; Zheng, W.; Han, J.; Zhang, L.; Liu, C. High strength silica-based ceramics material for investment casting applications: Effects of adding nanosized alumina coatings. *Ceram Int.* **2020**, *46*, 196-203.
57. Yu, H.; Hou, Z.; Guo, X.; Chen, Y.; Li, J.; Luo, L.; Li, J.; Yang, T. Finite element analysis on flexural strength of Al_2O_3-ZrO_2 composite ceramics with different proportions. *Mater Sci Eng A.* **2018**, *738*, 213-218.
58. Rao, P. K.; Jana, P.; Ahmad, M. I.; Roy, P. K. Synthesis and characterization of zirconia toughened alumina ceramics prepared by co-precipitation method. *Ceram Int.* **2019**, *45*, 16054-16061.
59. Tovar-Vargas, D.; Roitero, E.; Anglada, M.; Jiménez-Piqué, E.; Reveron, H. Mechanical properties of ceria-calcia stabilized zirconia ceramics with alumina additions. *J Eur Ceram Soc.* **2021**, *41*, 5602-5612.
60. Liu, J.; Huo, W.; Zhang, X.; Ren, B.; Li, Y.; Zhang, Z.; Yang, J. Optimal design on the high-temperature mechanical properties of porous alumina ceramics based on fractal dimension analysis. *J Adv Ceram.* **2018**, *7*, 89-98.
61. Manshor, H.; Azhar, A. Z. A.; Rashid, R. A.; Sulaiman, S.; Abdullah, E. C.; Ahmad, Z. A. Effects of Cr_2O_3 addition on the phase, mechanical properties, and microstructure of zirconia-toughened alumina added with TiO_2 (ZTA–TiO_2) ceramic composite. *Int J Refract Met Hard Mater.* **2016**, *61*, 40-45.
62. Zhu, X.; Kong, F.; Ma, X. Sintering behavior and properties of $MgTiO_3$/CaO-B_2O_3-SiO_2 ceramic composites for LTCC applications. *Ceram Int.* **2019**, *45*, 1940-1945.
63. Wang, X.; Zhao, J.; Cui, E.; Song, S.; Liu, H.; Song, W. Microstructure, mechanical properties and toughening mechanisms of graphene reinforced Al_2O_3-WC-TiC composite ceramic tool material. *Ceram Int.* **2019**, *45*, 10321-10329.
64. Zhang, L.; Liu, X.; Li, M.; Xu, E.; Zhao, F.; Yuan, H.; Sun, X.; Zhang, C.; Gao, L.; Gao, J. Feasibility of SiAlON–Si_3N_4 composite ceramic as a potential bone repairing material. *Ceram Int.* **2020**, *46*, 1760-1765.
65. Zhao, H.; Li, Z.; Zhang, M.; Li, J.; Wu, M.; Li, X.; Chen, J.; Xie, M.; Li, J.; Sun, X. High-performance Al_2O_3–YAG:Ce composite ceramic phosphors for miniaturization of high-brightness white light-emitting diodes. *Ceram Int.* **2020**, *46*, 653-662.
66. Li, B.; Li, G.; Chen, H.; Chen, J.; Hou, X.; Li, Y. Physical and mechanical properties of hot-press sintering ternary CM_2A_8 ($CaMg_2Al_{16}O_{27}$) and $C_2M_2A_{14}$ ($Ca_2Mg_2Al_{28}O_{46}$) ceramics. *J Adv Ceram.* **2018**, *7*, 229-236.

Received: June 30, 2023
Revised: August 7, 2023
Accepted: September 8, 2023
Available online: September 28, 2023

Research progress and clinical translation of three-dimensional printed porous tantalum in orthopaedics

*Jiawei Ying, Haiyu Yu, Liangliang Cheng, Junlei Li, Bin Wu, Liqun Song, Pinqiao Yi, Haiyao Wang, Lingpeng Liu, Dewei Zhao**

Key Words:
3D printed; additive manufacturing; orthopaedic implant; porous; tantalum

From the Contents

ABSTRACT

With continuous developments in additive manufacturing technology, tantalum (Ta) metal has been manufactured into orthopaedic implants with a variety of forms, properties and uses by three-dimensional printing. Based on extensive research in recent years, the design, processing and performance aspects of this new orthopaedic implant material have been greatly improved. Besides the bionic porous structure and mechanical characteristics that are similar to human bone tissue, porous tantalum is considered to be a viable bone repair material due to its outstanding corrosion resistance, biocompatibility, bone integration and bone conductivity. Numerous in vitro, in vivo, and clinical studies have been carried out in order to analyse the safety and efficacy of these implants in orthopaedic applications. This study reviews the most recent advances in manufacturing, characteristics and clinical application of porous tantalum materials.

***Corresponding author:**
Dewei Zhao,
zhaodewei2016@163.com.

http://doi.org/10.12336/biomatertransl.2023.03.005

How to cite this article:
Ying, J.; Yu, H.; Cheng, L.; Li, J.; Wu, B.; Song, L.; Yi, P.; Wang, H.; Liu, L.; Zhao D. Research progress and clinical translation of three-dimensional printed porous tantalum in orthopaedics. *Biomater Transl.* **2023**, *4*(3), 166-179.

Introduction

Injuries to the musculoskeletal system are mainly caused by trauma or bone disease. Bone defects are an especially common clinical problem, resulting in significantly-reduced quality of life for millions of patients every year. Although autologous or allogeneic bone transplantation can partially repair bone defects, there are problems such as source limitation, and risks of donor site complications and infectious diseases. Therefore, finding more suitable bone substitute materials is the focus and hot spot of tissue engineering research.[1, 2] The optimum substance for a bone implant should not only have the same elastic modulus and mechanical strength as bone, but also have good histocompatibility and bone integration ability. At present, the most commonly used metal grafts, represented by pure titanium (Ti), titanium alloy or stainless steel, are difficult to adapt to the requirements of bone replacement because of problems including cytotoxicity, low histocompatibility, rapid wear, and high elastic modulus. As a new metal graft material, porous tantalum (Ta) has attracted more and more interest due to its special microstructure, mechanical characteristics and good biocompatibility.[2, 3] In their review article, Han et al.[4] compare the research progress and clinical application of porous Ta and porous Ti fabricated by different methods. As additive manufacturing (AM) technology has advanced in recent years, an increasing number of studies have been carried out on three-dimensional (3D) printing of porous Ta and its gradual application

to orthopaedics. The research development and therapeutic application of AM porous Ta in bone tissue engineering are reviewed in this article.

An online search in PubMed, Web of Science, and Elsevier databases dating from 1990 to January 2023 was performed with the key words "additive manufacturing," "3D printed," "tantalum," "bone," and "orthopedics." Two researchers screened all the duplicated literature and checked the cited references independently for veracity. Inclusion criteria were studies reported in English or Chinese language, studies on Ta fabricated using AM technology, and studies related to orthopaedics. Studies were excluded when the Ta used in the studies was not prepared by 3D printing technology or applied to a field unrelated to orthopaedics.

Physical and Chemical Characteristics of Tantalum

Ta (atomic number 73, molecular weight 180.05) is a rare transition metal that is infrequently found in nature. Solid Ta has a density of 16.68 g/cm^3 and a hardness of 6–6.5 Mohs, which is close to diamond. Ta's melting point as a refractory metal is 3017°C. Porous Ta differs from solid metal Ta in its ultra-hardness and density. Porous Ta material has a 3D polyhedral pore structure visible under scanning electron microscopy that is similar to cancellous bone, and the porosity greatly lowers the density of porous Ta material. Ta in its purest form has relatively active chemical characteristics. Ta_2O_5 and TaO_2 are the two major oxide forms in which it is found. The surface of pure Ta spontaneously produces a persistent oxide layer that is non-conductive and resistant to the majority of strong acids and bases when Ta is exposed to air or treated.[5] Consequently Ta is very poorly soluble at all pH levels and potentials. Ta has great corrosion resistance as a result, and it can also lessen the frequency of local inflammation brought on by corrosion products.[6] By altering the surface hydrophobicity and electrostatic effects, the Ta_2O_5 oxide layer on the Ta surface gives good corrosion resistance and also increases cell adhesion. Boyan et al.[7] have demonstrated that hydrophilic surfaces are more favourable to cell adhesion and proliferation. Ta is quite hydrophobic, but as Ta_2O_5 forms, Ta becomes more hydrophilic. On the surface of pure Ta, the static water contact angle is 97.3 ± 4.2°, but it substantially drops to 6.3 ± 1.1° on the surface of Ta_2O_5.[8]

Porous Structure of Tantalum

Bone, including both cancellous bone and cortical bone, has open cells and a 3D interconnected porous structure. High-density orthopaedic implants have a high elastic modulus, which makes them vulnerable to stress shielding, osteolysis, and implant failure. Therefore, porous structures are of interest to researchers. The mechanical properties of 3D-printed Ta scaffolds are influenced by design elements such as porosity, pore size, strut diameter, and pore connectivity.[9]

The mechanical qualities, biocompatibility, and osteogenesis of implants are significantly influenced by the different geometric parameters of the pores in the material.[4, 10] Biemond et al.[11] investigated Ti_6Al_4V implants with wave-like and cuboidal pore designs. The friction coefficient of the wavy porous implant was higher than that of the cubic porous implant, while the bone ingrown depth of the cubic porous implant was much deeper than that of the wavy porous implant. When comparing Ta scaffolds with similar pore characteristics but different pore structures, Markhoff et al.[12] concluded that a pyramidal pore structure is most appropriate for cell migration and proliferation, and they successfully fabricated porous Ta scaffolds with pore geometry of diamond,[13] rhombic dodecahedron,[14] and biomimetic trabeculae.[15]

Cancellous bone has a porosity that ranges from 30% to 95%, and this high porosity provides enough space for cell migration as well as for the transport of nutrients and oxygen.[16, 17] A vast amount of biological research has revealed that implants with higher porosity are more favourable to cell proliferation and bone formation, and also improve biocompatibility, osteogenesis and vascularisation.[12, 17] Wauthle et al.[18] examined the biological characteristics of porous Ta scaffolds generated by selective laser melting (SLM) with a porosity of 80% and determined that high porosity gives good biocompatibility, bone conductivity, and osteogenesis. **Figure 1** presents scanning electron microscopic images of 3D-printed Ta scaffolds with varying porosities.

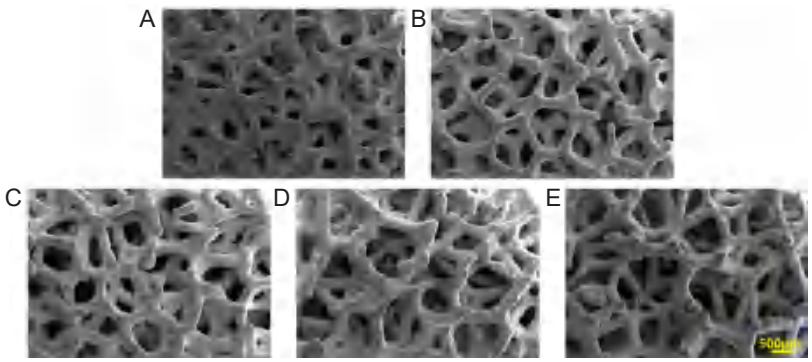

Figure 1. Scanning electron microscopic images of selective laser melting-fabricated porous Ta scaffolds with different porosities. (A–E) 60%, 65%, 70%, 75%, and 80%. Reprinted from Gao et al.[9] Scale bar: 500 μm.

Department of Orthopaedics, Affiliated Zhongshan Hospital of Dalian University, Dalian, Liaoning Province, China

In addition, pore interconnectivity, pore size, and strut diameter are also involved in the mechanical and biological aspects of 3D-printed porous Ta scaffolds. Strut diameter has a significant effect on the mechanical properties of the scaffold, while interpore connectivity plays a significant part in bone conduction, osseointegration, and bone ingrowth.[17] To achieve the desired requirements, the structural parameters of the various pores should be balanced in the Ta scaffold.

Three-Dimensional Printed Porous Tantalum

AM has been identified as a powerful and adaptable processing approach capable of generating porous orthopaedic implants when highly personalised, precise and complicated structures are required. A variety of 3D-printing technologies have been developed in recent years, including SLM, electron beam melting (EBM), direct metal deposition, direct metal printing, fused deposition modelling, direct metal writing, and binder jetting. Among them, SLM and EBM have become the most frequently-utilised technologies for manufacturing porous metal scaffolds because of their benefits of high accuracy, high efficiency, and good stability.

There are similarities in the composition and manufacturing methods of these two technologies. In both systems the point platform rises continually, providing the metal powder, while the blade moves the new Ta powder onto the building platform, where the scaffold is built.

Metal powders are fused together into solid pieces using a laser or electron beam. After the powder layer is established, the frame platform falls, and the next layer of Ta powder that is deposited is hit by the application from the material distribution platform. When the whole construction is complete, the created item is cut free from its base.[10] The difference is that SLM uses a high-energy laser while EBM uses an electron beam. **Figure 2** shows the working mechanism of the SLM and EBM machines.[19, 20]

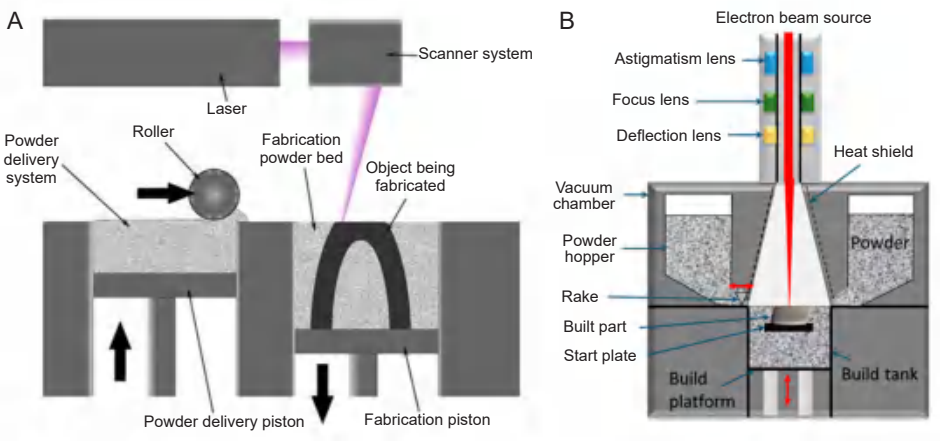

Figure 2. (A) Schematic of the selective laser melting process. Reprinted from Kamran and Farid.[19] (B) An electron beam melting machine. Reprinted from Azam et al.[20]

Compared with chemical vapour deposition and powder metallurgy, the pore formation mechanism of AM is different, resulting in different pore structure characteristics. This allows the AM scaffold to have the finest connectivity and the most adjustable pore characteristics with respect to parameters including strut diameter, pore size, and porosity. Moreover, by designing the geometry according to anatomically-matched requirements, AM can construct highly porous Ta scaffolds. Future porous Ta scaffold preparation will likely rely heavily on AM due to the continuing advances in 3D printing-related technology.

Mechanical Characteristics of Porous Tantalum

Clinical orthopaedic implant materials must have appropriate mechanical characteristics. Especially in the load-bearing area, the maximum strength and relatively low stiffness can enhance the initial biological fusion of the bone around the implant and ensure its long-term stability. In addition, significant indicators for determining the mechanical properties of Ta scaffolds in mechanical analysis include the compressive strength, elastic modulus, tensile strength, fatigue property, and friction coefficient.

The variations in compressive strength of Ta scaffolds are first caused by variations in the pore characteristics, structure, and manufacturing process. The compressive strength of porous Ta prepared using different techniques ranges from 14 to 480 MPa. Therefore, future studies will concentrate on 3D-printed Ta with more advanced compressive strength.[9] Porous Ta has an elastic modulus that is more comparable to that of natural bone than other metallic materials. Because 3D-printed Ta has an elastic modulus closer to that of cancellous bone (0.1–0.5 GPa) and cortical bone (12–18 GPa) than Ti (106–115 GPa), the stress shielding effect is reduced, bone resorption is prevented, and more nearby bone stores are protected.[21] Yang et al.[22] used 3D printing technology to prepare Ta trabecular scaffolds with porosity of 60%, 70% and 80%. In the three-point bending test, the bending strength was approximately 97, 52.8 and 23 MPa, respectively, indicating that as porosity decreased, porous Ta's

bending strength increased.[22] More research is required on the flexural strength of 3D-printed Ta scaffolds for extended bone healing, such as ways to enhance the flexural strength by changing the design and structure.

In addition, the fatigue performance of the fabricated porous Ta material also needs to be considered, which can be greatly impacted by different preparation methods. Zardiackas et al.[23] investigated the fatigue behaviour of a porous Ta scaffold prepared by chemical vapour deposition with a porosity of between 75% and 85%. After 5×10^6 cycles of compressive fatigue, the fatigue limit was 23 MPa, and the fatigue limit after 5×10^6 cycles of cantilever bending was 35 MPa.[23] In a compression–compression fatigue test, Wauthle et al.[18] investigated the compressive strength of a 3D-printed Ta scaffold with 80% porosity. They discovered a remarkably low fatigue limit (7.35 MPa at 10^6 cycles). Ta's porous nature and high coefficient of friction can provide additional friction between bone tissue and porous Ta. According to a report,[24] porous Ta has a 40% to 75% higher friction than a conventional porous coating, which is more suited to the stable fixation of an implant and increases surgical success rates.

These excellent mechanical characteristics make porous Ta an effective substitute for human bone tissue. Although the mechanical properties produced by different processing techniques are quite different, this just shows that porous Ta materials have considerable potential in orthopaedic applications, and more in-depth research is needed to identify better manufacturing parameters. For convenience, we have tabulated the mechanical characteristics of AM porous Ta compared with cancellous bone (**Table 1**).[25-28]

Table 1. Mechanical properties of 3D-printed porous Ta

	Manufacturing method	Porosity (%)	Elastic modulus (GPa)	Compressive strength (MPa)	Compressive yield strength (MPa)	Reference
Cancellous bone		50–90	0.01–3.0	–	2–12	25
Ta	SLM	79.7 ± 0.2	1.22 ± 0.07	3.61 ± 0.4	12.7 ± 0.6	15
		38–65	2–20	–	–	18
		68.3 ± 1.1	2.34 ± 0.2	78.54 ± 9.1	–	14
	LENS	27–55	1.5–20	–	–	26
	EBM	75–85	–	–	6.8–24	27
	LMLMC	35.48–50	2.8–9.0	56–480	–	28

Note: '–' indicates no available data. EBM: electron beam melting; LENS: laser near net shaping; LMLMC: laser multi-layer micro-cladding; SLM: selective laser melting; Ta: tantalum.

In Vitro Biological Characteristics of Porous Tantalum

Porous Ta metal has been favoured by researchers in recent years, not only because of its mechanical properties, but more importantly because of its good biocompatibility and good biological characteristics represented by promotion of osteogenesis.

Biocompatibility, cell adhesion, cytotoxicity and proliferation

Porous Ta scaffolds easily combine with oxygen to form a self-passivation surface oxide layer (Ta_2O_5).[29] In addition to preventing corrosion on the scaffold *in vivo*, the surface is extremely stable over a wide pH range. The surface of 3D-printed Ta promotes cell adhesion and proliferation due to its good biological characteristics and durable compatibility with different cell types.[30] With mouse fibroblasts (L929), a 3D-printed Ta scaffold created by Wauthle et al.[18] demonstrated good biocompatibility, promoting early integration and bone formation. Wei et al.[31] examined the effectiveness of porous Ta scaffolds in restoring significant cartilage defects in the weight-bearing area. Bone marrow mesenchymal stem cells (BMSCs) and chondrocytes were loaded onto a porous Ta scaffold and subsequently injected into a goat cartilage defect model. The fact that chondrocytes and BMSCs continued to thrive on porous Ta scaffolds 16 weeks after surgery supports the possibility that porous Ta is an important factor in the differentiation of BMSCs into osteoblasts.

The adhesion degree of early cells is crucial for the effective proliferation and differentiation of 3D-printed Ta surfaces.[9] Balla et al.[32] examined the morphological features of osteoblasts cultured on 3D-printed Ta for 3 days through scanning electron microscopy. Osteoblasts were flattened and evenly dispersed across the Ta surface. Comparable results were obtained by Wang et al.[15] and Guo et al.[14] (**Figure 3A**). Dou et al.[33] cultured BMSCs on 3D-printed Ta and porous Ti_6Al_4V, then after 1 day of incubation, they evaluated cell status and number of attachments by fluorescence microscopy in live and dead cells. In comparison to porous Ti_6Al_4V, morphological analysis of stromal stem cells on porous Ta revealed much greater adhesion and extension. Almost every cell on the surface of porous Ta was alive, indicating that porous Ta has good cytocompatibility.

The most frequently-used quantitative assays use 3-(4,5-dimethylthiazol-2-yl)-2,5-diphenyltetrazolium (MTT) or cell counting kit (CCK)-8, which are used to measure cytotoxicity typically through morphological inspection and evaluation of cell viability. Wang et al.[15] investigated whether 3D-printed Ta scaffolds were cytotoxic to mesenchymal stem cells in a 3-(4,5-dimethylthiazol-2-yl)-2,5-diphenyltetrazolium experiment. The optical density values of the Ta and the control group (cells in Dulbecco's modified Eagle medium)

showed no significant differences, indicating that porous Ta was not cytotoxic to human mesenchymal stem cells. The proliferation and behaviours of human fibroblasts, osteoblasts, and mesenchymal stem cells were examined by Gee et al.[34] in regard to the effects of porous Ta. They concluded that Ta did not interfere with biological functions in any of these three types of human cells. Other studies on cytotoxicity have also reached similar conclusions.[35, 36]

Dou et al.[33] and Guo et al.[14] used cell counting kit-8 to evaluate the proliferation of BMSCs on the surface of porous Ta and Ti_6Al_4V, and found that porous Ta had a substantially greater ability to promote cell proliferation than porous Ti_6Al_4V (**Figure 3B**).[33] Evaluation using the 3-(4,5-dimethylthiazol-2-yl)-2,5-diphenyltetrazolium measurement assay also reached the same conclusion.[37, 38]

Osteogenesis

Sagomonyants et al.[39] found that porous Ta significantly stimulated the proliferation of human osteoblasts and improved their osteogenic ability compared with other metal materials, and this effect was more prominent in osteoblasts from elderly individuals over 65 years old. Through scanning electron microscopic observation, Wang et al.[40] found that osteoblasts cultured *in vitro* adhered to, proliferated and formed various intercellular connections on the pore surfaces of porous Ta. According to studies,[39, 41] Ta increases the expression of genes associated with osteoblasts and certain cytokines while decreasing the expression of genes connected with osteoclasts. This encourages the proliferation, differentiation and mineralisation of osteoblasts. The findings demonstrated that the expressions of bone morphogenetic protein-2, alkaline phosphatase, osteocalcin, and osteopontin were noticeably greater in the experimental group than in the control group.[42] The differentiation potential of human foetal osteoblasts cultured on porous Ta and porous Ti scaffolds is similarly influenced by the expression of the alkaline phosphatase protein. Confocal images (**Figure 3C**) showed that porous Ta scaffolds had a higher expression of vinculin protein than porous Ti scaffolds.[32] Temponi et al.[38] assessed the biological behaviour of human peripheral blood mononuclear cells interacting with porous Ta. Porous Ta did not change the activity of peripheral blood mononuclear cells compared to the control group, while also allowing cell adhesion, reducing receptor activator of nuclear factor-kappa B ligand (RANKL) expression, and enhancing transforming growth factor-β expression.[43] In addition, the surface characteristics of implanted Ta can be modified using a variety of techniques, including sandblasting, alkali heat treatment, anodic oxidation, coating and surface functionalisation. These surface treatment technologies can enhance the osteogenic properties of the material.[44-47]

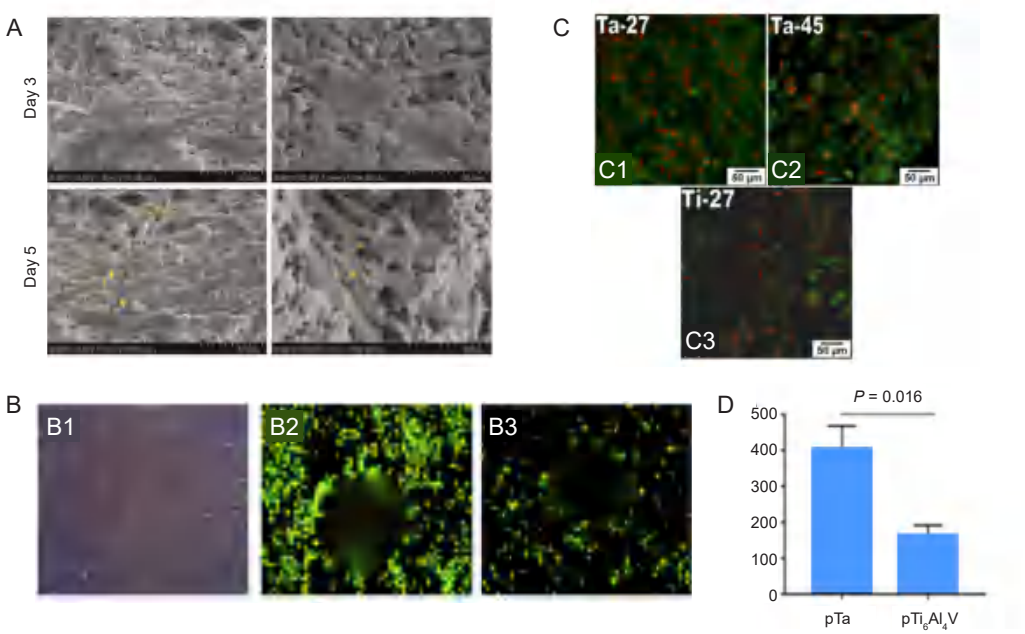

Figure 3. Cell adhesion and proliferation properties on porous Ta. (A) Morphology of mesenchymal stem cells (yellow arrows) cultured for 3 and 5 days. Reprinted from Wang et al.[15] (B) Light (B1) and fluorescence microscopic images of live-dead-stained bone marrow mesenchymal stem cells incubated on porous Ta (B2) and Ti_6Al_4V (B3) for 1 day, and quantification of the adherent cells (B4). Reprinted from Dox et al.[33](C) Confocal micrographs of vinculin expression on porous Ta with porosities of 27% (C1) and 45% (C2) and on porous Ti with 27% porosity (C3). Reprinted from Balla et al.[32] Copyright © 2010 Acta Materialia Inc. Scale bars: 50 μm. Ta: tantalum; Ti: titanium.

Angiogenesis

Oxygen and nutrients required for osteogenesis are delivered by newly-formed blood vessels, and the role of angiogenesis is to promote the continuing stability of bone implant materials.[47] Porous Ta, polydopamine–porous Ta scaffolds, polydopamine–magnesium ion porous Ta scaffolds, and polydopamine–strontium ion porous Ta scaffolds were all thoroughly investigated by Cheng et al.[49] for their impact

on the ability of human umbilical vein endothelial cells to form and migrate *in vitro*. Their findings confirmed that the porous Ta scaffold was beneficial to angiogenesis. *In vitro*, the vascularisation rate of porous Ta scaffold materials can be enhanced by the addition of Sr and Mg ions.

Antibacterial activity

Whether or not porous Ta has antibacterial properties is still controversial. Studies conducted by Zhang and colleagues[50, 51] revealed that a TaN coating exhibited excellent anti-bacterial properties against various types of bacteria, such as Staphylococcus aureus and Porphyromonas gingivalis. In another study, the use of Ta-based components in 966 patients who had undergone total hip arthroplasty significantly decreased the likelihood of infection.[52] Compared to Ti, the infection rate of Ta was lower at 3.1%. This suggests that it confers some resistance against infection.

The porous nature of Ta materials and their rough surfaces are helpful for tissue growth and early implant durability, but they also create favourable circumstances for bacterial colonisation.[53] In *in vivo* environments, porous Ta prostheses demonstrated adequate osseointegration ability even when the implanted site was in a long-term infected state, but 3D-printed Ta failed to demonstrate intrinsic anti-biofilm qualities *in vitro*.[54, 55] According to a study by Yang et al.,[56] this could be the outcome of the host immunological reaction brought on by porous Ta. Other research has yielded inconclusive results regarding the capacity of porous Ta to fend off infection *in vivo*.[57] There is still much disagreement in academia as to whether Ta has intrinsic antibacterial properties.

Preclinical Experiments using Tantalum

Many scholars have verified the osseointegration and osteogenic characteristics of porous Ta scaffolds *in vivo* through animal experiments. As mentioned above, porous Ta implants with open, interconnected structures are beneficial for osteoblast adhesion and proliferation as well as the passage of nutrients and oxygen needed for the formation of new bone. The oxygen concentration and acidic conditions of porous Ta scaffold were verified by Jonitz et al.[47] to be advantageous for bone ingrowth. At 16 weeks after surgery, Wang et al.[58] completed 3D reconstruction of micro-computed tomography scans and estimated the quantity percentage of bone formed around porous Ta implants in rabbits with condylar osteochondral defects. They indicated that the interior of the porous Ta implant as well as its surface had been penetrated by freshly-formed bone. The right hind legs of rabbits were surgically implanted with porous 3D-printed Ta and Ti_6Al_4V implants by Guo et al.[14] Radiographs taken at 4, 8, and 12 weeks, shown in **Figure 4A**, revealed that porous Ta specimens integrated into the surrounding bone tissue more successfully than porous Ti_6Al_4V specimens and prevented loosening or dislocation.[14] Wauthle et al.[18] conducted histological evaluation of a porous Ta implant removed from a rat femoral defect and found that the pores of the implant supported strong new bone growth, and the porous Ta scaffold was successfully incorporated into the surrounding tissue (**Figure 4B**). In conclusion, the superior osseointegration and osteoconductivity of porous Ta facilitated bone tissue remodelling and regeneration.

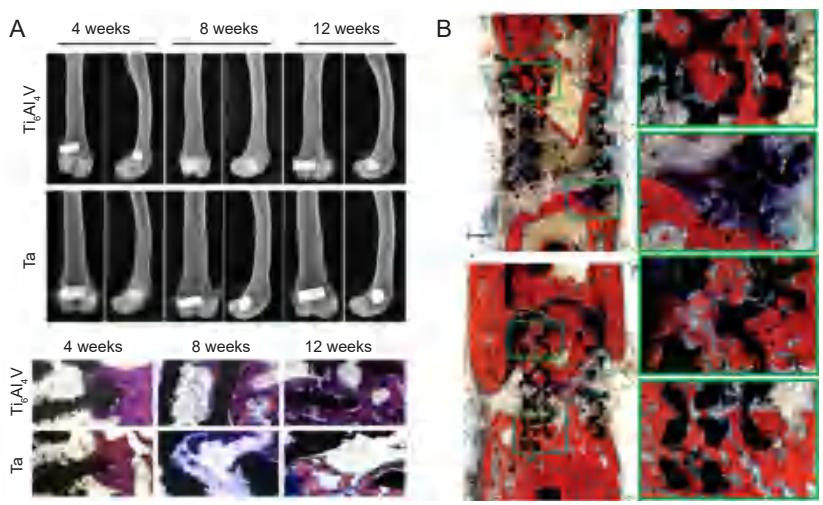

Figure 4. Osseointegration of porous tantalum (Ta) scaffolds. (A) Radiographic and histological images of porous Ta and Ti_6Al_4V implants at 4, 8, and 12 weeks. Reprinted from Guo et al.[14] (B) Histological images of SLM porous Ta after 12 weeks *in vivo*. Reprinted from Wauthle et al.[18] Copyright © 2014 Acta Materialia Inc.

The term "osseointegration" refers to the process in which an implant is enveloped by surrounding bone tissue or comes into contact directly with it. Porous Ta scaffolds have solid osseointegration after implantation, good *in vitro* biocompatibility, and no early, evident allergic reactions.[59] In the right hind leg of rabbits, Guo et al.[14] implanted porous Ta and Ti_6Al_4V implants. Radiographs taken at 4, 8, and 12 weeks revealed that the porous Ta samples prevented loosening or dislocation more successfully than the porous Ti_6Al_4V samples. Wang et al.[60] used micro-computed tomography analysis to evaluate the volume of new bone around porous Ta implants and compared them with porous Ti implants at 6

and 12 weeks. They discovered that the volume of new bone around the porous Ta implants was much greater than that surrounding the porous Ti implants.[60] Porous Ta rods were inserted into the hind legs of dogs by Wei et al.[61] and evaluated by a hard tissue biopsy 3 to 6 weeks after implantation. They found that new osteoblast adhesion and new bone ingrowth were seen at the Ta-host bone contact area and the pores. Three and six months after implantation, the Ta rod from a canine femoral shaft defect model was analysed by Van Gieson staining by Wang et al.[15] The study revealed that the bonding strength between the 3D-printed Ta and the host bone was significantly greater after 6 months, and examination of hard tissue sections demonstrated that the new bone was firmly bonded to the surface of the Ta implant. In a rabbit tibial repair model, Fraser et al. implanted Ti implants at the neck and root tip together with a mid-connected implant constructed of porous Ta.[62] They observed that new bone growth occurred more frequently around the middle of the implant than at the neck and tip of the root because of the greater interaction with the surrounding soft and hard tissues.

The potential of porous Ta in bone functional regeneration is demonstrated by the abundance of blood vessels that emerge at the interface and inside the prosthesis as new bone tissue grows into the implant. After 4, 8, and 16 weeks of healing, Hacking et al.[63] removed subcutaneous porous Ta implants from the backs of dogs and used transmission light microscopy to examine their histological sections. The porous Ta stent was discovered to include a significant proportion of vascularised connective fibrous tissue 16 weeks after placement. After removing porous Ta implants from dog femurs 52 weeks after they were implanted, Bobyn et al.[64] discovered identical histological evidence of vascular supply throughout the endophytic bone. These results confirmed that porous Ta promotes vasculogenesis, but the angiogenic mechanisms and factors affecting angiogenesis in porous Ta scaffolds have not been clarified.

Drug Delivery of Porous Tantalum

In the past few years, the use of porous structures to deliver drugs has become a research hotspot. Porous Ta metal has become one of the best choices for drug-loaded scaffolds due to its good biocompatibility. Surface modification by dip coating, hydrogel packaging, and spray coating are examples of drug-loading techniques. Multiple studies have shown that porous Ta metal itself has no observable antibacterial effect *in vitro*.[53, 65] However, porous Ta promotes innate immunity and antibacterial actions *in vivo*.[55] Carrying antibiotics to fight infection has become the main use of drug delivery. Functional reconstruction and adjuvant therapy after tumour resection are another use of porous Ta metallic materials for drug delivery. Guo et al.[66] used hydrogel and electrostatic interaction techniques to load doxorubicin onto 3D-printed porous Ta and showed that this technique successfully extended the duration of medication release. Some scholars further enhanced the osteogenic effect of Ta metal by drug loading. For repairing bone defects, Tanzer et al.[67] used 3D-printed porous Ta and surgically implanted a porous Ta stent carrying zoledronic acid into the proximal femurs of dogs. Compared to a blank control group, the bone mass around the prosthesis was 2.34 times greater in the experimental group than the control group, and bone growth was 58% higher. In addition, other studies using implants loaded with vascular endothelial growth factor or transforming growth factor have verified the increased repair ability after drug loading.[68, 69] High local drug concentration, long release duration, and low toxicity are all benefits of the porous Ta metal drug delivery system; however clinical transformation application and drug dosage optimization still need to be improved.[70] **Figure 5** shows different methods of loading cells or medications onto porous Ta.

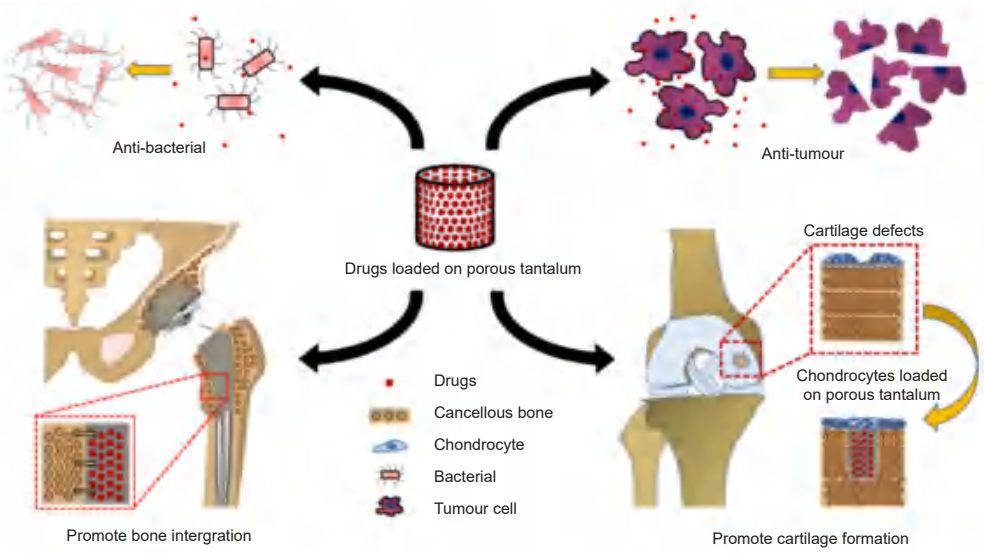

Figure 5. Drugs or cells loaded onto porous tantalum (Ta) for different treatments. Copyright 2021 from Hua et al.[70] Reproduced by permission of Taylor and Francis Group, LLC, a division of Informapic.

Clinical Translation of Porous Tantalum

As mentioned above, porous Ta has excellent biological properties, an elastic modulus comparable to human cancellous bone, sufficient mechanical strength, and excellent corrosion resistance. Since Kaplan et al.[71] first developed Ta implants with an open cell structure in 1994, porous Ta metal implants are being used more frequently in orthopaedic procedures such as foot and ankle surgery, shoulder reconstruction, spinal fusion, and hip and knee replacement. The effectiveness and safety of 3D-printed Ta implants have been the subject of an increasing number of clinical trials. **Figure 6** shows several instances of 3D-printed porous Ta implants applied in orthopaedic surgery.[72, 73]

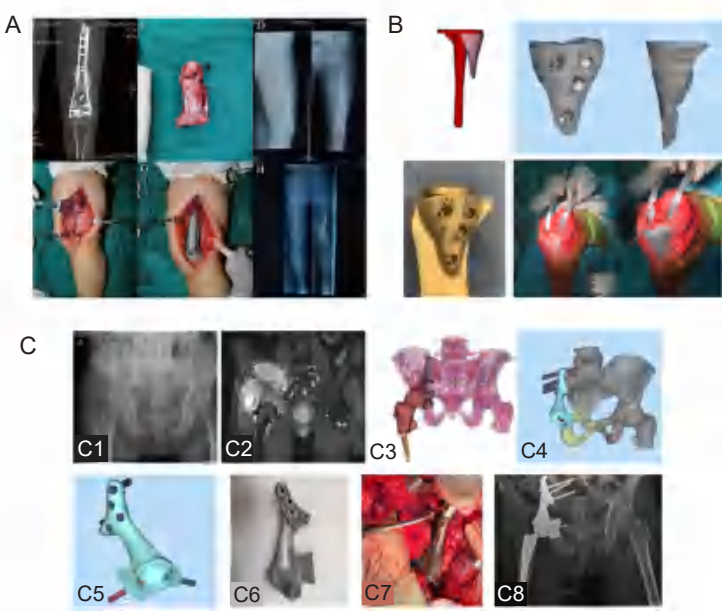

Figure 6. Clinical translation of 3D-printed porous Ta. (A) The clinical application of customized 3D-printed porous Ta scaffolds combined with Masquelet's induced membrane technique to reconstruct an infected segmental femoral defect. Reprinted from Wu et al.[72] (B) Knee reconstruction using 3D-printed porous Ta augmentation in the treatment of a Charcot joint. Reprinted from Hua et al.[73] (C) After pelvic tumour resection, hemi-pelvic replacement surgery was performed using 3D-printed porous Ta implants. (C1) Anteroposterior X-ray of the patient's hip joint showed an uneven density of the right iliac crest. (C2) Coronal MRI showed the extent of tumour invasion. (C3) Preoperative simulation of tumour resection and reconstruction range and location. (C4) Hemi-pelvic prosthesis design to restore the pelvic ring structure. (C5) Lateral view of the hemi-pelvic prosthesis. (C6) 3D-printed hemi-pelvic prosthesis. (C7) Intraoperative prosthesis implantation. (C8) X-ray at 6 months after surgery. C was from the authors' original study. 3D: three-dimensional; MRI: magnetic resonance imaging; Ta: tantalum.

Hip

At present, porous Ta implants are frequently used in three types of hip surgery: developmental dysplasia of the hip acetabular shelf, femoral head necrosis support, and hip reconstruction. Cheng et al.[74] reported a study on the application of individualised porous Ta metal acetabular shelf augments prepared by 3D-printing technology for hip joint reconstruction in the treatment of adult developmental dysplasia of the hip. Eight patients with Crowe type I developmental dysplasia of the hip were included in this study. Individual 3D-modelling of the hip joint was performed by computer. The most appropriate size of the acetabular shelf was designed using specialised software MIMICS (Materialise, Leuven, Belgium), and then the porous acetabular augment was processed. The visual analogue scale score decreased from 2.92 ± 0.79 preoperatively to 0.83 ± 0.72 at the last follow-up, and the Harris hip score increased from 69.67 ± 4.62 preoperatively to 84.25 ± 4.14 at the final follow-up. Imaging analysis revealed that the Ta metal acetabular augment was in tight contact with the iliac bone and exhibited no loosening or osteoarthritis progression, and the changes were statistically significant.

In the treatment of osteonecrosis of the femoral head (ONFH), a porous Ta rod plays the role of filling and supporting a femoral head with a bone defect after core decompression, and stimulating osteogenesis of the host bone in the subchondral bone area. Studies have shown that a porous Ta rod can slow the progress of early osteonecrosis and delay the time of joint replacement.[75, 76] Liu et al.[77] reported that 149 patients with early ONFH were treated with porous Ta rods, and the follow-up study after 3 years showed good clinical and imaging results. However, the long-term effect of Ta rods is controversial.[78] One study showed that the mechanical support of the necrotic area by porous Ta rods is insufficient, and only 1.9% of the bone ingraft was observed in histopathological examination of the 15 Ta rods removed.[79] Therefore, some scholars have tried to combine vascularised bone flap transplantation or BMSCs with porous Ta rods.[80, 81] To confirm the efficacy of

these techniques, long-term clinical follow-up surveillance is still required to evaluate these improvements.

The use of porous Ta material in total hip arthroplasty is mainly in the acetabular cup. In 2002, experts directly pressed polyethylene lining into a porous Ta cup, and this integrated design reduced wear of the polyethylene.[82] Wear debris has been considered as the main cause of aseptic loosening of the acetabular cup, so this design can theoretically prolong the service life of the artificial joint. In a clinically available prospective study, 151 hips were followed up for 8–10 years after primary total hip arthroplasty.[83] Although periacetabular spaces of 1 to 5 mm in length could be identified early in 25 hips, these disappeared after 24 weeks. No complications such as osteolysis or prosthesis loosening were confirmed by follow-up radiographs. On the surface of the porous Ta cup, there was significant bone ingrowth in a patient who underwent revision surgery due to dislocation 50 months after surgery. Eighty-two patients who underwent total hip replacement with a porous Ta acetabular component were observed by Macheras et al.[84] for an average of 7.3 years. At 6 months following surgery, the gap between the prosthesis and the surrounding bone was filled with new bone tissue, and at the latest follow-up, there were no radiolucent lines or indications of periprosthetic osteolysis.[84] For revision total hip arthroplasty, bone defect repair and acetabulum reconstruction, as well as restoration of basic stability, centre of rotation, and maximum bone–implant contact, are surgical challenges.[85] Several short-term and medium-term studies have shown that porous Ta acetabular cups and patches provide good results in the treatment of acetabular bone defects.[86, 87] Löchel et al.[88] performed a 10-year follow-up after hip revision surgery using a porous Ta cup and augment. The survival rate of 53 hips with complete follow-up was 92.5%. The Harris hip score increased significantly after revision surgery.

Knee

Porous Ta materials are also frequently used in knee reconstruction surgery. In short-term and long-term postoperative follow-up studies, the replacement of a conventional prosthesis with a cementless porous Ta single-piece tibial prosthesis achieved good clinical results.[89-91] De Martino et al.[92] described results in 33 patients who underwent primary total knee arthroplasty (TKA) with a cementless Ta single tibial component in a study with postoperative follow-up of at least 10 years. None of the prostheses were subjected to radiological examination for osteolysis, or displacement. The individuals' average knee scores increased from 56 before surgery to 93 afterward, showing that porous Ta is a promising alternative material for TKA prosthesis. The construction of this tibial monolithic component is comparable to that of the acetabular monolithic replacement in that polyethylene is directly compressed into the porous Ta substrate, eliminating the possibility of wear debris penetrating the bone–implant interface. The mechanical and biological characteristics of the porous Ta ensure the primary stability and long-term survival of the tibial component. Significant bone ingrowth was found in the column and posterior floor plate interface of a porous Ta tibial prosthesis that was recovered from a chronically-infected knee prosthesis through histological analysis, indicating that even in an infected environment, good bone-implant fusion can still be achieved.[93]

The treatment of bone defects in the distal femur, proximal tibia and even patella in knee reconstruction has always been one of the difficulties in surgery. Porous Ta grafts are used for structural transplantation and various irregular shapes can be designed and prepared to restore the required bone reserve depending on location and the amount of bone lost.[94] A number of medium-term follow-up studies have shown that porous Ta vertebrae have a good effect on restoring huge bone defects and maintaining the stability of prostheses, whether in the femoral or tibial sides.[95, 96] Another systematic review of Ta cones and cannulas revealed a 9.7% reoperation rate and a 0.8% sterile loosening rate per cannula. The reoperation rate of Ta vertebrae was 18.7%, and the aseptic loosening rate was 1.7%.[97] Patellar reconstruction with a porous Ta prosthesis is a way to restore the normal structure and function of the patellofemoral joint in cases of knee extension device dysfunction due to patellar resection or patellar bone defect. In a clinical study, Kamath et al.[98] investigated the use of a porous Ta patellar component to treat severe patellar loss during revision TKA. All 23 participants had positive clinical outcomes at the most recent follow-up (mean 7.7 years), as measured by the Oxford Knee Score and the Knee Society Score.[98]

Spine

Porous Ta scaffolds are commonly used in lumbar interbody fusion and cervical interbody fusion in spinal repair applications.[99] A porous Ta cage used in anterior cervical fusion was proven to be beneficial in a prospective randomized controlled clinical experiment by Fernández-Fairen et al.[100] The Ta cage implantation group revealed a similar fusion rate and postoperative stability at the conclusion of a 2-year follow-up period compared to the standard autogenous iliac bone transplant paired with an anterior wall plate. Patients who received single-hole Ta cage implantation for interbody fusion had good clinical and radiological outcomes after 11 years of follow-up, with no significant complications in 12 patients. In addition, Mastronardi et al.[101] showed that porous Ta was beneficial in terms of interbody fusion rate, low complication rate, and short- or long-term postoperative evaluation scores, such as 36-item short-form, neck disability index, and visual analogue scale. Lebhar et al.[102] also revealed the preliminary stability and osseointegration of Ta interbody implants in the medium-term follow-up of posterior lumbar interbody fusion, and the results confirmed that porous Ta implants are a reliable choice for spinal fusion surgery. Surgical time, blood loss, length of hospital stay, fusion rate, and visual analogue scale scores, and complication rates from pertinent clinical studies, were all examined in two recent meta-analyses. We discovered through two meta-analyses that porous Ta implants, which have been the gold standard in the surgical treatment of anterior cervical degenerative disc degeneration, are equally effective and safe.[37, 103]

Foot and ankle

End-stage ankle arthritis is a very serious disease. In the

case of ineffective conservative treatment, ankle arthrodesis and ankle replacement are two commonly-used surgical treatments.[104] Horisberger et al.[105] revealed the use of a Ta spacer to reconstruct major ankle bone defects during ankle arthrodesis. Postoperative X-rays confirmed that the structure had good initial stability.[105] Five years after surgery, Tiusanen et al.[106] reported 104 patients who had undergone total ankle replacement with a porous Ta prosthesis. Low rates of osteolysis and prosthesis loosening were found, and patient pain and functional outcomes were encouraging, indicating that Ta is an effective substitute for traditional bone grafting in foot and ankle applications.[106] Sundet et al.[107] used a combination of retrograde screws, a porous Ta spacer, and an osteoinductive augment with autologous bone marrow concentrate during revision surgery on 30 patients (31 ankles) who had undergone a failed total ankle replacement. The fusion rate was 93.5% after a mean follow-up of 23 months, and almost all patients were satisfied with the procedure, with pain relief and improved mobility. Although the survival rate of TKA has been shown to be lower than that of hip and knee replacement, some studies have recommended retaining the range of motion and normal gait of the ankle rather than using arthrodesis.[99, 108] The tibial and talar components of a porous Ta-based ankle prosthesis taken out of a 50-year-old female patient had a higher percentage of bone ingrowth than the porous Ta hip and knee components that were retrieved. At the same time, active bone remodelling was still visible in the porous Ta layer 3 years after operation.[109]

Others

In a case reported by Zhao et al.,[110] a 3D-printed porous Ta plate was used to treat tibial fracture nonunion, and the patient was able to perform normal activities 10 weeks after surgery without pain in the affected limb. The fracture had fully healed at the 5-month follow-up, and the patient was able to return to work and normal activities.[110] In order to manage challenging proximal humeral fractures, Li et al.[111] observed 51 patients who had undergone total shoulder arthroplasty utilizing a porous Ta prosthesis. After an average follow-up period of 3 years, radiographic evaluation showed anatomical union of the greater tuberosity of the shoulder in 92% of enrolled patients, and there was no evidence of an infection or of prosthesis loosening. Using monoblock porous Ta glenoid components, Chen et al. revealed good clinical results in patients with no loosening of the glenoid component or need for revision surgery regardless of preoperative glenoid morphology.[112] Sasanuma et al.[113] also demonstrated that in elderly patients with chronic comminuted proximal humeral fractures, the reverse shoulder arthroplasty group using porous Ta implants had a higher rate of bone healing and a greater range of shoulder motion than the group using nonporous stents.

Summary

Recently, porous Ta metal has attracted more attention as a new orthopaedic implant material. With the deepening of research and the progress of technology, the advantages of porous Ta metal materials in mechanics and biology have been gradually highlighted. The use of Ta is not limited to orthopaedic equipment such as porous Ta rods and intervertebral fusion cages, but it has also been applied to complex implants such as artificial hip and knee prostheses. Three-dimensional printing technology has the advantages of sufficient design freedom and personalised customisation when dealing with the complex morphology of human body structure. It is easier to load different medications onto the porous surface of the material, but it is challenging to maintain the biological activity and regulate the kinetics of its delayed release. However, its clinical application still faces problems such as high cost, a complex preparation process, and inadequately slow osseointegration. *In vivo* safety also needs to be supported by more research evidence. In addition, the mechanism of action involved in the biological effects of Ta metals requires more comprehensive and in-depth exploration, including the development of proteomics and genomics. It is necessary for researchers from materials science, biology, medicine and other disciplines to cooperate. Future studies will focus on porous Ta metal materials with easy preparation processes, low costs, and superior performance.

There are some limitations in this review. Publication bias was assessed but could not be ruled out. In addition not all clinically-pertinent topics can be addressed by this analysis, and some of the results may be challenging to put into practice. However, the authors provided an innovative viewpoint on how to introduce Ta into bone repair materials using advances in AM technology. We hope that this review will provide a succinct explanation of the potential of Ta as a bone implant material in the near future.

Author contributions
Conceptualization: DZ, JY; definition of intellectual content: LC, JL; literature search: HY, PY, HW, LL; manuscript preparation and editing: JY, HY, LS, BW; manuscript review: DZ. All authors approved the final version of the manuscript.
Financial support
This work was supported by the General Program of the National Natural Science Foundation of China, No. 82172398.
Acknowledgement
None.
Conflicts of interest statement
The authors declare that they have no known competing financial interests or personal relationships that could have appeared to influence the work reported in this paper.

1. Li, J. J.; Ebied, M.; Xu, J.; Zreiqat, H. Current approaches to bone tissue engineering: the interface between biology and engineering. *Adv Healthc Mater.* **2018**, *7*, e1701061.
2. Ghassemi, T.; Shahroodi, A.; Ebrahimzadeh, M. H.; Mousavian, A.; Movaffagh, J.; Moradi, A. Current concepts in scaffolding for bone tissue engineering. *Arch Bone Jt Surg.* **2018**, **6**, 90-99.
3. Asri, R. I. M.; Harun, W. S. W.; Samykano, M.; Lah, N. A. C.; Ghani, S. A. C.; Tarlochan, F.; Raza, M. R. Corrosion and surface modification on biocompatible metals: A review. *Mater Sci Eng C Mater Biol Appl.* **2017**, *77*, 1261-1274.

4. Han, Q.; Wang, C.; Chen, H.; Zhao, X.; Wang, J. Porous tantalum and titanium in orthopedics: a review. *ACS Biomater Sci Eng.* **2019**, *5*, 5798-5824.
5. Cardonne, S. M.; Kumar, P.; Michaluk, C. A.; Schwartz, H. D. Tantalum and its alloys. *Int J Refract Met Hard Mater.* **1995**, *13*, 187-194.
6. Zhang, L.; Haddouti, E. M.; Beckert, H.; Biehl, R.; Pariyar, S.; Rüwald, J. M.; Li, X.; Jaenisch, M.; Burger, C.; Wirtz, D. C.; Kabir, K.; Schildberg, F. A. Investigation of cytotoxicity, oxidative stress, and inflammatory responses of tantalum nanoparticles in THP-1-derived macrophages. *Mediators Inflamm.* **2020**, *2020*, 3824593.
7. Boyan, B. D.; Lotz, E. M.; Schwartz, Z. * Roughness and hydrophilicity as osteogenic biomimetic surface properties. *Tissue Eng Part A.* **2017**, *23*, 1479-1489.
8. Chang, Y. Y.; Huang, H. L.; Chen, H. J.; Lai, C. H.; Wen, C. Y. Antibacterial properties and cytocompatibility of tantalum oxide coatings. *Surf Coat Technol.* **2014**, *259*, 193-198.
9. Gao, H.; Yang, J.; Jin, X.; Qu, X.; Zhang, F.; Zhang, D.; Chen, H.; Wei, H.; Zhang, S.; Jia, W.; Yue, B.; Li, X. Porous tantalum scaffolds: FABRICATION, structure, properties, and orthopedic applications. *Mater Des.* **2021**, *210*, 110095.
10. Wang, Z.; Wang, C.; Li, C.; Qin, Y.; Zhong, L.; Chen, B.; Li, Z.; Liu, H.; Chang, F.; Wang, J. Analysis of factors influencing bone ingrowth into three-dimensional printed porous metal scaffolds: a review. *J Alloys Compd.* **2017**, *717*, 271-285.
11. Biemond, J. E.; Aquarius, R.; Verdonschot, N.; Buma, P. Frictional and bone ingrowth properties of engineered surface topographies produced by electron beam technology. *Arch Orthop Trauma Surg.* **2011**, *131*, 711-718.
12. Markhoff, J.; Wieding, J.; Weissmann, V.; Pasold, J.; Jonitz-Heincke, A.; Bader, R. Influence of different three-dimensional open porous titanium scaffold designs on human osteoblasts behavior in static and dynamic cell investigations. *Materials (Basel).* **2015**, *8*, 5490-5507.
13. Wang, H.; Su, K.; Su, L.; Liang, P.; Ji, P.; Wang, C. Comparison of 3D-printed porous tantalum and titanium scaffolds on osteointegration and osteogenesis. *Mater Sci Eng C Mater Biol Appl.* **2019**, *104*, 109908.
14. Guo, Y.; Xie, K.; Jiang, W.; Wang, L.; Li, G.; Zhao, S.; Wu, W.; Hao, Y. In vitro and in vivo study of 3D-printed porous tantalum scaffolds for repairing bone defects. *ACS Biomater Sci Eng.* 2019, *5*, 1123-1133.
15. Wang, X.; Zhu, Z.; Xiao, H.; Luo, C.; Luo, X.; Lv, F.; Liao, J.; Huang, W. Three-dimensional, multiscale, and interconnected trabecular bone mimic porous tantalum scaffold for bone tissue engineering. *ACS Omega.* **2020**, *5*, 22520-22528.
16. Keaveny, T. M.; Morgan, E. F.; Niebur, G. L.; Yeh, O. C. Biomechanics of trabecular bone. *Annu Rev Biomed Eng.* **2001**, *3*, 307-333.
17. Karageorgiou, V.; Kaplan, D. Porosity of 3D biomaterial scaffolds and osteogenesis. *Biomaterials.* **2005**, *26*, 5474-5491.
18. Wauthle, R.; van der Stok, J.; Amin Yavari, S.; Van Humbeeck, J.; Kruth, J. P.; Zadpoor, A. A.; Weinans, H.; Mulier, M.; Schrooten, J. Additively manufactured porous tantalum implants. *Acta Biomater.* **2015**, *14*, 217-225.
19. Kamran, S.; Farid, A. Microstructure-tailored stainless steels with high mechanical performance at elevated temperature. In *Stainless Steels and Alloys*, Zoia, D., ed. IntechOpen: Rijeka, **2018**; p Ch. 7.
20. Azam, F. I.; Abdul Rani, A. M.; Altaf, K.; Rao, T. V. V. L. N.; Zaharin, H. A. An in-depth review on direct additive manufacturing of metals. *IOP Conf Ser Mater Sci Eng.* **2018**, *328*, 012005.
21. Liu, Y.; Bao, C.; Wismeijer, D.; Wu, G. The physicochemical/biological properties of porous tantalum and the potential surface modification techniques to improve its clinical application in dental implantology. *Mater Sci Eng C Mater Biol Appl.* **2015**, *49*, 323-329.
22. Yang, J.; Jin, X.; Gao, H.; Zhang, D.; Chen, H.; Zhang, S.; Li, X. Additive manufacturing of trabecular tantalum scaffolds by laser powder bed fusion: Mechanical property evaluation and porous structure characterization. *Mater Charact.* **2020**, *170*, 110694.
23. Zardiackas, L. D.; Parsell, D. E.; Dillon, L. D.; Mitchell, D. W.; Nunnery, L. A.; Poggie, R. Structure, metallurgy, and mechanical properties of a porous tantalum foam. *J Biomed Mater Res.* **2001**, *58*, 180-187.
24. Stiehl, J. B. Trabecular metal in hip reconstructive surgery. *Orthopedics.* **2005**, *28*, 662-670.
25. Yang, M.; Ma, H.; Shen, Z.; Huang, Z.; Tian, Q.; Tian, J. Dissimilar material welding of tantalum foil and Q235 steel plate using improved explosive welding technique. *Mater Des.* **2020**, *186*, 108348.
26. Qian, H.; Lei, T.; Lei, P.; Hu, Y. Additively manufactured tantalum implants for repairing bone defects: a systematic review. *Tissue Eng Part B Rev.* **2021**, *27*, 166-180.
27. Tang, H. P.; Yang, K.; Jia, L.; He, W. W.; Yang, L.; Zhang, X. Z. Tantalum bone implants printed by selective electron beam manufacturing (SEBM) and their clinical applications. *JOM.* **2020**, *72*, 1016-1021.
28. Chen, C.; Li, Y.; Zhang, M.; Wang, X.; Zhang, C.; Jing, H. Effect of laser processing parameters on mechanical properties of porous tantalum fabricated by laser multi-layer micro-cladding. *Rapid Prototyp J.* **2017**, *23*, 758-770.
29. Maccauro, G.; Iommetti, P. R.; Muratori, F.; Raffaelli, L.; Manicone, P. F.; Fabbriciani, C. An overview about biomedical applications of micron and nano size tantalum. *Recent Pat Biotechnol.* **2009**, *3*, 157-165.
30. Cheng, X.; Wan, Q.; Pei, X. Graphene family materials in bone tissue regeneration: perspectives and challenges. *Nanoscale Res Lett.* **2018**, *13*, 289.
31. Wei, X.; Zuo, X.; Yang, B. In Sequential recommendation based on long-term and short-term user behavior with self-attention, Knowledge Science, Engineering and Management, Cham, 2019// Douligeris, C.; Karagiannis, D.; Apostolou, D., eds. Springer International Publishing: Cham, **2019**; pp 72-83.
32. Balla, V. K.; Bodhak, S.; Bose, S.; Bandyopadhyay, A. Porous tantalum structures for bone implants: fabrication, mechanical and in vitro biological properties. *Acta Biomater.* **2010**, *6*, 3349-3359.
33. Dou, X.; Wei, X.; Liu, G.; Wang, S.; Lv, Y.; Li, J.; Ma, Z.; Zheng, G.; Wang, Y.; Hu, M.; Yu, W.; Zhao, D. Effect of porous tantalum on promoting the osteogenic differentiation of bone marrow mesenchymal stem cells in vitro through the MAPK/ERK signal pathway. *J Orthop Translat.* **2019**, *19*, 81-93.
34. Gee, E. C. A.; Eleotério, R.; Bowker, L. M.; Saithna, A.; Hunt, J. A. The influence of tantalum on human cell lineages important for healing in soft-tissue reattachment surgery: an in-vitro analysis. *J Exp Orthop.* **2019**, *6*, 40.
35. Lu, M.; Xu, S.; Lei, Z. X.; Lu, D.; Cao, W.; Huttula, M.; Hou, C. H.; Du, S. H.; Chen, W.; Dai, S. W.; Li, H. M.; Jin, D. D. Application of a novel porous tantalum implant in rabbit anterior lumbar spine fusion model: in vitro and in vivo experiments. *Chin Med J (Engl).* **2019**, *132*, 51-62.
36. Wei, X.; Liu, B.; Liu, G.; Yang, F.; Cao, F.; Dou, X.; Yu, W.; Wang, B.; Zheng, G.; Cheng, L.; Ma, Z.; Zhang, Y.; Yang, J.; Wang, Z.; Li, J.; Cui, D.; Wang, W.; Xie, H.; Li, L.; Zhang, F.; Lineaweaver, W. C.; Zhao, D. Mesenchymal stem cell-loaded porous tantalum integrated with biomimetic 3D collagen-based scaffold to repair large osteochondral

defects in goats. *Stem Cell Res Ther.* **2019**, *10*, 72.
37. Wang, Y.; Wei, R.; Subedi, D.; Jiang, H.; Yan, J.; Li, J. Tantalum fusion device in anterior cervical discectomy and fusion for treatment of cervical degeneration disease: a systematic review and meta-analysis. *Clin Spine Surg.* **2020**, *33*, 111-119.
38. Temponi, E. F.; Souza, P. E. A.; Souto, G. R.; Magalhães, L. M. D.; Dutra, W. O.; Gollob, K. J.; Silva, T. A.; Soares, R. V. Effect of porous tantalum on the biological response of human peripheral mononuclear cells exposed to Porphyromonas gingivalis. *J Investig Clin Dent.* **2019**, *10*, e12472.
39. Sagomonyants, K. B.; Hakim-Zargar, M.; Jhaveri, A.; Aronow, M. S.; Gronowicz, G. Porous tantalum stimulates the proliferation and osteogenesis of osteoblasts from elderly female patients. *J Orthop Res.* **2011**, *29*, 609-616.
40. Wang, Q.; Zhang, H.; Li, Q.; Ye, L.; Gan, H.; Liu, Y.; Wang, H.; Wang, Z. Biocompatibility and osteogenic properties of porous tantalum. *Exp Ther Med.* **2015**, *9*, 780-786.
41. Jonitz, A.; Lochner, K.; Lindner, T.; Hansmann, D.; Marrot, A.; Bader, R. Oxygen consumption, acidification and migration capacity of human primary osteoblasts within a three-dimensional tantalum scaffold. *J Mater Sci Mater Med.* **2011**, *22*, 2089-2095.
42. Wang, F.; Li, C.; Zhang, S.; Liu, H. Tantalum coated on titanium dioxide nanotubes by plasma spraying enhances cytocompatibility for dental implants. *Surf Coat Technol.* **2020**, *382*, 125161.
43. Qian, H.; Lei, T.; Ye, Z.; Hu, Y.; Lei, P. From the performance to the essence: the biological mechanisms of how tantalum contributes to osteogenesis. *Biomed Res Int.* **2020**, *2020*, 5162524.
44. Wang, X.; Ning, B.; Pei, X. Tantalum and its derivatives in orthopedic and dental implants: Osteogenesis and antibacterial properties. *Colloids Surf B Biointerfaces.* **2021**, *208*, 112055.
45. Horandghadim, N.; Khalil-Allafi, J.; Urgen, M. Effect of Ta(2) O(5) content on the osseointegration and cytotoxicity behaviors in hydroxyapatite-Ta(2)O(5) coatings applied by EPD on superelastic NiTi alloys. *Mater Sci Eng C Mater Biol Appl.* **2019**, *102*, 683-695.
46. Mei, S.; Yang, L.; Pan, Y.; Wang, D.; Wang, X.; Tang, T.; Wei, J. Influences of tantalum pentoxide and surface coarsening on surface roughness, hydrophilicity, surface energy, protein adsorption and cell responses to PEEK based biocomposite. *Colloids Surf B Biointerfaces.* **2019**, *174*, 207-215.
47. Li, R.; Liu, G.; Yang, L.; Qing, Y.; Tang, X.; Guo, D.; Zhang, K.; Qin, Y. Tantalum boride as a biocompatible coating to improve osteogenesis of the bionano interface. *J Biomed Mater Res A.* **2020**, *108*, 1726-1735.
48. Rouwkema, J.; Rivron, N. C.; van Blitterswijk, C. A. Vascularization in tissue engineering. *Trends Biotechnol.* **2008**, *26*, 434-441.
49. Cheng, S.; Ke, J.; Yao, M.; Shao, H.; Zhou, J.; Wang, M.; Ji, X.; Zhong, G.; Peng, F.; Ma, L.; Zhang, Y. Improved osteointegration and angiogenesis of strontium-incorporated 3D-printed tantalum scaffold via bioinspired polydopamine coating. *J Mater Sci Technol.* **2021**, *69*, 106-118.
50. Zhang, Y.; Zheng, Y.; Li, Y.; Wang, L.; Bai, Y.; Zhao, Q.; Xiong, X.; Cheng, Y.; Tang, Z.; Deng, Y.; Wei, S. Tantalum nitride-decorated titanium with enhanced resistance to microbiologically induced corrosion and mechanical property for dental application. *PLoS One.* **2015**, *10*, e0130774.
51. Zhu, Y.; Gu, Y.; Qiao, S.; Zhou, L.; Shi, J.; Lai, H. Bacterial and mammalian cells adhesion to tantalum-decorated micro-/nano-structured titanium. *J Biomed Mater Res A.* **2017**, *105*, 871-878.
52. Tokarski, A. T.; Novack, T. A.; Parvizi, J. Is tantalum protective against infection in revision total hip arthroplasty? *Bone Joint J.* **2015**, 97-B, 45-49.
53. Subramani, K.; Jung, R. E.; Molenberg, A.; Hammerle, C. H. Biofilm on dental implants: a review of the literature. *Int J Oral Maxillofac Implants.* **2009**, *24*, 616-626.
54. Harrison, P. L.; Harrison, T.; Stockley, I.; Smith, T. J. Does tantalum exhibit any intrinsic antimicrobial or antibiofilm properties? *Bone Joint J.* **2017**, 99-B, 1153-1156.
55. Wahl, P.; Sprecher, C. M.; Brüning, C.; Meier, C.; Milz, S.; Gautier, E.; Fintan Moriarty, T. Successful bony integration of a porous tantalum implant despite longlasting and ongoing infection: Histologic workup of an explanted shoulder prosthesis. *J Biomed Mater Res B Appl Biomater.* **2018**, *106*, 2924-2931.
56. Yang, C.; Li, J.; Zhu, C.; Zhang, Q.; Yu, J.; Wang, J.; Wang, Q.; Tang, J.; Zhou, H.; Shen, H. Advanced antibacterial activity of biocompatible tantalum nanofilm via enhanced local innate immunity. *Acta Biomater.* **2019**, *89*, 403-418.
57. Matharu, G. S.; Judge, A.; Murray, D. W.; Pandit, H. G. Do Trabecular metal acetabular components reduce the risk of rerevision after revision THA performed for periprosthetic joint infection? A study using the NJR data set. *Clin Orthop Relat Res.* **2019**, *477*, 1382-1389.
58. Wang, Q.; Zhang, H.; Gan, H.; Wang, H.; Li, Q.; Wang, Z. Application of combined porous tantalum scaffolds loaded with bone morphogenetic protein 7 to repair of osteochondral defect in rabbits. *Int Orthop.* **2018**, *42*, 1437-1448.
59. Bandyopadhyay, A.; Mitra, I.; Shivaram, A.; Dasgupta, N.; Bose, S. Direct comparison of additively manufactured porous titanium and tantalum implants towards in vivo osseointegration. *Addit Manuf.* **2019**, *28*, 259-266.
60. Wang, Q.; Qiao, Y.; Cheng, M.; Jiang, G.; He, G.; Chen, Y.; Zhang, X.; Liu, X. Tantalum implanted entangled porous titanium promotes surface osseointegration and bone ingrowth. *Sci Rep.* **2016**, *6*, 26248.
61. Wei, X.; Zhao, D.; Wang, B.; Wang, W.; Kang, K.; Xie, H.; Liu, B.; Zhang, X.; Zhang, J.; Yang, Z. Tantalum coating of porous carbon scaffold supplemented with autologous bone marrow stromal stem cells for bone regeneration in vitro and in vivo. *Exp Biol Med (Maywood).* **2016**, *241*, 592-602.
62. Fraser, D.; Mendonca, G.; Sartori, E.; Funkenbusch, P.; Ercoli, C.; Meirelles, L. Bone response to porous tantalum implants in a gap-healing model. *Clin Oral Implants Res.* **2019**, *30*, 156-168.
63. Hacking, S. A.; Bobyn, J. D.; Toh, K.; Tanzer, M.; Krygier, J. J. Fibrous tissue ingrowth and attachment to porous tantalum. *J Biomed Mater Res.* **2000**, *52*, 631-638.
64. Bobyn, J. D.; Stackpool, G. J.; Hacking, S. A.; Tanzer, M.; Krygier, J. J. Characteristics of bone ingrowth and interface mechanics of a new porous tantalum biomaterial. *J Bone Joint Surg Br.* **1999**, *81*, 907-914.
65. Sautet, P.; Parratte, S.; Mékidèche, T.; Abdel, M. P.; Flécher, X.; Argenson, J. N.; Ollivier, M. Antibiotic-loaded tantalum may serve as an antimicrobial delivery agent. *Bone Joint J.* **2019**, 101-B, 848-851.
66. Guo, X.; Chen, M.; Feng, W.; Liang, J.; Zhao, H.; Tian, L.; Chao, H.; Zou, X. Electrostatic self-assembly of multilayer copolymeric membranes on the surface of porous tantalum implants for sustained release of doxorubicin. *Int J Nanomedicine.* **2011**, *6*, 3057-3064.
67. Tanzer, M.; Karabasz, D.; Krygier, J. J.; Cohen, R.; Bobyn, J. D. The Otto Aufranc Award: bone augmentation around and within porous implants by local bisphosphonate elution. *Clin Orthop Relat Res.* **2005**, *441*, 30-39.
68. Zhou, R.; Xu, W.; Chen, F.; Qi, C.; Lu, B. Q.; Zhang, H.; Wu, J.;

Qian, Q. R.; Zhu, Y. J. Amorphous calcium phosphate nanospheres/polylactide composite coated tantalum scaffold: facile preparation, fast biomineralization and subchondral bone defect repair application. *Colloids Surf B Biointerfaces.* **2014**, *123*, 236-245.

69. Mrosek, E. H.; Schagemann, J. C.; Chung, H. W.; Fitzsimmons, J. S.; Yaszemski, M. J.; Mardones, R. M.; O'Driscoll, S. W.; Reinholz, G. G. Porous tantalum and poly-epsilon-caprolactone biocomposites for osteochondral defect repair: preliminary studies in rabbits. *J Orthop Res.* **2010**, *28*, 141-148.
70. Hua, L.; Lei, T.; Qian, H.; Zhang, Y.; Hu, Y.; Lei, P. 3D-printed porous tantalum: recent application in various drug delivery systems to repair hard tissue defects. *Expert Opin Drug Deliv.* **2021**, *18*, 625-634.
71. Rodeo, S. A.; Delos, D.; Weber, A.; Ju, X.; Cunningham, M. E.; Fortier, L.; Maher, S. What's new in orthopaedic research. *J Bone Joint Surg Am.* **2010**, *92*, 2491-2501.
72. Wu, Y.; Shi, X.; Zi, S.; Li, M.; Chen, S.; Zhang, C.; Xu, Y. The clinical application of customized 3D-printed porous tantalum scaffolds combined with Masquelet's induced membrane technique to reconstruct infective segmental femoral defect. *J Orthop Surg Res.* **2022**, *17*, 479.
73. Hua, L.; Lei, P.; Hu, Y. Knee Reconstruction Using 3D-Printed Porous Tantalum Augment in the Treatment of Charcot Joint. *Orthop Surg.* **2022**, *14*, 3125-3128.
74. Cheng, L.; Zhao, D.; Yang, L.; Li, J.; Ma, Z.; Wang, Z.; Tian, F.; Tian, S. The application of 3D printed customized porous tantalum acetabular patch for adult DDH hip reconstruction. *Zhonghua Guke Zazhi.* **2018**, *38*, 650-657.
75. Veillette, C. J.; Mehdian, H.; Schemitsch, E. H.; McKee, M. D. Survivorship analysis and radiographic outcome following tantalum rod insertion for osteonecrosis of the femoral head. *J Bone Joint Surg Am.* **2006**, *88 Suppl 3*, 48-55.
76. Liu, G.; Wang, J.; Yang, S.; Xu, W.; Ye, S.; Xia, T. Effect of a porous tantalum rod on early and intermediate stages of necrosis of the femoral head. *Biomed Mater.* **2010**, *5*, 065003.
77. Liu, Z. H.; Guo, W. S.; Li, Z. R.; Cheng, L. M.; Zhang, Q. D.; Yue, D. B.; Shi, Z. C.; Wang, B. L.; Sun, W.; Zhang, N. F. Porous tantalum rods for treating osteonecrosis of the femoral head. *Genet Mol Res.* **2014**, *13*, 8342-8352.
78. Zhang, X.; Wang, J.; Xiao, J.; Shi, Z. Early failures of porous tantalum osteonecrosis implants: a case series with retrieval analysis. *Int Orthop.* **2016**, *40*, 1827-1834.
79. Tanzer, M.; Bobyn, J. D.; Krygier, J. J.; Karabasz, D. Histopathologic retrieval analysis of clinically failed porous tantalum osteonecrosis implants. *J Bone Joint Surg Am.* **2008**, *90*, 1282-1289.
80. Zhao, D.; Zhang, Y.; Wang, W.; Liu, Y.; Li, Z.; Wang, B.; Yu, X. Tantalum rod implantation and vascularized iliac grafting for osteonecrosis of the femoral head. *Orthopedics.* **2013**, *36*, 789-795.
81. Zhao, D.; Liu, B.; Wang, B.; Yang, L.; Xie, H.; Huang, S.; Zhang, Y.; Wei, X. Autologous bone marrow mesenchymal stem cells associated with tantalum rod implantation and vascularized iliac grafting for the treatment of end-stage osteonecrosis of the femoral head. *Biomed Res Int.* **2015**, *2015*, 240506.
82. Sculco, T. P. The acetabular component: an elliptical monoblock alternative. *J Arthroplasty.* **2002**, *17*, 118-120.
83. Macheras, G.; Kateros, K.; Kostakos, A.; Koutsostathis, S.; Danomaras, D.; Papagelopoulos, P. J. Eight- to ten-year clinical and radiographic outcome of a porous tantalum monoblock acetabular component. *J Arthroplasty.* **2009**, *24*, 705-709.
84. Macheras, G. A.; Papagelopoulos, P. J.; Kateros, K.; Kostakos, A. T.; Baltas, D.; Karachalios, T. S. Radiological evaluation of the metal-bone interface of a porous tantalum monoblock acetabular component. *J Bone Joint Surg Br.* **2006**, *88*, 304-309.
85. Garbuz, D. S. Revision total hip: a novel modular cementless acetabular system for reconstruction of severe acetabular bone loss. *Oper Tech Orthop.* **2004**, *14*, 117-120.
86. Sporer, S. M.; Paprosky, W. G. The use of a trabecular metal acetabular component and trabecular metal augment for severe acetabular defects. *J Arthroplasty.* **2006**, *21*, 83-86.
87. Malkani, A. L.; Price, M. R.; Crawford, C. H., 3rd; Baker, D. L. Acetabular component revision using a porous tantalum biomaterial: a case series. *J Arthroplasty.* **2009**, *24*, 1068-1073.
88. Löchel, J.; Janz, V.; Hipfl, C.; Perka, C.; Wassilew, G. I. Reconstruction of acetabular defects with porous tantalum shells and augments in revision total hip arthroplasty at ten-year follow-up. *Bone Joint J.* **2019**, *101-b*, 311-316.
89. Hu, B.; Chen, Y.; Zhu, H.; Wu, H.; Yan, S. Cementless porous tantalum monoblock tibia vs cemented modular tibia in primary total knee arthroplasty: a meta-analysis. *J Arthroplasty.* **2017**, *32*, 666-674.
90. Hayakawa, K.; Date, H.; Tsujimura, S.; Nojiri, S.; Yamada, H.; Nakagawa, K. Mid-term results of total knee arthroplasty with a porous tantalum monoblock tibial component. *Knee.* **2014**, *21*, 199-203.
91. Wang, F.; Chen, H.; Yang, P.; Muheremu, A.; He, P.; Fan, H.; Yang, L. Three-dimensional printed porous tantalum prosthesis for treating inflammation after total knee arthroplasty in one-stage surgery - a case report. *J Int Med Res.* **2020**, *48*, 300060519891280.
92. De Martino, I.; D'Apolito, R.; Sculco, P. K.; Poultsides, L. A.; Gasparini, G. Total knee arthroplasty using cementless porous tantalum monoblock tibial component: a minimum 10-year follow-up. *J Arthroplasty.* **2016**, *31*, 2193-2198.
93. Sambaziotis, C.; Lovy, A. J.; Koller, K. E.; Bloebaum, R. D.; Hirsh, D. M.; Kim, S. J. Histologic retrieval analysis of a porous tantalum metal implant in an infected primary total knee arthroplasty. *J Arthroplasty.* **2012**, *27*, 1413.e5-9.
94. Levine, B.; Sporer, S.; Della Valle, C. J.; Jacobs, J. J.; Paprosky, W. Porous tantalum in reconstructive surgery of the knee: a review. *J Knee Surg.* **2007**, *20*, 185-194.
95. Potter, G. D., 3rd; Abdel, M. P.; Lewallen, D. G.; Hanssen, A. D. Midterm results of porous tantalum femoral cones in revision total knee arthroplasty. *J Bone Joint Surg Am.* **2016**, *98*, 1286-1291.
96. Kamath, A. F.; Lewallen, D. G.; Hanssen, A. D. Porous tantalum metaphyseal cones for severe tibial bone loss in revision knee arthroplasty: a five to nine-year follow-up. *J Bone Joint Surg Am.* **2015**, *97*, 216-223.
97. Rodríguez-Merchán, E. C.; Gómez-Cardero, P.; Encinas-Ullán, C. A. Management of bone loss in revision total knee arthroplasty: therapeutic options and results. *EFORT Open Rev.* **2021**, *6*, 1073-1086.
98. Kamath, A. F.; Gee, A. O.; Nelson, C. L.; Garino, J. P.; Lotke, P. A.; Lee, G. C. Porous tantalum patellar components in revision total knee arthroplasty minimum 5-year follow-up. *J Arthroplasty.* **2012**, *27*, 82-87.
99. Hanc, M.; Fokter, S. K.; Vogrin, M.; Molicnik, A.; Recnik, G. Porous tantalum in spinal surgery: an overview. *Eur J Orthop Surg Traumatol.* **2016**, *26*, 1-7.
100. Fernández-Fairen, M.; Alvarado, E.; Torres, A. Eleven-year follow-up of two cohorts of patients comparing stand-alone porous tantalum cage versus autologous bone graft and plating in anterior cervical fusions. *World Neurosurg.* **2019**, *122*, e156-e167.

101. Mastronardi, L.; Roperto, R.; Cacciotti, G.; Calvosa, F. Anterior cervical fusion with stand-alone trabecular metal cages to treat cervical myelopathy caused by degenerative disk disease. observations in 88 cases with minimum 12-month follow-up. *J Neurol Surg A Cent Eur Neurosurg.* **2018**, *79*, 496-501.
102. Lebhar, J.; Kriegel, P.; Chatellier, P.; Breton, Y.; Ropars, M.; Huten, D. Tantalum implants for posterior lumbar interbody fusion: a safe method at medium-term follow-up? *Orthop Traumatol Surg Res.* **2020**, *106*, 269-274.
103. Li, N.; Hu, W. Q.; Xin, W. Q.; Li, Q. F.; Tian, P. Comparison between porous tantalum metal implants and autograft in anterior cervical discectomy and fusion: a meta-analysis. *J Comp Eff Res.* **2019**, *8*, 511-521.
104. Adukia, V.; Mangwani, J.; Issac, R.; Hussain, S.; Parker, L. Current concepts in the management of ankle arthritis. *J Clin Orthop Trauma.* **2020**, *11*, 388-398.
105. Horisberger, M.; Paul, J.; Wiewiorski, M.; Henninger, H. B.; Khalifa, M. S.; Barg, A.; Valderrabano, V. Commercially available trabecular metal ankle interpositional spacer for tibiotalocalcaneal arthrodesis secondary to severe bone loss of the ankle. *J Foot Ankle Surg.* **2014**, *53*, 383-387.
106. Tiusanen, H.; Kormi, S.; Kohonen, I.; Saltychev, M. Results of trabecular-metal total ankle arthroplasties with transfibular approach. *Foot Ankle Int.* **2020**, *41*, 411-418.
107. Sundet, M.; Johnsen, E.; Eikvar, K. H.; Eriksen, M. L. Retrograde nailing, trabecular metal implant and use of bone marrow aspirate concentrate after failed ankle joint replacement. *Foot Ankle Surg.* **2021**, *27*, 123-128.
108. Onggo, J. R.; Nambiar, M.; Phan, K.; Hickey, B.; Galvin, M.; Bedi, H. Outcome after total ankle arthroplasty with a minimum of five years follow-up: a systematic review and meta-analysis. *Foot Ankle Surg.* **2020**, *26*, 556-563.
109. Epperson, R. T.; Barg, A.; Williams, D. L.; Saltzman, C. L. Histological analysis of a retrieved porous tantalum total ankle replacement: a case report. *JBJS Case Connect.* **2020**, *10*, e0379.
110. Zhao, D. W.; Ma, Z. J.; Wang, T. N.; Liu, B. Y. Biocompatible porous tantalum metal plates in the treatment of tibial fracture. *Orthop Surg.* **2019**, *11*, 325-329.
111. Li, F.; Jiang, C. Trabecular metal shoulder prosthesis in the treatment of complex proximal humeral fractures. *Int Orthop.* **2013**, *37*, 2259-2264.
112. Chen, R. E.; Mannava, S.; Miller, R. J.; Voloshin, I. Comparison of mid-term outcomes of total shoulder arthroplasty for B2 and A glenoids treated with trabecular metal glenoid components. *Semin Arthroplasty.* **2020**, *30*, 326-332.
113. Sasanuma, H.; Iijima, Y.; Saito, T.; Kanaya, Y.; Yano, Y.; Fukushima, T.; Nakama, S.; Takeshita, K. Clinical results of reverse shoulder arthroplasty for comminuted proximal humerus fractures in elderly patients: a comparison between nonporous stems versus trabecular metal stems. *JSES Int.* **2020**, *4*, 952-958.

Received: November 16, 2022
Revised: August 3, 2023
Accepted: August 30, 2023
Available online: September 28, 2023

A comparative study of human and porcine-derived decellularised nerve matrices

Rui Li[1,2], Shuai Qiu[3], Weihong Yang[2,4], Zilong Rao[1], Jiaxin Chen[1], Yuexiong Yang[4], Qingtang Zhu[3,], Xiaolin Liu[3], Ying Bai[1,*], Daping Quan[1,*]*

Key Words:
allogeneic; decellularised nerve matrix; immune response; xenogeneic; α-Gal

From the Contents

ABSTRACT

Decellularised extracellular matrix (dECM) biomaterials originating from allogeneic and xenogeneic tissues have been broadly studied in the field of regenerative medicine and have already been used in clinical treatments. Allogeneic dECMs are considered more compatible, but they have the drawback of extremely limited human tissue sources. Their availability is also restricted by the health and age of the donors. To investigate the viability of xenogeneic tissues as a substitute for human tissues, we fabricated both porcine decellularised nerve matrix (pDNM) and human decellularised nerve matrix for a comprehensive comparison. Photomicrographs showed that both dECM scaffolds retained the ECM microstructures of native human nerve tissues. Proteomic analysis demonstrated that the protein compositions of both dECMs were also very similar to each other. Their functional ECM contents effectively promoted the proliferation, migration, and maturation of primary human Schwann cells in vitro. However, pDNM contained a few antigens that induced severe host immune responses in humanised mice. Interestingly, after removing the α-galactosidase antigen, the immune responses were highly alleviated and the pre-treated pDNM maintained a human decellularised nerve matrix-like pro-regenerative phenotype. Therefore, we believe that an α-galactosidase-free pDNM may serve as a viable substitute for human decellularised nerve matrix in future clinical applications.

***Corresponding authors:**
Qingtang Zhu,
Zhuqingt@mail.sysu.edu.cn;
Ying Bai,
baiy28@mail.sysu.edu.cn;
Daping Quan,
cesqdp@mail.sysu.edu.cn.

http://doi.org/10.12336/biomatertransl.2023.03.006

How to cite this article:
Li, R.; Qiu, S.; Yang, W.; Rao, Z.; Chen, J.; Yang, Y.; Zhu, Q.; Liu, X.; Bai, Y.; Quan. D. A comparative study of human and porcine-derived decellularised nerve matrices. *Biomater Transl.* **2023**, *4*(3), 180-195.

Introduction

The number of functional biomaterials composed of decellularised extracellular matrix (dECM) has been growing rapidly and they have drawn great attention regarding regenerative medicine.[1-3] Numerous applications of dECM scaffolds and hydrogels have been developed for peripheral nerve regeneration, musculoskeletal defect repair, wound healing, treatment of myocardial infarction, and therapeutic solutions for many other diseases.[4-6] dECM biomaterials, especially those derived from mammalian tissues, often exhibit specific bioactivity that is beneficial to facilitating cellular proliferation, migration, maturation, and directed differentiation, eventually promoting tissue remodelling.[7] It is worth noting that both xenogeneic and allogeneic tissues have been employed as original sources of biomaterials, which have been implanted in millions of patients for clinical treatments.[8-10]

Among many U.S. Food and Drug Administration-approved dECM scaffolds, those derived from allogeneic nerves provide off-the-shelf substitutes for nerve autografts (the gold standard) for functionally repairing peripheral nerve deficits.[11] Current commercialised decellularised nerve allografts, which include Avance (Axogen Inc., Alachua, FL, USA) and hANGs (Guangzhou Zhongda Medical Device Company, Guangzhou, China), maintain the nanofibrous structures and major components of the natural extracellular matrix (ECM) in human nerves.[11, 12] However, the practical use of such decellularised allografts is extremely limited by

the inadequate tissue supply as well as the great risk of disease transmission. Moreover, the allogeneic tissues are typically from old and cadaveric sources with large batch variability. The age of the source animal is one of the major factors that determines the biological function of dECM scaffolds. Those obtained from foetal/neonatal mammals result in greater regenerative performance than those produced from adult mammals.[13, 14]

Besides these commercialised decellularised nerve allografts, various xenogeneic dECM-based materials have been developed into functional scaffolds for peripheral nerve regeneration, as reported in many pre-clinical research studies.[9, 15, 16] Porcine decellularised nerve matrix (pDNM) has been processed in several other forms that allow customised fabrication of advanced nerve guidance conduits. For example, pDNM was intimately integrated into oriented electrospun nanofibres, which combined biological and topological nerve guidance and resulted in synergistic effects on directed neurite outgrowth and remyelination.[17-19] Additionally, pDNM can be further digested and form a hydrogel at ~37°C for easy processing or cell encapsulation. The pDNM pre-gel solution can be either directly injected into injury sites,[20] or perfused into pre-fabricated conduits for repairing peripheral nerve defects.[21, 22] Unlike clinical application of allogeneic dECM nerve grafts, the above-mentioned research studies used porcine dECM biomaterials and implanted them into xenogeneic animal models (mostly rodent sciatic nerve defect models), which demonstrated their beneficial properties in promoting nerve regeneration and functional recovery. Here we ask a question that is critical to biomaterials translation: can these xenogeneic dECM materials serve as viable substitutes for human decellularised nerve grafts for the clinical treatment of nerve defects? As a matter of fact, decellularised porcine tissues have been successfully commercialised and implanted into patients as biological scaffold materials, including dermis, heart valves, small intestinal submucosa, and others.[23] They are readily available and usually harvested from younger tissue sources.

Although both raw material sources have been used clinically, few comparative studies between the xenogeneic and allogeneic decellularised materials have been performed, and especially the host response to both materials is poorly understood. Although some research studies reported that dECM may suppress inflammatory responses after xenogeneic graft implantation into non-human animal models,[24, 25] a few cell surface antigens found in the tissue-derived dECM materials can potentially provoke host rejection or other immunogenic responses. For example, the galactosidase (Gal) epitope is commonly present in non-primate mammalian tissue but not in primates.[26] Compared to the innate immune response, very few studies have investigated changes in the acquired immune system following dECM scaffold implantation. Animal studies are typically used for biocompatibility assessments, but the immune cell receptors are distinctly different from those in humans.[27] On the other hand, considering the difficulties with conducting clinical trials or obtaining patient biopsies, the human immune response to these implanted biomaterials is hard to predict.

Herein, a comparative study was conducted to provide a comprehensive understanding of human and porcine decellularised nerve matrices (hDNM and pDNM), with respect to their microstructures, compositions, bioactivities, and the human immune responses post-implantation. First, the microstructures of both hDNM and pDNM were observed by scanning electron microscopy (SEM) and compared with each other after optimised decellularisation. Second, proteomic analysis revealed the compositional similarities and differences between the two materials. To briefly examine the bioavailability of both dECM materials, primary human Schwann cells (HSCs) were cultured on hydrogels derived from hDNM (hDNM-gel) and pDNM (pDNM-gel) for *in vitro* characterisation and comparison. Finally, the host response to the xenogeneic pDNM and allogeneic hDNM was assessed using a humanised mouse model. Hopefully, this comparative study can provide some insights into the clinical translations of tissue-derived dECM materials, especially pDNM which may serve as a substitute for decellularised hDNM allografts for the restoration of peripheral nerve defects.

Methods

Preparation of hDNM and pDNM

Human peripheral nerves (sciatic nerve) were obtained from Guangzhou Zhongda Medical Equipment Co., Ltd. (Guangzhou, China), and the study was approved by National Medical Products Administration of China (approval No. 20163131598, approved on August 26, 2021). Preparation of hDNM was performed according to a protocol described previously.[12] Briefly, the nerves were washed and then soaked in phosphate-buffered saline (PBS; B040100, Sangon Biotech, Shanghai, China) overnight. Then, the nerve tissues were agitated and rinsed in deionised water three times for 2 hours each time. The washed nerves were transferred to 3.0% (w/v) Triton X-100 (X100PC, Sigma-Aldrich, St. Louis, MO, USA) in PBS for 12 hours, and subsequently immersed in 4.0% sodium deoxycholate-containing PBS for another 6 hours. The resulting decellularised nerves were rinsed with deionised water for 1 day, followed by washing in isopropyl alcohol for 12 hours to remove lipids. Finally, after freezing at –40°C for 4 hours, the decellularised tissues were lyophilised for 2 days to produce the hDNM scaffolds.

The pDNM scaffolds were prepared by following a previously-reported protocol.[21] Briefly, the raw middle part of sciatic nerves and the corresponding distal end were harvested from miniature pigs (provided by the Experimental Animal Centre

1 Guangdong Engineering Technology Research Centre for Functional Biomaterials, School of Materials Science and Engineering, Sun Yat-sen University, Guangzhou, Guangdong Province, China; 2 Key Laboratory for Polymeric Composite & Functional Materials of Ministry of Education, School of Chemistry, Sun Yat-sen University, Guangzhou, Guangdong Province, China; 3 Guangdong Engineering Technology Research Centre for Peripheral Nerve Tissue, Department of Orthopaedic and Microsurgery, The First Affiliated Hospital of Sun Yat-sen University, Guangzhou, Guangdong Province, China; 4 Guangzhou Zhongda Medical Equipment Co., Ltd., Guangzhou, Guangdong Province, China

of the First Affiliated Hospital of Sun Yat-sen University), then decellularised by sequential treatment with 3.0% Triton X-100, 4.0% sodium deoxycholate, and rinsed with sterile water. Finally, the pDNM scaffold was obtained after degreasing with a mixed solvent (ethanol:dichloromethane = 1:2) and lyophilisation.

Scanning electron microscopy

The microstructures of both hDNM and pDNM were characterised by SEM (JSM-6380LA, Jeol Ltd., Tokyo, Japan). The sample preparation was implemented using a previously-reported method.[28] Briefly, both hDNM and pDNM scaffolds were cut into small pieces and mounted on aluminium sample stubs. Their cross-sections were sputtered with platinum/palladium and then subjected to observation using an SEM.

Histological staining

The hDNM and pDNM scaffolds were fixed in 4% paraformaldehyde (P0099, Beyotime Biotechnology, Shanghai, China) at 4°C for 12 hours. The fixed samples were dehydrated in graded alcohol, embedded in paraffin, and sectioned into 5-μm pieces. The sections were deparaffinised and then stained with haematoxylin-eosin by following the manufacturer's protocols (C0105, Beyotime Biotechnology). All samples were observed and images captured under a microscope (Leica Microsystems, Wetzlar, Germany).

Residual DNA detection

Samples of hDNM and pDNM (5 mg each) were digested in proteinase K solution (200 μL, 1 mg/mL; ST533, Beyotime Biotechnology) at 56°C until digestion was complete. After centrifugation at 10,190 × *g* for 10 minutes, the DNA content of the supernatant was determined using a Quant-iT PicoGreen kit (P11496, Invitrogen, Carlsbad, CA, USA) according to the YY/T 0606.25-2014 standard.[21]

Liquid chromatography-tandem mass spectrometry

Proteomic analysis of both hDNM and pDNM was performed by liquid chromatography-tandem mass spectrometry (LC-MS/MS).[29] Each dECM sample was added to sodium dodecyl sulphate lysis buffer (P0013G, Beyotime Biotechnology) at sample: buffer = 1:100 and then centrifuged at 14,000 × g for 30 minutes. The supernatant was analysed using a bicinchoninic acid protein assay kit (P0009, Beyotime Biotechnology). Afterwards, the proteins within the supernatant were digested with 25 μL trypsin solution, vortexed, and then incubated at 37°C overnight. The digested peptides were then desalted using Pierce C18 spin tips (90011, Thermo Fisher Scientific, Waltham, MA, USA). Peptide separation was implemented using high pH reverse-phase high-performance liquid chromatography on a C18 column. Finally, the isolated peptides were resuspended in 30 μL of solvent mixture (0.1% formic acid in acetonitrile) and analysed by online nanospray LC-MS/MS on an Orbitrap Fusion coupled to an EASY-nano-LC system (EASY-Nlc, Thermo Fisher Scientific).

Proteomic analysis

The raw data from the mass spectrometer were analysed using Protein Discoverer 2.1 (Thermo Fisher Scientific) against the porcine and mammalian protein UniProt database (https://www.uniprot.org/help/publications).[30] All searches required 10 ppm precursor mass tolerance, 0.02 Da fragment mass tolerance, strict tryptic cleavage up to two missed cleavages, and 1% protein false discovery rate.[31] Using these conditions, the protein expression values were obtained and corrected using $\log_2$ transformation. Meanwhile, the mean value of each protein in the pDNM and hDNM samples was calculated, termed pDNM and hDNM, respectively. The ratio of pDNM to hDNM was defended as the FoldChange. To identify differentially-expressed proteins, the value of $\log_2$FoldChange > 1 with adjusted *P*-value < 0.05 was used to identify those which were up-regulated, while the value of $\log_2$FoldChange < −1 with adjusted *P*-value < 0.05 was used to identify down-regulated proteins. Matrisome annotations of both porcine and human nerves were identified and classified using MatrisomeDB 2.0 (http://www.matrisomedb.org).[32] The proteomics figures, including unsupervised hierarchical clustering images, were generated using the DESeq package in the R language software (version 3.2.3, https://www.r-project.org/).

Preparation of hDNM-gel and pDNM-gel

To obtain the hDNM-gel and pDNM-gel, the lyophilised hDNM and pDNM scaffolds were first ground into powder using a Thomas Model 4 Wiley® Mill (Thomas Scientific, MA, USA). Then, the hDNM and pDNM powders were digested in 1 mg/mL pepsin dissolved in 0.01 M HCl (C0680110213, Nanjing Reagent, Nanjing, China). The digested solution was subjected to centrifugation at 44,760 × *g* (Optima MAX-XP, Beckman Coulter, Brea, CA, USA) for 30 minutes to remove all the undissolved particulates. Afterwards, the solution was neutralised to pH ~7.4 using 0.1 M NaOH (BD27, Guangzhou Chemical reagent Factory, Guangzhou, China) and diluted to reach an ionic equilibrium using 10× PBS (P1022-500, Solarbio, Beijing, China). The pre-gel solution was stored at −20°C or gelled at 37°C to obtain either hDNM-gel or pDNM-gel. The final concentration of both hydrogels was 1% (w/v).

Preparation of primary human Schwann cells

HSCs (Cat# 1700, ScienCell Research Laboratories, San Diego, CA, USA) were isolated from human spinal nerves. They were cultured in Schwann cell medium (P60123, ScienCell Research Laboratories) containing 1% Schwann cell growth supplement, 1% penicillin/streptomycin, and 10% foetal bovine serum. The HSCs were incubated at 37°C in a humidified 5% CO_2 incubator. After two passages, 1 × 10^6 cells per well were seeded into 6-well plates pre-coated with 0.5% (w/v) hDNM-gel or pDNM-gel, respectively.

Viability test

HSCs were seeded into 6-well plates pre-coated with hDNM-gel or pDNM-gel, as appropriate. After 2 days of culture, the medium was replaced with PBS containing live/dead staining reagent (1 mM) and incubated in the dark for 30 minutes, then images of the cells were captured for counting using a fluorescence microscope (Nikon, Tokyo, Japan).

Proliferation assessment

HSC proliferation was evaluated through 5-ethynyl-2′-deoxyuridine (EdU) labelling. After 24-hour incubation, the Schwann cell culture medium in each well was replaced with 200 μL fresh medium supplemented with EdU (final concentration 1 μM; C10310-3, RiboBio, Guangzhou, China). HSCs were then cultured for another 24 hours and fixed in 4% paraformaldehyde for 30 minutes. DNA incorporating EdU was labelled using an Alexa Fluor 488 Click-iT assay kit by following the manufacturer's instructions. Briefly, 1× Apollo dye reaction solution (100 μL) in combination with primary S100 antibody (mouse monoclonal, 1:1000, Cat# ab4066, Abcam, Cambridge, UK) was added to each well. After incubating for 2 hours at 37°C, cells were incubated with the goat anti-rabbit IgG Alexa Fluor 594-conjugated secondary antibody (1:5000, ab150080, Abcam) for 1 hour at 37°C. Next, cells were rinsed with PBS for 0.5 hour and their nuclei were stained with 6-diamidino-2-phenylindole-dihydrochloride (1 mM, C1006, Beyotime Biotechnology) in PBS for 10 minutes. Finally, observations were performed using a confocal microscope (LSM 900, Carl Zeiss Microscopy GmbH, Jena, Germany). The number of EdU^+ cells was quantified in at least three randomly-selected fields per sample ($n = 4$).

Cell migration

HSC migration was assessed by a wound-healing scratch assay. Cells were seeded into 6-well plates pre-coated with either hDNM-gel or pDNM-gel, and cultured until confluence. Then, a sterile 200 μL pipette tip was used to create a uniform linear scratch across the centre of the wells. Each well was rinsed with medium to remove the detached cells, and the remaining cells were incubated under standard culture conditions for another 24 hours. Images of cell migration across the wound were acquired immediately after scratching and after culture for 24 hours using a fluorescence microscope (Nikon). The migration rate was measured using ImageJ software (V1.8.0.112, National Institutes of Health, Bethesda, MD, USA).[33] Migration rate was calculated as follows:

$$Migration\ rate\ (\%) = \left(\frac{D_0 - D_t}{D_0}\right) \times 100\% \quad (1)$$

where D_0 and D_t represent the gap distance immediately after scratching and the width of the wound after 24 hours, respectively.

Quantitative polymerase chain reaction

HSCs cultured on hDNM-gel/pDNM-gel were harvested on day 2. Total RNA was extracted from the cultured cells using TRIzol reagent (15596-018, Invitrogen), following the manufacturer's instructions. Equal amounts of total RNA were subjected to reverse transcription using a Prime Script™ RT reagent kit (RR047Q, TaKaRa, Kyoto, Japan). Quantitative polymerase chain reaction (qPCR) amplification was performed on an Applied Biosystems Step One Real-Time PCR System using a SYBR Premix Ex Taq™ Kit (RR820A, Takara). Relative fold changes in mRNA expression were calculated using the formula $2^{-\Delta\Delta Ct}$ method.[34] The fluorescence threshold (Ct) values were obtained from the SDS Enterprise Database software (Sphera). The primer sequences used in this study are shown in **Table 1**.

Table 1. Primer sequences used for quantitative polymerase chain reaction

Gene	Primer sequence	Product size (bp)
MAP-2	Forward: 5'-CTT CAC GCA CAC CAG GCA CTC-3'	102
	Reverse: 5'-CCT TCT TCT CAC TCG GCA CCA AG-3'	
GAP43	Forward: 5'-TCC ACT GAT AAC TCG CCG TCC TC-3'	94
	Reverse: 5'-CAG CAG CAG TGA CAG CAG CAG-3'	
MBP	Forward: 5'-CGA GGA CGG AGA TGA GGA GTA GTC-3'	197
	Reverse: 5'-CAG CTC AGC GAC GCA GAG TG-3'	
MPZ	Forward: 5'-TGG TGC TGT TGC TGC TGC TG-3'	185
	Reverse: 5'-GGT GCT TCT GCT GTG GTC CAG-3'	
GFAP	Forward: 5'-GCT GCG GCT CGA TCA ACT CAC-3'	169
	Reverse: 5'-GGT GGC TTC ATC TGC TTC CTG TC-3'	
S100β	Forward: 5'-ACA ATG ATG GAG ACG GCG AAT GTG-3'	80
	Reverse: 5'-GAA CTC GTG GCA GGC AGT AGT AAC-3'	
β-Actin	Forward: 5'-GCA AGT GCT TCT AGG CGG ACT G-3'	195
	Reverse: 5'-CTG CTG TCA CCT TCA CCG TTC C-3'	

Note: ECM: extracellular matrix; GAP43: growth-associated protein 43; GFAP: glial fibrillary acidic protein; MAP-2: microtubule-associated protein-2; MBP: myelin basic protein; MPZ: myelin protein zero.

Preparation of pDNM-enzymolysis

To eliminate the α-Gal antigen in the pDNM, pDNM-enzymolysis was prepared according to a previously-described method with a slight modification.[35] Briefly, the lyophilised pDNM samples were incubated with 100 U/mL α-galactosidase (G8507, Merck, Darmstadt, Germany) for 4 hours at 25°C with gentle agitation. Then, the samples were washed with PBS solution three times, 30 minutes each time, followed by immersion in saline overnight to completely remove the residual enzyme.

Detection of α-Gal antigen

The content of the α-Gal antigen was characterised using western blotting, immunofluorescence staining, and enzyme-linked immunosorbent assay.

Western blot

The hDNM, pDNM, and pDNM-enzymolysis samples were lysed by RIPA buffer (P0013, Beyotime Biotechnology). After quantification by bicinchoninic acid assay, the obtained proteins were separated and transferred to polyvinylidene fluoride membranes (IPVH00010, Millipore, Bedford, MA, USA). Afterwards, the membranes were treated with primary α-Gal antibody (human polyclonal, 1:1000, Santa Cruz Biotechnology, Santa Cruz, CA, USA, Cat# sc-517442) overnight, followed by horseradish peroxidase-conjugated secondary antibody (anti-rabbit, 1:10,000, Bioworld, Nanjing, China, Cat# BS13278) at 37°C for 1 hour. Finally, the membranes were assessed using a chemiluminescence ECL kit (P0018FS, Beyotime Biotechnology) and the results were observed using the ChemiDoc™ XRS+ Imaging System (GelDoc XR+, Bio-Rad, Hercules, CA, USA). Western blotting of MHC-1 in both hDNM and pDNM scaffolds followed a similar procedure except that a primary MHC-1 antibody (human polyclonal, 1:1000, Abcam, Cat# ab134189) was used.

Immunofluorescence staining

The samples were cut into 10-μm-thick sections and washed three times with 0.01 M PBS. After blocking with 5% bovine serum albumin (HY-D0842, MedChemExpress, Newark, NJ, USA) for 30 minutes, the specimens were incubated with primary α-Gal antibody (1:1000) overnight at 4°C. Then a rabbit anti-human IgG Alexa Fluor 488-conjugated secondary antibody (1:5000, Abcam, Cat# ab150189) was added and the samples were incubated at 37°C for 1 hour. Immunofluorescence images were obtained using a confocal laser microscope (DM6000, Leica Microsystems). The mean grey value of α-Gal was calculated using the integrated density divided by the area of the selected region. These parameters were quantified using ImageJ software. Images of five randomly-selected fields in each sample and three samples in each group were subjected to statistical analysis.

Enzyme-linked immunosorbent assay

The dissected nerve tissues with/without decellularisation and the pDNM-enzymolysis samples were weighed and mixed in radio immunoprecipitation assay lysis buffer. After centrifugation at 1790 × *g* for 10 minutes, the α-Gal in the supernatants was quantified using an α-Gal Antigen Quantitative Detection Kit (7010, SanYao Science & Technology Co, Beijing, China) according to the manufacturer's instructions. Briefly, after premixing with the dilution buffer, the samples were incubated in 96-well microplates coated with α-Gal antibody for incubation at room temperature for 1 hour. Then, 200 μL volume of α-Gal antibody working solution was added to each well and incubated at room temperature for another 2 hours. Subsequently, the tetramethylbenzidine substrate solution (100 μL/well) was added to enable the reaction at 25°C for 30 minutes. The reaction was stopped by adding stop solution (50 μL/well). The enzyme-linked immunosorbent assay results were obtained at 450 nm with a microplate reader (Thermo Fisher Scientific, MA, USA).

Detection of endotoxin

Chromogenic endpoint *Tachypleus amebocyte* lysate (Chinese Horseshoe Crab Reagent Manufactory, Xiamen, China) was used for endotoxin quantification, which was carried out according to the manufacturer's protocol. Briefly, pDNM or hDNM suspension (10 mg/mL, 100 μL) plus Tachypleus amebocyte lysate (100 μL) were sequentially added to a 96-well plate. After incubating at 37°C for 10 minutes, 100 μL chromogenic matrix solution was added to each well. After 15 minutes, 500 μL azo reagent solution was added to each well. The absorbance of each well was measured with a microplate reader (545 nm, Thermo Fisher Scientific). This experiment was repeated three times. The linearity of the standard was verified using endotoxin standard solution.

Humanised mouse model

The female mice (20–25 g) used for immune evaluation were peripheral blood mononuclear cell-NOD-Prkdcscid Il2rg^{null} (PBMC-NPG) mice (Stock No. VS-AM-004, also termed Hu-mice), which were purchased from Beijing Vitalstar Biotechnology, aged 8–10 weeks. All animal experiments were performed in accordance with a protocol that was approved by the Institutional Animal Care and Use Committee of Beijing Vitalstar Biotechnology Company (approval No. VST-SY-20191008, approval date: October 8, 2019), and were designed and reported according to the Animal Research: Reporting of *In Vivo* Experiments (ARRIVE) guidelines.[36] NPG immunodeficient mice were conditioned with sublethal (1.4 Gy) whole-body irradiation.[37] After 6 hours of irradiation, the animals were transfused intravenously with 2×10^7 human peripheral blood mononuclear cells (PBMCs) isolated from the peripheral blood of healthy adult donors.[38] Then, the mice were employed for dECM immunity experiments for 8 weeks.

Immune response *in vivo* assay

To evaluate the host immune response in humanised mice, the pDNM or hDNM solutions were injected into PBMC-NPG mice subcutaneously. Biomaterial injection and harvesting were performed following a previously-reported approach (**Additional Figure 1**).[39] After anaesthesia with 1.8% isoflurane (Forene™, Abbott Laboratories SA, IL, USA) in O_2/N_2 (30%/70%) for 5 minutes, each animal was pre-injected with 100 μL of sterile black ink in the back to visually label the matrices for ease of identification upon harvesting. Subsequently, four sites of the same dorsal region received a single type of dECM solution (pDNM or hDNM, 10 mg/mL, 250 μL per site) by evenly spaced subcutaneous injections. One week post injection, the animals were deeply anaesthetised by inhaling 1.8% isoflurane and transcardially perfused with 10 mL 0.9% normal saline, followed by 10 mL of ice-cold 4% paraformaldehyde in 0.1 M PBS. The subcutaneous tissue with all the injection sites, together with their neighbouring regions, was harvested for histological analysis.

Furthermore, the adaptive immune responses of both dECMs were examined using the same humanised mouse model. The PBMC-NPG mice were injected with 1 mL pDNM, hDNM, or pDNM-enzymolysis solution (concentration = 10 mg/mL) through the caudal vein during isoflurane anaesthesia. One week after injection, the venous blood was harvested from the eyeballs and collected into heparin anticoagulant tubes for flow cytometry.

In the above-mentioned two processes, each experiment contained four groups (n = 3 for each group): control, hDNM, pDNM, and pDNM-enzymolysis groups. The PBMC-NPG mice that received 1 mL pDNM, hDNM, or pDNM-enzymolysis solution were regarded as hDNM, pDNM, and pDNM-enzymolysis groups, respectively. The control group received the same volume of sterile normal saline.

Flow cytometry

The blood cells collected in heparin anticoagulant tubes were washed with PBS and incubated with the antibody panel for 30–45 minutes at 4°C in the dark. Then, the cells were lysed with Pharm Lyse (Cat# 555899, BD Biosciences, San Jose, CA, USA) for 4 minutes. After centrifugation, the samples were suspended in PBS for data acquisition by flow cytometry (BD FACSCanto II, Beckman Coulter). Fluorochrome-conjugated monoclonal antibodies to the following human or mouse antigens were used: FITC-anti mouse CD45 (Biolegend, San Diego, CA, USA, Cat# 147710, RRID: AB_2563541), PE-anti human CD45 (Biolegend, Cat# 304039, RRID: AB_314395), FITC-anti human CD45 (Biolegend, Cat# 304038, RRID: AB_314393), PE-anti human CD3 (Biolegend, Cat# 300308, RRID: AB_314043), APC-anti human CD19 (Biolegend, Cat# 392506, RRID:AB_2750096), PE-Cy7 anti human CD4 (Biolegend, Cat# 357410, RRID: AB_2565661), APC-anti human CD8 (Biolegend, Cat# 344722, RRID: AB_2075390). A FACSCalibur instrument and Cellquest software were used for flow cytometry analysis.

Statistical analysis

Pearson's correlation analysis was performed using IBM SPSS Statistics 27 (Armonk, NY, USA). The other statistical analyses were performed using GraphPad Prism 8.0.2 (GraphPad Software Inc., La Jolla, CA, USA, www.graphpad.com). The data are expressed as mean ± standard deviation (SD) for continuous variables. When three groups of data were compared, one-way analysis of variance followed by Tukey's *post hoc* test was used. Differences were considered statistically significant when $P < 0.05$.

Results

Decellularisation and structural characterisations of hDNM and pDNM

The cross-sectional morphologies of the native nerve tissues in both human and porcine showed substantial nerve tract-like ellipsoidal shape (**Additional Figure 2**). After optimised decellularisation, the ultrastructures of hDNM and pDNM were characterised by SEM (**Figure 1A–D**). As shown in **Figure 1A1** and **B1**, both DNM scaffolds were composed of many decellularised nerve bundles/fascicles and interfascicular connective tissues. Higher resolution micrographs showed that each nerve fascicle consisted of numerous microchannels with diameters ranging from 5 to 20 μm (**Figure 1A2–4** and **B2–4**). Furthermore, the longitudinal view of both DNM scaffolds showed lamellar microstructures with rather smooth surfaces (**Figure 1C1** and **D1**). The magnified images clearly showed that these laminar structures (i.e., endoneurium) were formed by closely-assembled and longitudinally-aligned nanofibres, each with a diameter of ~100 nm (**Figure 1C2**, **3** and **D2**, **3**). It was apparent that both hDNM and pDNM consisted of similar micro- and nanostructures, and no significant differences were found between the two scaffolds, except for the slightly misaligned nanofibres found in hDNM (**Figure 1C3**) and the randomly-distributed microbeads on the pDNM. These minor variations were most likely due to the slight disparities in decellularisation protocols.

Results from haematoxylin-eosin staining showed that cellular content in either dECM scaffold, implying that both nerve tissues underwent complete decellularisation (**Figure 1E**). In the hDNM, the shape of nerve tracts was almost intact after decellularisation, while the pDNM revealed a slightly disordered extracellular matrix of the porcine sciatic nerves. Moreover, DNA content in the dECM scaffolds was also quantified (**Figure 1F**). The result showed that the DNA content in native human nerves and native porcine nerves was 572.6 ± 161.2 ng/mg and 300.9 ± 116.9 ng/mg, respectively. After decellularisation, their DNA contents were reduced approximately 94.1% (native human nerve) and 88.1% (native porcine nerve). Nevertheless, enzyme digestion did not further reduce the content of residual DNA (hDNM *vs.* hDNM-gel: $P > 0.05$; hDNM *vs.* hDNM-gel: $P > 0.05$). The minimal residual DNA content in hDNM (34.2 ± 9.5 ng/mg), hDNM-gel (33.3 ± 7.7 ng/mg), pDNM (36.1 ± 11.2 ng/mg) and pDNM-gel (28.8 ± 11.8 ng/mg) met the globally-recognised standard (50 ng/mg).[40] Although repeated and intensive chemical decellularisation would further reduce the residual DNA content within the hDNM and pDNM, their composition and microstructures might also be seriously damaged under such harsh conditions.

Proteomic analysis of hDNM and pDNM

Since the dECMs consist of numerous types of proteins from the native nerve tissues, the compositions of pDNM and hDNM were identified by LC-MS/MS and compared by proteomic analysis. After Pearson's correlation analysis, it was noticed that the unsupervised hierarchical clustering in the pDNM and hDNM samples were highly correlated with each other, but clustered separately between different groups (**Figure 2A**). Through mass spectrometric analysis, it was noted that the pDNM and hDNM shared 1431 characterised proteins in common, while 46 proteins in pDNM were upregulated and 48 proteins were downregulated compared to hDNM (**Figure 2B**). The protein compositions in each dECM sample are shown as a heatmap (**Figure 2C**). The proteomics results confirmed that the major components of pDNM and hDNM have the same functionalities, except for the minor protein species that are more specific corresponding to their original tissue sources.

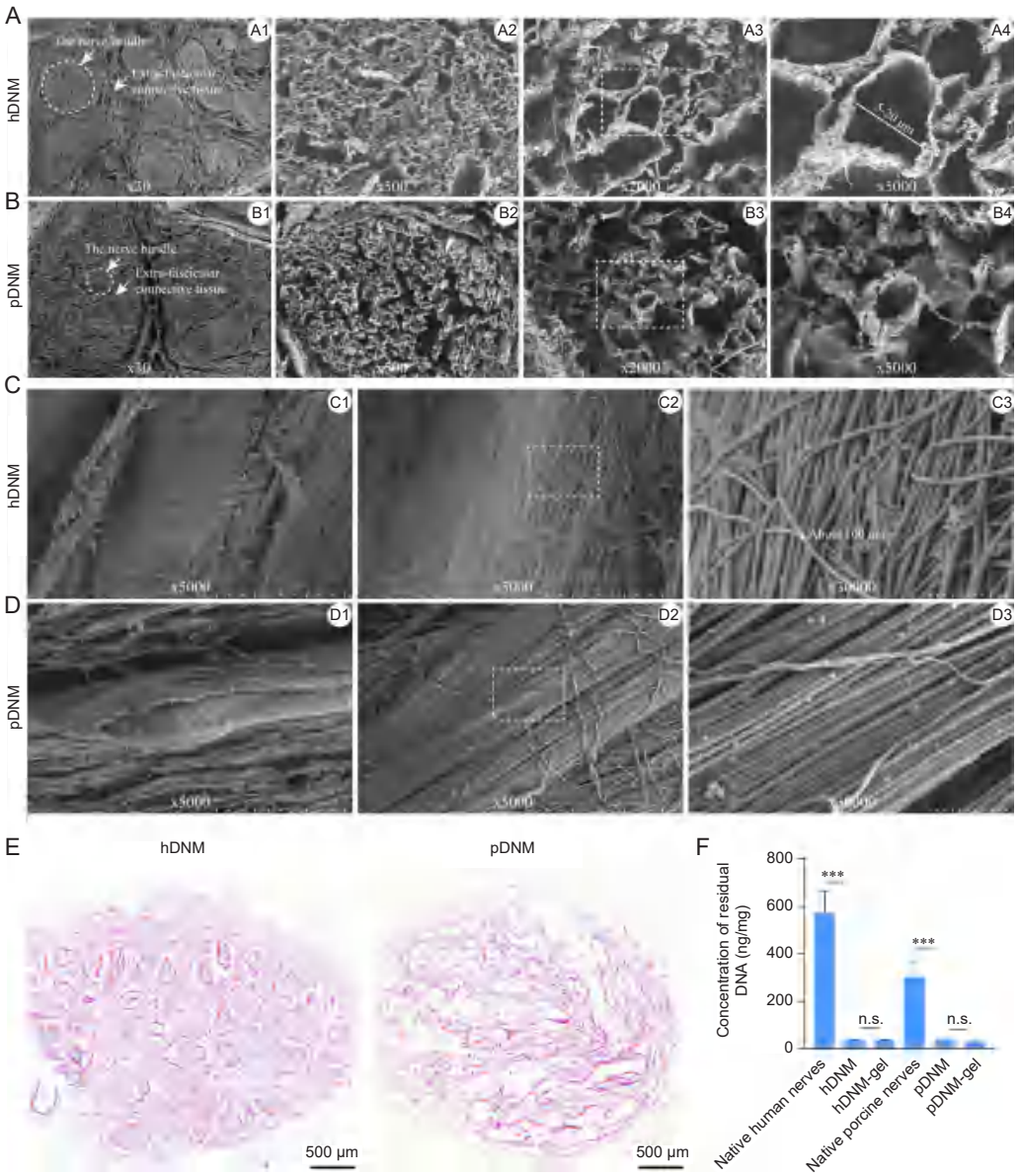

Figure 1. Structural and histological characterisations of the hDNM and pDNM scaffolds. Representative SEM micrographs of the hDNM (A) and pDNM (B) at lower magnification. Representative SEM micrographs of the hDNM (C) and pDNM (D) at higher magnification. Scale bars: 1 mm in A1, B1; 100 μm in A2, B2; 20 μm in A3, B3; 10 μm in A4, B4, C1, C2, D1, D2; and 1 μm in C3, D3. (E) Representative micrographs of hDNM and pDNM cross-sections after H&E staining. Scale bars: 500 μm. (F) DNA content quantified in the fresh tissues, hDNM, pDNM, hDNM-gel and pDNM-gel. Data are expressed as mean ± SD (n = 4). ***P < 0.001. H&E: haematoxylin-eosin; hDNM: human decellularised nerve matrix; n.s: not significant; pDNM: porcine decellularised nerve matrix; SEM: scanning electron microscopy.

We further investigated the diversity of ECM proteins identified in the hDNM and pDNM using an ECM-specific categorisation database, Matrisome DB 2.0. The ECM proteins, which are often divided into two categories: core matrisome and matrisome-associated proteins, are essential for tissue morphogenesis, differentiation, and homeostasis. As shown in the Venn diagram (**Figure 3A**), 68 ECM proteins were identified in the pDNM samples. Meanwhile, 53 ECM proteins were detected in the hDNM, among which 35 proteins were also found in the pDNM. Other than these shared species of proteins, 33 were identified only in the pDNM and 18 specific proteins were found in the hDNM. These specific ECM proteins are listed in **Table 2**. Detailed matrisome analysis further revealed that the matrisome-associated proteins, which included the ECM-related proteins, the ECM regulators, and many secreted factors, were particularly enriched in the pDNM. Contrarily, the hDNM possessed a larger proportion of core matrisome proteins, including the ECM glycoproteins and proteoglycans (**Figure 3B** and **C**). The heatmap results showed that the relative abundance of the 35 shared proteins identified in the pDNM was 24, which was higher than that in the hDNM (11, **Figure 3D**). Additionally, the volcano plot shows that the number of up-regulated matrisome proteins in the pDNM was twice as many as that of the down-regulated

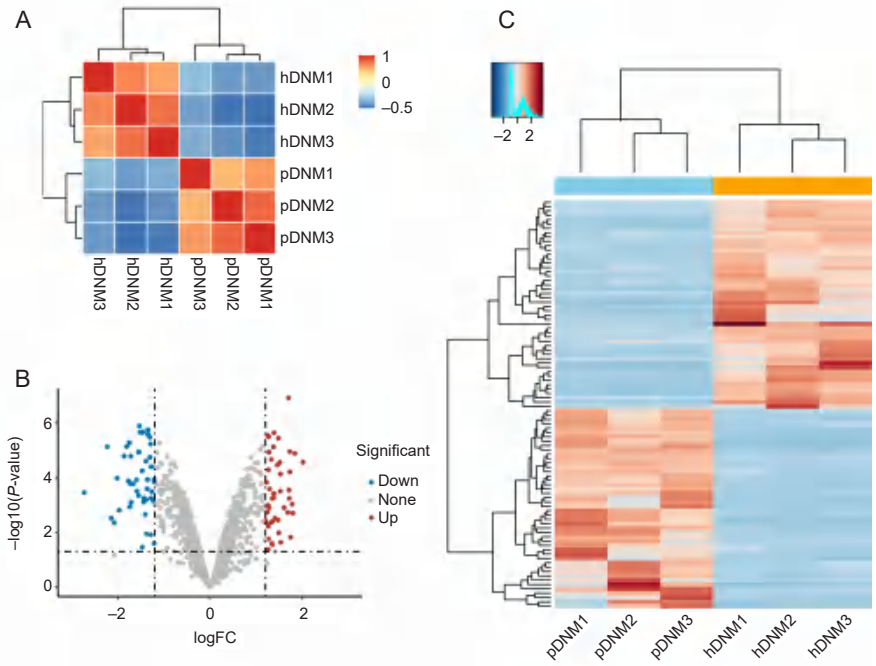

Figure 2. Proteomic analysis of hDNM and pDNM. (A) Unsupervised hierarchical clustering between the hDNM and pDNM using Pearson's correlation. (B) Volcano plot showing the differentially-expressed proteins between the hDNM and pDNM. (C) Heatmap and cluster dendrogram of protein abundances in the hDNM and pDNM. FC: fold change; hDNM: human decellularised nerve matrix; pDNM: porcine decellularised nerve matrix.

Table 2. Specific dECM proteins identified only in the pDNM or hDNM

Classification		pDNM	hDNM
Core matrisome	ECM glycoproteins	LAMB3, MXRA5, EDIL3, SLIT1, VWA3A, EMILIN3	EMILIN2, CTGF, LAMA1, SRPX
	Collagens	None	COL6A6
	Proteoglycans	None	None
ECM-associated proteins	ECM-related proteins	ELFN2, FREM2, C1QL4, PLXNA2, PLXNA4, ANXA9	GPC5, FCN1, PLXNA3
	ECM regulators	ADAMTS14, TIMP3, CTSG, MMP12, MEP1A, ADAMTS7, ADAMTS5	FAM20C, ADAMTS21, ADAMTS15, ADAMTSL3
	Secreted factors	WNT3A, BMP3, INHBA, MSTN, S100A4, NFSF15, FGF14, S100A13, ANGPTL7, HHIP, BRINP2, GDF3, FGF9	MEGF11, IL4, GDF5, INHBB

Note: dECM: decellularised extracellular matrix; ECM: extracellular matrix; hDNM: human decellularised nerve matrix; pDNM: porcine decellularised nerve matrix.

proteins (**Figure 3E**), among which the upregulated proteins were positively regulated with cellular proliferation (i.e., CSPG4, FGF2), migration (i.e., SLIT3, CSPG4, LAMA2), and maturation (i.e., FGF2). Among the three downregulated proteins, PODN negatively regulated cell proliferation and migration (**Figure 3E**). It is acknowledged that these diverse proteomic compositions found in dECMs can have strong regulatory effects on cell behaviour.

Cellular behaviour regulated by hDNM and pDNM hydrogels

To easily examine the functionalities of both pDNM and hDNM for cell culture and regulating cellular behaviours *in vitro*, both dECM scaffolds were first converted into their corresponding hydrogels, i.e. pDNM-gel and hDNM-gel, respectively. Then, these hydrogels were employed to culture HSCs, a classic glial cell extracted from the human spinal nerve that can provide a simple, well-defined, and accessible mammalian *in vitro* model for investigating nerve cell and material interaction.[41] Cell viability, proliferation, migration, and functional expressions were systematically investigated and compared using hDNM-gel and pDNM-gel.

First, the cytocompatibility of both dECM hydrogels was assessed by live/dead staining. It should be emphasised that very few dead cells were identified after 48 hours of culture, indicating that both pDNM-gel and hDNM-gel were highly compatible with the HSCs (**Figure 4A**). Furthermore, it was also noticed that the total number of HSCs growing on both hDNM-gel and pDNM-gel were nearly double that of the control group, which suggested that the dECM hydrogels

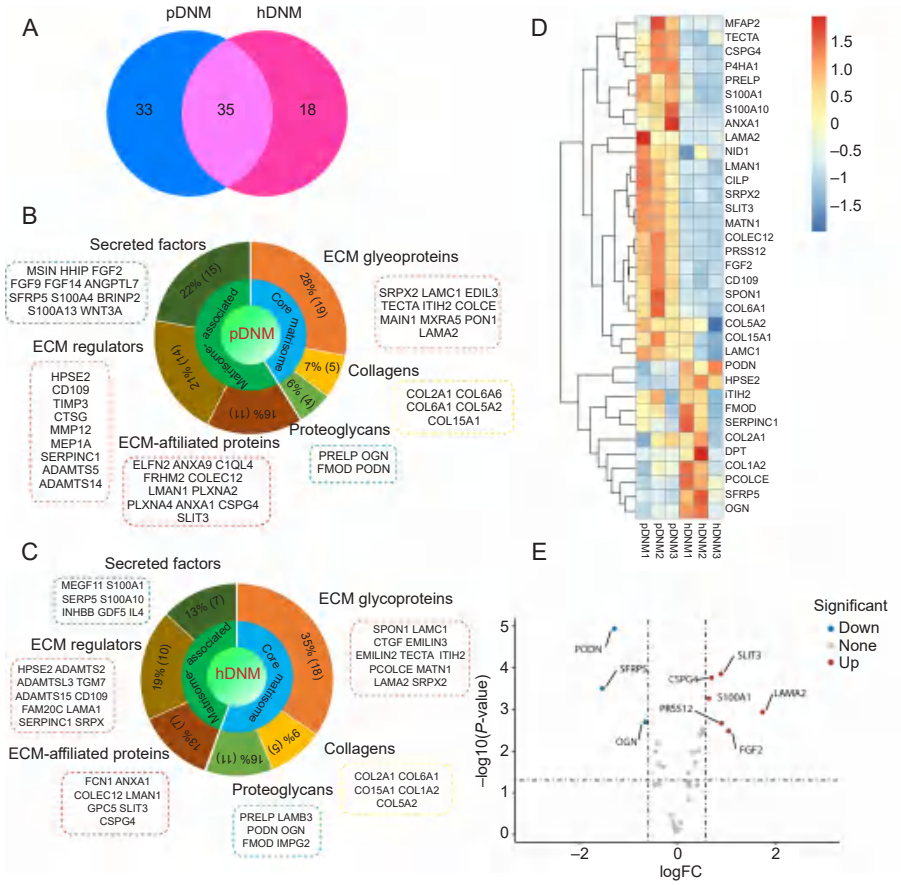

Figure 3. Matrisome analysis of the proteomic composition in pDNM and hDNM. (A) Venn diagram showing the number of ECM proteins detected in hDNM and pDNM. (B, C) Percentages of the ECM proteins and their corresponding matrisome subcategories identified in pDNM (B) and hDNM (C). (D) Heatmap representing significant distinctions in the co-expressed ECM proteins between pDNM and hDNM. The relative abundance of the 35 shared proteins identified in pDNM was higher than that in hDNM. (E) Volcano plot of the differentially expressed ECM proteins in pDNM compared to hDNM. The red and blue dots indicate the significantly up- and down-regulated ECM proteins, respectively (n = 3 for both pDNM and hDNM). ECM: extracellular matrix, hDNM: human decellularised nerve matrix; pDNM: porcine decellularised nerve matrix.

also promoted HSC proliferation. This was confirmed by immunofluorescence staining, when the cultured HSCs were double stained by EdU and S100 to label proliferating cells and Schwann cells, respectively. It was noted that the number of EdU/S100 co-expressing cells cultured on hDNM-gel and pDNM-gel were both significantly greater compared with the control group (**Figure 4B**). However, no significant difference was evident between the two hydrogel groups (**Figure 4C**). These results indicated that both hydrogels exhibited similar biological functions in facilitating HSC proliferation. Additionally, the migration of HSCs was evaluated using a wound healing assay. It was obvious that the HSCs migration was significantly facilitated on both the hDNM-gel and pDNM-gel within 24 hours, resulting in much higher migration rates, but there was not much difference between the two dECM hydrogel groups (**Figure 4D** and **E**).

Furthermore, to validate the bioactivities of the dECMs in promoting cell behaviours and for comparison, the mRNA levels of several genes, which are highly related to neuronal growth, remyelination, and differentiation, were assessed by qPCR. The results showed that both DNM hydrogels effectively upregulated the mRNA expression levels of MAP-2, GAP43, MBP, and MPZ, but no significant changes were evident regarding GFAP and S100β gene expression (**Figure 4F**). These results suggested that the dECM hydrogels contributed to facilitating HSC growth and remyelination but had a minor modulatory effect on their differentiation. Comparisons between the hDNM-gel and pDNM-gel groups revealed no significant discrepancies in the expression levels of the above-mentioned genes. The results from cell culture demonstrated that both hDNM and pDNM hydrogels exhibited similar bioactivities in regulating the survival, proliferation, migration, and maturation of cultured HSCs.

α-Gal antigen and other immunogenic contents retained in hDNM and pDNM

Tissue-derived dECM materials, especially xenogeneic pDNM, inevitably contain small amounts of antigens and other biomolecules that might evoke host rejection and foreign body responses, and such molecules include α-Gal, MHC-1, and endotoxins.[42] To confirm the existence of these immunogens in hDNM and pDNM, we first evaluated the α-Gal antigen

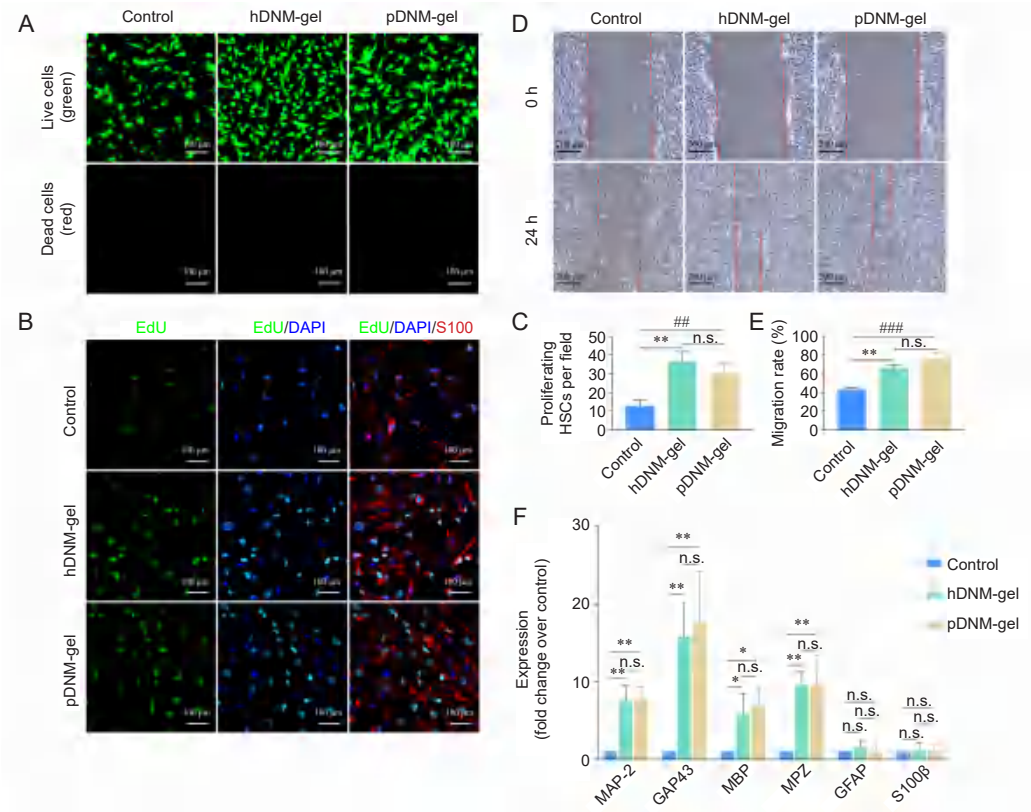

Figure 4. Bioactivities of both hDNM-gel and pDNM-gel in regulating the behaviours of cultured HSCs. (A) Representative fluorescence micrographs of the cultured HSCs on hDNM-gel and pDNM-gel after 48 hours of incubation and live/dead staining, compared to the control (no hydrogel). Scale bars: 100 μm. (B) Representative fluorescence confocal micrographs of HSCs cultured for 48 hours and immunostained with EdU (green), S100 (red), and DAPI (blue). Scale bars: 100 μm. (C) Number of proliferating ($EdU^+/S100^+$) HSCs in B. (D) Wound healing characterisation showing the wound gaps at 0 and 24 hours in the control, hDNM-gel, and pDNM-gel groups. Scale bars: 100 μm. (E) HSC migration based on the wound healing experiments in D (n = 3). (F) MAP-2, GAP43, MBP, MPZ, GFAP, and S100β mRNA expression of the HSCs cultured on hDNM-gel and pDNM-gel were significantly upregulated compared to the control group (n = 5). β-actin was used as the reference. Data are shown as the mean ± SD. *P < 0.05, **P < 0.01, ***P < 0.001. DAPI: 6-diamidino-2-phenylindole-dihydrochloride; dECM: decellularised extracellular matrix; EdU: 5-ethynyl-2′-deoxyuridine; GAP43: growth-associated protein 43; GFAP: glial fibrillary acidic protein; hDNM-gel: human decellularised nerve matrix hydrogel; HSCs: human Schwann cells; MAP-2: microtubule-associated protein-2; MBP: myelin basic protein; MPZ: myelin protein zero; n.s, not significant; pDNM-gel: porcine decellularised nerve matrix hydrogel.

that is commonly identified in non-primate mammalian tissues as a factor that may elicit severe immune rejection after implantation. The western blot results showed that no α-Gal was detectable in the hDNM, meanwhile, a large amount of α-Gal content was evident in the pDNM, which confirms that this antigen is a sort of specific protein that does not exist in human tissue. Once the pDNM was enzymatically hydrolysed by α-galactosidase, the α-Gal content was found to be effectively removed from the resulting pDNM-enzymolysis (**Figure 5A** and **B**). The immunofluorescence staining results using α-Gal antibody confirmed the absence of α-Gal in hDNM, and the presence of the Gal epitope in the pDNM was highly diminished once treated with α-Gal (**Figure 5C** and **D**). Furthermore, it was noticed that the abundant α-Gal antigen in raw porcine nerve tissues was significantly reduced after decellularisation (i.e., in pDNM), and further erased after hydrolysation (**Figure 5E**). These results suggested that although some α-Gal was present in the pDNM, the amount of this xenoantigen can be efficiently reduced by post-decellularisation modification.

Considering other possible factors that may lead to host rejection, another antigen, MHC-1, that may elicit host rejection was also assessed by western blotting. It was noted that MHC-1 was present in both hDNM and pDNM; however, the pDNM contained more MHC-1 antigen compared to the hDNM (P < 0.01; **Figure 5F** and **G**). Furthermore, we also evaluated endotoxin contamination in both dECMs using a kinetic turbidimetric technique, which revealed that hDNM and pDNM had similar contents of endotoxin (**Figure 5H**).

Host immune responses to hDNM and pDNM in a humanised mouse model

To better assess the human immune response after implantation of DNMs, a humanised mouse model was established using the PBMC-NPG mice. These Hu-mice possess human

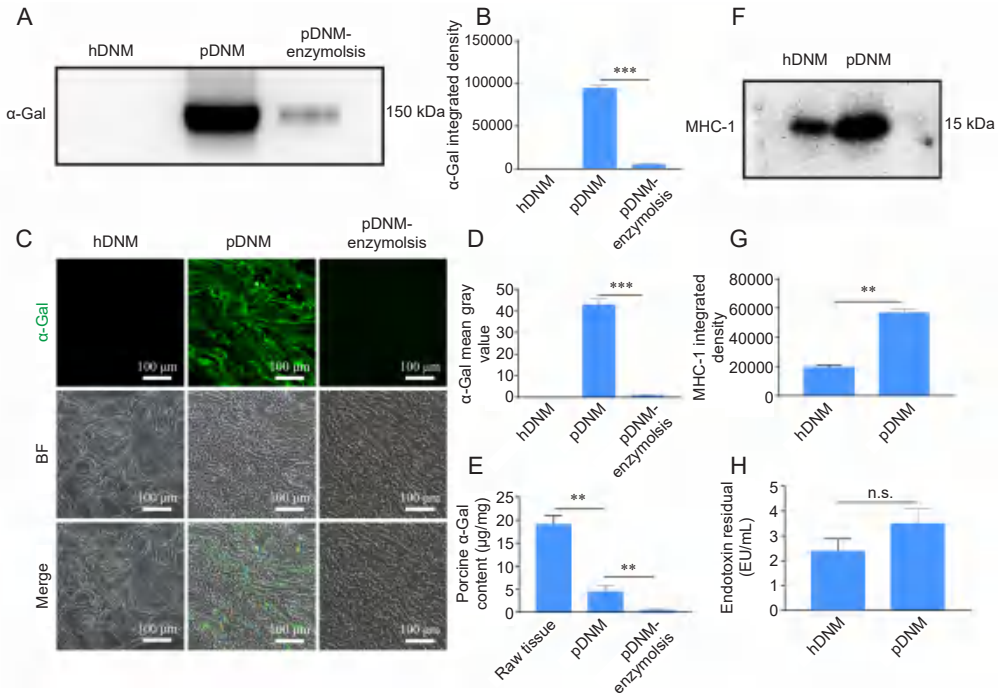

Figure 5. Detection of the immunogenic contents (α-Gal, MHC-1, and endotoxin) in hDNM and pDNM. (A, B) Western blot results and quantification of α-Gal antigen in hDNM, pDNM, and pDNM pre-treated with α-galactosidase (pDNM-enzymolysis). (C) Immunofluorescence staining and BF micrographs showing the presence of α-Gal antigen (green) within the hDNM, pDNM, and pDNM-enzymolysis samples. Scale bars: 100 μm. (D) Quantification of the immunoreactivity of α-Gal antigens. (E) Quantification of α-Gal content in raw porcine nerve tissues, pDNM, and pDNM after α-Gal treatment. (F) Western blot image and (G) quantification of the MHC-1 content in hDNM and pDNM. (H) Quantification of the endotoxin content in hDNM and pDNM. Data are presented as mean ± SD ($n = 3$). $^{**}P < 0.01$, $^{***}P < 0.001$. α-Gal: α-galactosidase; BF: bright field; hDNM: human decellularised nerve matrix; MHC-1: major histocompatibility complex 1; n.s.: not significant; pDNM: porcine decellularised nerve matrix.

immune cells that can respond to immunogens, including T- and B-cells.[43] The prepared hDNM, pDNM, and pDNM-enzymolysis were subcutaneously injected into the back of the Hu-mice. One week after injection, the subcutaneous tissue around the injection site of each Hu-mouse was sectioned for histological analysis, and the foreign body reactions were evaluated by the extent of cellular infiltration (**Figure 6A**). Unlike normal subcutaneous tissue in a humanised mouse model (control group), after administration of the dECM materials, larger cavities were observed, and cells could be seen to have intensively infiltrated into the injected area. The cell infiltration was particularly significant in the pDNM injected region, rather than the hDNM and pDNM-enzymolysis groups. It was interesting that the number of infiltrated cells in the pDNM-enzymolysis group was about the same as that of the hDNM group, suggesting similar foreign body responses post-implantation (**Figure 6B**).

To evaluate the adaptive immune responses of the implanted Hu-mice, 10 mg/mL hDNM, pDNM and pDNM-enzymolysis solutions were administered to PBMC-NPG mice through intravenous injection. One week after treatment, their venous blood was collected to identify and quantify the human leukocytes ($hCD45^+$) and their subpopulations, including B cells ($hCD45^+hCD19^+$), T helper cells ($hCD3^+hCD4^+$), and cytotoxic T cells ($hCD3^+hCD8^+$) using flow cytometry. First, it was noted that the percentage of human immune cells in the blood was detectable in the control group (3.20 ± 0.25%), although the mouse leukocytes ($mCD45^+$) were still responsible for the dominant percentage (80.35 ± 3.47%; **Figure 6C** and **D**). Meanwhile, all the dECM-injected Hu-mice exhibited a significantly increased number of human immune cells. The administration of pDNM led to the greatest number of leukocytes ($hCD45^+$ 17.96 ± 1.17%). The hDNM-treated group resulted in a slightly better immune response but the percentage of $hCD45^+$ cells still increased to 11.06 ± 0.96%. Surprisingly, the introduction of pDNM-enzymolysis elicited minimal host immune response, with the fraction of $hCD45^+$ cells only elevated to 6.46 ± 1.16%, which was even less than that of the hDNM group. A similar trend was observed regarding the number of human B cells. The total number of B cells increased to 730 ± 48 per 1000 cells after pDNM administration, which was much greater than that of the hDNM injected Hu-mice (**Figure 6E**). Meanwhile, the injection of pDNM-enzymolysis induced a very small increment of the human B cell population, which was close to that of the Hu-mice without materials implantation.

We next explored the different T cell subtypes and their accumulation after injection of dECMs into the Hu-mice (**Figure 7A**), which can verify the type of host immune responses to the implantable biomaterials, whether they

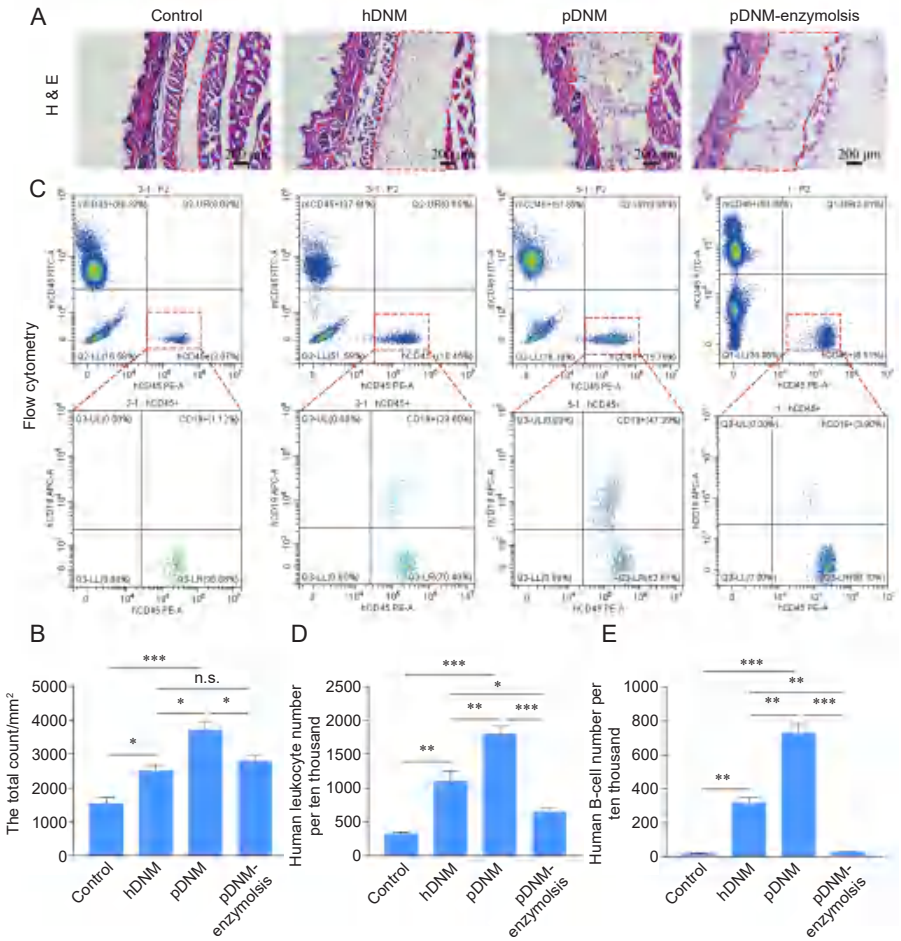

Figure 6. Host immune responses to subcutaneously injected hDNM, pDNM, and pDNM-enzymolysis in a humanised mouse model. Hu-mice received the same volume of sterile saline as the control. (A) H&E staining of the subcutaneous tissues sectioned from the Hu-mice in each group. Scale bars: 200 μm. (B) The total number of infiltrating cells in the dotted box in A based on H&E histological staining. (C) Flow cytometry results showing the human immune cells after treatment. (D, E) Quantitative analysis of the density of human leukocytes (hCD45$^+$) (D) and the density of human B cells (hCD45$^+$ hCD19$^+$) (E) based on flow cytometric assessments. Data are presented as mean ± SD (n = 3). *P < 0.05, **P < 0.01, ***P < 0.001. H&E: haematoxylin-eosin; hDNM: human decellularised nerve matrix; n.s: not significant; pDNM: porcine decellularised nerve matrix.

are pro-remodelling or pro-inflammatory. It was noted that the introduction of pDNM led to the greatest number of T cells. Though the allogeneic hDNM also resulted in a larger T cell repopulation, this was still much less than that of pDNM group. The hydrolysed pDNM (pDNM-enzymolysis), however, manifested a much slower T cell repopulation; the density of T cells was even smaller than that of the hDNM group (**Figure 7B**). Such distinct differences between the hDNM, pDNM, and pDNM-enzymolysis groups were further confirmed by sorting the T cells into two subtypes, T helper cells and cytotoxic T cells. Both the hDNM- and pDNM-enzymolysis-injected mice were proven to have more T helper cells and far fewer cytotoxic T cells compared to those of the pDNM group (**Figure 7C** and **D**), which resulted in a higher T helper cells/cytotoxic T cells ratio, implicating a pro-remodelling phenotype. Interestingly, the pDNM-enzymolysis group exhibited similar host responses to the hDNM group in terms of human adaptive immune responses.

Discussion

Porcine-derived dECM biomaterials are potentially useful for repair and reconstruction of xenogenic tissues in the field of tissue engineering and regenerative medicine.[44, 45] Given the similarity in gene sequences between humans and pigs,[46] porcine tissue-derived materials are currently viewed as attractive alternatives in regenerative medicine. Previously, we have successfully prepared dECM scaffolds and their derivative hydrogel from porcine sciatic nerve tissue, namely pDNM and pDNM-gel, by following rather straightforward decellularisation and digestion protocols, and their bioactivity and processibility have been proven in terms of promoting peripheral nerve regeneration and functional recovery *in vitro* and *in vivo*.[17-22] To verify that such mammal-derived xenografts can be used as an appropriate substitute for future clinical applications, herein, a comparative study concerning the variations between the allogeneic hDNM and xenogeneic pDNM was systematically implemented. Unlike our previous reports, this study focuses on comparisons between the

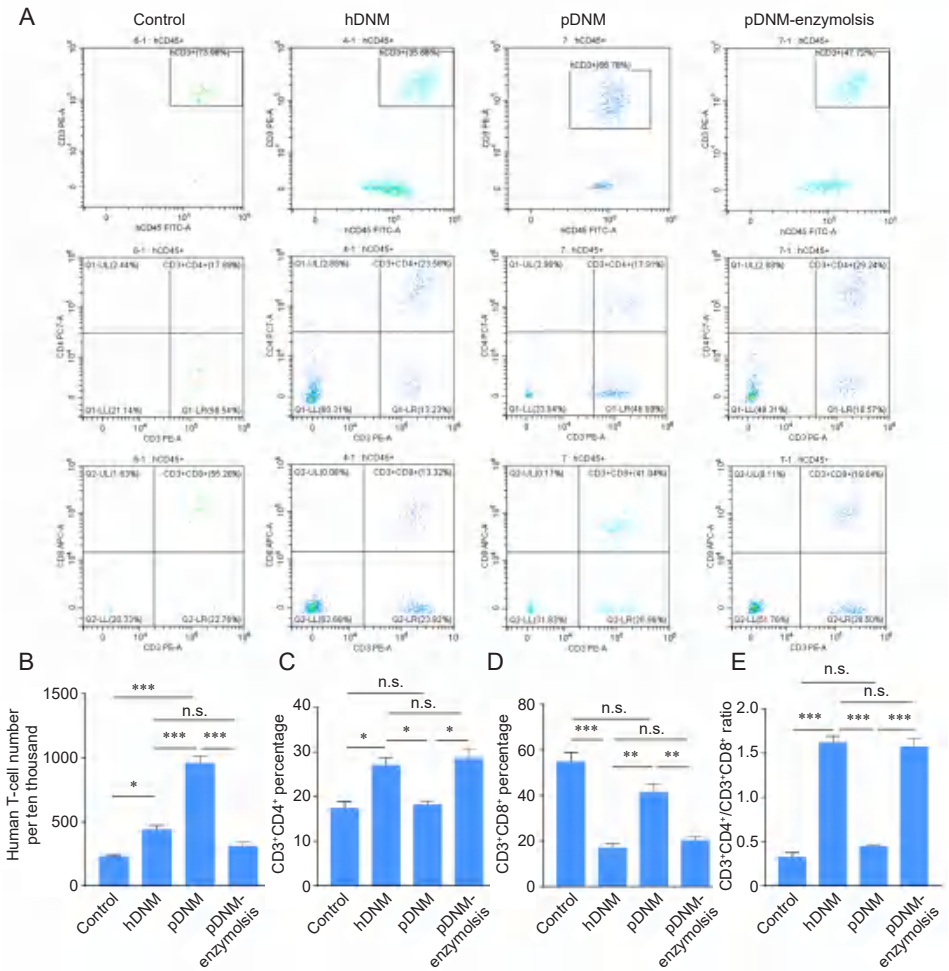

Figure 7. Evaluation of T cell repopulation and their subtypes after injection of hDNM, pDNM, or pDNM-enzymolysis into humanised mice, analysed using flow cytometry. (A) T cells ($hCD45^+hCD3^+$) and their subtypes, including T helper cells ($hCD3^+hCD4^+$) and cytotoxic T cells ($hCD3^+hCD8^+$). (B) The density of total human T cells after introducing the dECMs into Hu-mice. (C) The percentage of the T helper cells ($hCD3^+hCD4^+$). (D) The percentage of cytotoxic T cells ($hCD3^+hCD8^+$). (E) The ratios of T helper cells/cytotoxic T cells. The data are expressed as mean ± SD ($n = 3$). $^*P < 0.05$, $^{**}P < 0.01$, $^{***}P < 0.001$. hDNM: human decellularised nerve matrix; n.s: not significant; pDNM: porcine decellularised nerve matrix.

microstructures of the scaffolds, proteomic compositions, biological functions of the dECM hydrogels, and more importantly, the immunogenicity for potential implantation into human bodies. Furthermore, a consecutive question that we managed to answer is, if pDNM might result in severe host rejection following clinical implantation, can it be modified to produce a more clinically-satisfactory outcome?

We first characterised the microscopic ultrastructures of both hDNM and pDNM scaffolds using SEM. Both decellularised matrices retained the structures of the nerve fascicles and interfascicular connective tissues, which are consistent with the high-resolution topography of the native peripheral nerve fascicles reported by Yan et al.[47] These longitudinally-aligned microtubes function in guiding axonal growth.[22]

It has been shown that the diverse proteomic compositions of dECMs play a vital role in regulating cellular phenotypes and behaviours.[48, 49] Therefore, we systematically compared the compositions of hDNM and pDNM through proteomic analysis regarding all the protein species and specifically the ECM matrisome. We first realised that most of the constituent biomolecules shared similar contents and functionalities between hDNM and pDNM. However, it was also noticed that pDNM possessed a slightly greater number and higher abundance of matrisome proteins compared to hDNM. Especially, some ECM proteins (such as CSPG4, FGF2, SLIT3, and LAMA2) were only identified in pDNM, which can positively facilitate cellular proliferation, migration, differentiation, and maturation. Meanwhile the core matrisome PODN, which may negatively regulate the above-mentioned biological processes, was far less abundant than that identified in the hDNM. We speculate that the similarity of the proteomic compositions of both hDNM and pDNM assure the fundamental functionalities of the tissue-specific dECM materials, but that the abundant ECM components found in the pDNM may provide higher bioactivities in facilitating nerve regeneration and functionalisation.

Therefore, to validate and compare the bioactivities of the dECM materials, primary HSCs were cultured on dECM hydrogels prepared from hDNM and pDNM. Since the cells cultured on dECM scaffold are typically hard to be visualised, hydrogel-based dECM materials were employed rather than the scaffolds themselves. Although some biomacromolecules in the DNM might undergo degradation or denaturation during enzymatic digestion, most of the dECM proteins were retained in the obtained hydrogels.[50, 51] Throughout all the *in vitro* characterisations, it has been acknowledged that both the hDNM and pDNM hydrogels exhibited similar functionalities in promoting HSC proliferation, migration, and specific gene expressions. This result seems be inconsistent with our normal logic. We speculate the reason may be attributed to degradation of some components when both dECMs are digested into hydrogel. Thus, further, we should characterise the composition of hDNM-gel and pDNM-gel using quantitative proteomic analysis.

Finally, the potential immunological responses in the human body are key to the viability of the various xenografts in clinical application, for example, porcine-derived dECM materials. In this study, we first evaluated the non-primate antigens and some other immunogenic components in the DNMs to assess potential adverse host responses. Among these detected immunogens, the α-Gal component was only evident in the pDNM, as we expected. In fact, it was not only present in the pDNM but also in considerable amounts that might evoke severe immune responses or host rejection in the human body. For this reason, we managed to remove the α-Gal content from the pDNM through enzymatic hydrolysation. It was realised that the α-Gal antigen could be effectively diminished using α-Gal.

Since there are serious ethical issues and difficulties related to experiments on real human bodies, we established a humanised mouse model to simulate the human immune responses to the administration of both hDNM and pDNM, and additionally, the α-Gal-eliminated pDNM (termed pDNM-enzymolysis) *in vivo*. Histological characterisation of the material-injected subcutaneous tissues showed that the introduction of pDNM evoked much more significant cell infiltration compared to that of the hDNM group. Furthermore, studies on the human immune cells in the Hu-mice showed that all the injected DNM materials stimulated considerable immunoreactions and resulted in significant proliferation of immune cells, including B cells and T cells. Obviously, the adaptive immune responses in the pDNM-injected Hu-mice were much more severe than those of the hDNM or pDNM-enzymolysis groups. Further evaluation of the T cell subpopulations revealed that the introduction of pDNM induced fewer T helper cells ($hCD3^+hCD4^+$) and more cytotoxic T-cells ($hCD3^+hCD8^+$), compared to the hDNM. These results suggested that the allogeneic hDNM stimulated a pro-remodelling response, whereas the xenogeneic pDNM intended to elicit a more pro-inflammatory immune reaction.

Since the α-Gal epitope usually serves as the key factor that evokes severe human immune responses, we conjectured that the removal of the α-Gal antigen might alleviate the hostile host responses against the porcine-derived xenografts. To this end, the pDNM-enzymolysis was also tested in the Hu-mice model. The adverse immune responses were found to be highly diminished upon removing the α-Gal content from the pDNM, which was comparable to or even better than that of the hDNM group. In the meantime, the T cells in the pDNM-enzymolysis Hu-mice dominantly retained the pro-regenerative phenotype that may further contribute to tissue regeneration, which was similar to those of the hDNM group. Consequently, considering the translational potential of the xenogeneic pDNM, we believe that this sort of porcine-derived dECM material can be beneficial for future clinical applications, once its residual α-Gal antigen has been removed. The α-Gal content can be properly eliminated by enzymatic hydrolysation, otherwise, the source tissues should be obtained from α-Gal gene-knockout pigs. Currently, the α-Gal epitope-induced immune response has drawn increasing attention for development of implantable dECM biomaterials which may be critical to their clinical translation. However, in the present study, we have not evaluated the potential transmission risk of porcine endogenous retroviruses. They are γ-retroviruses integrated in the genome of all pigs and can be transmitted from pig to human cells, leading to immunodeficiencies and tumors.[52, 53] Further work will be needed to either detect the presence of porcine endogenous retroviruses in pDNM using qPCR methods or directly harvest nerves from genetically-modified pigs.

In this study, two dECM materials derived from human and porcine nerve tissues (hDNM and pDNM) were prepared and compared in terms of their microstructures, compositions, biological performance, and immunogenicity. Basically, both hDNM and pDNM shared almost the same ultrastructure and comparable proteomic compositions. The hydrogels derived from both hDNM and pDNM also resulted in similar regulation of HSC behaviours. Distinct differences were evident regarding the specific antigens and their induced human host immune responses. pDNM contains a few xenoantigens, including α-Gal and MHC-1, that evoked more adverse host responses in a humanised mouse model, compared to the hDNM. After removing most of the α-Gal content using α-Gal hydrolysation, the human host responses were alleviated and became pro-regenerative. It was realized that pDNM-enzymolysis performed similarly to the hDNM and induced similar immune responses. This experimental evidence suggests that the removal of α-Gal antigen is key to the future application of pDNM and pDNM-derived biomaterials. Furthermore, the current study may provide a springboard for both xenogeneic dECM studies and harnessing such functional biomaterials for use at the bedside.

Author contributions

Methodology, material preparation, data collection: RL, WY, and ZR; *in vivo* test support, statistical analysis: RL and SQ; conceptualisation and design: YY, QZ, and XL; funding acquisition, supervision, manuscript finalisation, and project administration: YB; study conceptualisation and design, supervision, data interpretation, project administration, funding acquisition, manuscript drafting and refining: DQ. All authors approved the final version of this manuscript.

Financial support

This study was supported by the National Natural Science Foundation of China (Nos. 51903255 and 52073314), The Key Areas Research and Development Program of Guangdong Province (No. 2020B1111150003), and Science and Technology Program of Guangzhou City (No. 201904010364).

Acknowledgement

The authors would like to thank Ms. Weizhen Tang (a laboratory assistant in Guangdong Engineering Technology Research Centre for Functional Biomaterials, School of Materials Science and Engineering, Sun Yat-sen University) for her assistance in cell culture experiments.

Conflicts of interest statement

The authors declare that they have no competing financial interests or personal relationships that could have appeared to influence the work reported in this study. No conflicts of interest exist between Guangzhou Zhongda Medical Equipment Co., Ltd. and the publication of this paper.

Editor note: Daping Quang are an Editorial Board member of *Biomaterials Translational*. She is blinded from reviewing or making decisions on the manuscript. The article was subject to the journal's standard procedures, with peer review handled independently of this Editorial Board member and her research group.

Additional files

Additional Figure 1: A flow chart of the *in vivo* study.

Additional Figure 2: Scanning electron micrographs showing cross-sectional views of a native human nerve and a native porcine nerve.

1. Krishtul, S.; Baruch, L.; Machluf, M. Processed tissue–derived extracellular matrices: tailored platforms empowering diverse therapeutic applications. *Adv Funct Mater.* **2020**, *30*, 1900386.
2. Garreta, E.; Oria, R.; Tarantino, C.; Pla-Roca, M.; Prado, P.; Fernández-Avilés, F.; Campistol, J. M.; Samitier, J.; Montserrat, N. Tissue engineering by decellularization and 3D bioprinting. *Mater Today.* **2017**, *20*, 166-178.
3. Hussey, G. S.; Dziki, J. L.; Badylak, S. F. Extracellular matrix-based materials for regenerative medicine. *Nat Rev Mater.* 2018, *3*, 159-173.
4. Li, T.; Javed, R.; Ao, Q. Xenogeneic decellularized extracellular matrix-based biomaterials for peripheral nerve repair and regeneration. *Curr Neuropharmacol.* **2021**, *19*, 2152-2163.
5. Zouhair, S.; Sasso, E. D.; Tuladhar, S. R.; Fidalgo, C.; Vedovelli, L.; Filippi, A.; Borile, G.; Bagno, A.; Marchesan, M.; Giorgio, R.; Gregori, D.; Wolkers, W. F.; Romanato, F.; Korossis, S.; Gerosa, G.; Iop, L. A comprehensive comparison of bovine and porcine decellularized pericardia: new insights for surgical applications. *Biomolecules.* **2020**, *10*, 371.
6. Capella-Monsonís, H.; De Pieri, A.; Peixoto, R.; Korntner, S.; Zeugolis, D. I. Extracellular matrix-based biomaterials as adipose-derived stem cell delivery vehicles in wound healing: a comparative study between a collagen scaffold and two xenografts. *Stem Cell Res Ther.* **2020**, *11*, 510.
7. Bowers, S. L.; Banerjee, I.; Baudino, T. A. The extracellular matrix: at the center of it all. *J Mol Cell Cardiol.* **2010**, *48*, 474-482.
8. Keane, T. J.; Londono, R.; Turner, N. J.; Badylak, S. F. Consequences of ineffective decellularization of biologic scaffolds on the host response. *Biomaterials.* **2012**, *33*, 1771-1781.
9. Badylak, S. F. Xenogeneic extracellular matrix as a scaffold for tissue reconstruction. *Transpl Immunol.* **2004**, *12*, 367-377.
10. Badylak, S. F.; Gilbert, T. W. Immune response to biologic scaffold materials. *Semin Immunol.* **2008**, *20*, 109-116.
11. Kasper, M.; Deister, C.; Beck, F.; Schmidt, C. E. Bench-to-bedside lessons learned: commercialization of an acellular nerve graft. *Adv Healthc Mater.* **2020**, *9*, e2000174.
12. Yang, L. M.; Liu, X. L.; Zhu, Q. T.; Zhang, Y.; Xi, T. F.; Hu, J.; He, C. F.; Jiang, L. Human peripheral nerve-derived scaffold for tissue-engineered nerve grafts: histology and biocompatibility analysis. *J Biomed Mater Res B Appl Biomater.* **2011**, *96*, 25-33.
13. Colwell, A. S.; Longaker, M. T.; Lorenz, H. P. Mammalian fetal organ regeneration. *Adv Biochem Eng Biotechnol.* **2005**, *93*, 83-100.
14. Sicari, B. M.; Johnson, S. A.; Siu, B. F.; Crapo, P. M.; Daly, K. A.; Jiang, H.; Medberry, C. J.; Tottey, S.; Turner, N. J.; Badylak, S. F. The effect of source animal age upon the in vivo remodeling characteristics of an extracellular matrix scaffold. *Biomaterials.* **2012**, *33*, 5524-5533.
15. Badylak, S. F. The extracellular matrix as a biologic scaffold material. *Biomaterials.* **2007**, *28*, 3587-3593.
16. Seif-Naraghi, S. B.; Singelyn, J. M.; Salvatore, M. A.; Osborn, K. G.; Wang, J. J.; Sampat, U.; Kwan, O. L.; Strachan, G. M.; Wong, J.; Schup-Magoffin, P. J.; Braden, R. L.; Bartels, K.; DeQuach, J. A.; Preul, M.; Kinsey, A. M.; DeMaria, A. N.; Dib, N.; Christman, K. L. Safety and efficacy of an injectable extracellular matrix hydrogel for treating myocardial infarction. *Sci Transl Med.* **2013**, *5*, 173ra125.
17. Chen, S.; Du, Z.; Zou, J.; Qiu, S.; Rao, Z.; Liu, S.; Sun, X.; Xu, Y.; Zhu, Q.; Liu, X.; Mao, H. Q.; Bai, Y.; Quan, D. Promoting neurite growth and schwann cell migration by the harnessing decellularized nerve matrix onto nanofibrous guidance. *ACS Appl Mater Interfaces.* **2019**, *11*, 17167-17176.
18. Zheng, C.; Yang, Z.; Chen, S.; Zhang, F.; Rao, Z.; Zhao, C.; Quan, D.; Bai, Y.; Shen, J. Nanofibrous nerve guidance conduits decorated with decellularized matrix hydrogel facilitate peripheral nerve injury repair. *Theranostics.* **2021**, *11*, 2917-2931.
19. Deng, R.; Luo, Z.; Rao, Z.; Lin, Z.; Chen, S.; Zhou, J.; Zhu, Q.; Liu, X.; Bai, Y.; Quan, D. Decellularized extracellular matrix containing electrospun fibers for nerve regeneration: a comparison between core–shell structured and preblended composites. *Adv Fiber Mater.* **2022**, *4*, 503-519.
20. Xu, Y.; Zhou, J.; Liu, C.; Zhang, S.; Gao, F.; Guo, W.; Sun, X.; Zhang, C.; Li, H.; Rao, Z.; Qiu, S.; Zhu, Q.; Liu, X.; Guo, X.; Shao, Z.; Bai, Y.; Zhang, X.; Quan, D. Understanding the role of tissue-specific decellularized spinal cord matrix hydrogel for neural stem/progenitor cell microenvironment reconstruction and spinal cord injury. *Biomaterials.* **2021**, *268*, 120596.
21. Lin, T.; Liu, S.; Chen, S.; Qiu, S.; Rao, Z.; Liu, J.; Zhu, S.; Yan, L.; Mao, H.; Zhu, Q.; Quan, D.; Liu, X. Hydrogel derived from porcine decellularized nerve tissue as a promising biomaterial for repairing peripheral nerve defects. *Acta Biomater.* **2018**, *73*, 326-338.
22. Rao, Z.; Lin, T.; Qiu, S.; Zhou, J.; Liu, S.; Chen, S.; Wang, T.; Liu, X.; Zhu, Q.; Bai, Y.; Quan, D. Decellularized nerve matrix hydrogel scaffolds with longitudinally oriented and size-tunable microchannels for peripheral nerve regeneration. *Mater Sci Eng C Mater Biol Appl.* **2021**, *120*, 111791.
23. Keane, T. J.; Badylak, S. F. The host response to allogeneic and xenogeneic biological scaffold materials. *J Tissue Eng Regen Med.* **2015**, *9*, 504-511.
24. Brown, B. N.; Londono, R.; Tottey, S.; Zhang, L.; Kukla, K. A.; Wolf, M. T.; Daly, K. A.; Reing, J. E.; Badylak, S. F. Macrophage phenotype as a predictor of constructive remodeling following the implantation of biologically derived surgical mesh materials. *Acta Biomater.* **2012**, *8*, 978-987.

25. Brown, B. N.; Valentin, J. E.; Stewart-Akers, A. M.; McCabe, G. P.; Badylak, S. F. Macrophage phenotype and remodeling outcomes in response to biologic scaffolds with and without a cellular component. *Biomaterials.* **2009**, *30*, 1482-1491.
26. Galili, U. Interaction of the natural anti-Gal antibody with alpha-galactosyl epitopes: a major obstacle for xenotransplantation in humans. *Immunol Today.* **1993**, *14*, 480-482.
27. Mestas, J.; Hughes, C. C. Of mice and not men: differences between mouse and human immunology. *J Immunol.* **2004**, *172*, 2731-2738.
28. Qiu, S.; Rao, Z.; He, F.; Wang, T.; Xu, Y.; Du, Z.; Yao, Z.; Lin, T.; Yan, L.; Quan, D.; Zhu, Q.; Liu, X. Decellularized nerve matrix hydrogel and glial-derived neurotrophic factor modifications assisted nerve repair with decellularized nerve matrix scaffolds. *J Tissue Eng Regen Med.* **2020**, *14*, 931-943.
29. Devaud, Y. R.; Avilla-Royo, E.; Trachsel, C.; Grossmann, J.; Martin, I.; Lutolf, M. P.; Ehrbar, M. Label-free quantification proteomics for the identification of mesenchymal stromal cell matrisome inside 3D poly(ethylene glycol) hydrogels. *Adv Healthc Mater.* **2018**, *7*, e1800534.
30. UniProt Consortium. UniProt: the universal protein knowledgebase in 2021. *Nucleic Acids Res.* **2021**, *49*, D480-D489.
31. Morfeld, P. Controlling the false discovery rate in many SMR analyses. *J Occup Environ Med.* **2016**, *58*, e21-22.
32. Naba, A.; Clauser, K. R.; Ding, H.; Whittaker, C. A.; Carr, S. A.; Hynes, R. O. The extracellular matrix: Tools and insights for the "omics" era. *Matrix Biol.* **2016**, *49*, 10-24.
33. Schneider, C. A.; Rasband, W. S.; Eliceiri, K. W. NIH image to ImageJ: 25 years of image analysis. *Nat Methods.* **2012**, *9*, 671-675.
34. Bubner, B.; Baldwin, I. T. Use of real-time PCR for determining copy number and zygosity in transgenic plants. *Plant Cell Rep.* **2004**, *23*, 263-271.
35. Stone, K. R.; Ayala, G.; Goldstein, J.; Hurst, R.; Walgenbach, A.; Galili, U. Porcine cartilage transplants in the cynomolgus monkey. III. Transplantation of alpha-galactosidase-treated porcine cartilage. *Transplantation.* **1998**, *65*, 1577-1583.
36. Percie du Sert, N.; Hurst, V.; Ahluwalia, A.; Alam, S.; Avey, M. T.; Baker, M.; Browne, W. J.; Clark, A.; Cuthill, I. C.; Dirnagl, U.; Emerson, M.; Garner, P.; Holgate, S. T.; Howells, D. W.; Karp, N. A.; Lazic, S. E.; Lidster, K.; MacCallum, C. J.; Macleod, M.; Pearl, E. J.; Petersen, O. H.; Rawle, F.; Reynolds, P.; Rooney, K.; Sena, E. S.; Silberberg, S. D.; Steckler, T.; Würbel, H. The ARRIVE guidelines 2.0: Updated guidelines for reporting animal research. *PLoS Biol.* **2020**, *18*, e3000410.
37. Lan, P.; Tonomura, N.; Shimizu, A.; Wang, S.; Yang, Y. G. Reconstitution of a functional human immune system in immunodeficient mice through combined human fetal thymus/liver and CD34$^+$ cell transplantation. *Blood.* **2006**, *108*, 487-492.
38. Khan, S.; Kaihara, K. A. Single-cell RNA-sequencing of peripheral blood mononuclear cells with ddSEQ. *Methods Mol Biol.* **2019**, *1979*, 155-176.
39. Wang, R. M.; Johnson, T. D.; He, J.; Rong, Z.; Wong, M.; Nigam, V.; Behfar, A.; Xu, Y.; Christman, K. L. Humanized mouse model for assessing the human immune response to xenogeneic and allogeneic decellularized biomaterials. *Biomaterials.* **2017**, *129*, 98-110.
40. Crapo, P. M.; Medberry, C. J.; Reing, J. E.; Tottey, S.; van der Merwe, Y.; Jones, K. E.; Badylak, S. F. Biologic scaffolds composed of central nervous system extracellular matrix. *Biomaterials.* **2012**, *33*, 3539-3547.
41. Behan, B. L.; DeWitt, D. G.; Bogdanowicz, D. R.; Koppes, A. N.; Bale, S. S.; Thompson, D. M. Single-walled carbon nanotubes alter Schwann cell behavior differentially within 2D and 3D environments. *J Biomed Mater Res A.* **2011**, *96*, 46-57.
42. Aamodt, J. M.; Grainger, D. W. Extracellular matrix-based biomaterial scaffolds and the host response. *Biomaterials.* **2016**, *86*, 68-82.
43. Walsh, N. C.; Kenney, L. L.; Jangalwe, S.; Aryee, K. E.; Greiner, D. L.; Brehm, M. A.; Shultz, L. D. Humanized mouse models of clinical disease. *Annu Rev Pathol.* **2017**, *12*, 187-215.
44. Kočí, Z.; Výborný, K.; Dubišová, J.; Vacková, I.; Jäger, A.; Lunov, O.; Jiráková, K.; Kubinová, Š. Extracellular matrix hydrogel derived from human umbilical cord as a scaffold for neural tissue repair and its comparison with extracellular matrix from porcine tissues. *Tissue Eng Part C Methods.* **2017**, *23*, 333-345.
45. Tan, Q. W.; Zhang, Y.; Luo, J. C.; Zhang, D.; Xiong, B. J.; Yang, J. Q.; Xie, H. Q.; Lv, Q. Hydrogel derived from decellularized porcine adipose tissue as a promising biomaterial for soft tissue augmentation. *J Biomed Mater Res A.* **2017**, *105*, 1756-1764.
46. Bikhet, M.; Morsi, M.; Hara, H.; Rhodes, L. A.; Carlo, W. F.; Cleveland, D.; Cooper, D. K. C.; Iwase, H. The immune system in infants: Relevance to xenotransplantation. *Pediatr Transplant.* **2020**, *24*, e13795.
47. Yan, L.; Guo, Y.; Qi, J.; Zhu, Q.; Gu, L.; Zheng, C.; Lin, T.; Lu, Y.; Zeng, Z.; Yu, S.; Zhu, S.; Zhou, X.; Zhang, X.; Du, Y.; Yao, Z.; Lu, Y.; Liu, X. Iodine and freeze-drying enhanced high-resolution MicroCT imaging for reconstructing 3D intraneural topography of human peripheral nerve fascicles. *J Neurosci Methods.* **2017**, *287*, 58-67.
48. Spang, M. T.; Christman, K. L. Extracellular matrix hydrogel therapies: in vivo applications and development. *Acta Biomater.* **2018**, *68*, 1-14.
49. Bi, H.; Ye, K.; Jin, S. Proteomic analysis of decellularized pancreatic matrix identifies collagen V as a critical regulator for islet organogenesis from human pluripotent stem cells. *Biomaterials.* **2020**, *233*, 119673.
50. Choudhury, D.; Yee, M.; Sheng, Z. L. J.; Amirul, A.; Naing, M. W. Decellularization systems and devices: State-of-the-art. *Acta Biomater.* **2020**, *115*, 51-59.
51. Xing, H.; Lee, H.; Luo, L.; Kyriakides, T. R. Extracellular matrix-derived biomaterials in engineering cell function. *Biotechnol Adv.* **2020**, *42*, 107421.
52. Yue, Y.; Xu, W.; Kan, Y.; Zhao, H. Y.; Zhou, Y.; Song, X.; Wu, J.; Xiong, J.; Goswami, D.; Yang, M.; Lamriben, L.; Xu, M.; Zhang, Q.; Luo, Y.; Guo, J.; Mao, S.; Jiao, D.; Nguyen, T. D.; Li, Z.; Layer, J. V.; Li, M.; Paragas, V.; Youd, M. E.; Sun, Z.; Ding, Y.; Wang, W.; Dou, H.; Song, L.; Wang, X.; Le, L.; Fang, X.; George, H.; Anand, R.; Wang, S. Y.; Westlin, W. F.; Güell, M.; Markmann, J.; Qin, W.; Gao, Y.; Wei, H. J.; Church, G. M.; Yang, L. Extensive germline genome engineering in pigs. *Nat Biomed Eng.* **2021**, *5*, 134-143.
53. Niu, D.; Wei, H. J.; Lin, L.; George, H.; Wang, T.; Lee, I. H.; Zhao, H. Y.; Wang, Y.; Kan, Y.; Shrock, E.; Lesha, E.; Wang, G.; Luo, Y.; Qing, Y.; Jiao, D.; Zhao, H.; Zhou, X.; Wang, S.; Wei, H.; Güell, M.; Church, G. M.; Yang, L. Inactivation of porcine endogenous retrovirus in pigs using CRISPR-Cas9. *Science.* **2017**, *357*, 1303-1307.

Received: November 17, 2022
Revised: December 6, 2022
Accepted: March 8, 2023
Available online: September 28, 2023